Hall Magnetohydrodynamics Simulations of Hall-Physics-Driven Effects in Low-Density Plasmas Surrounding Dense Z-Pinch Liners

by

Jeffrey M. Woolstrum

A dissertation submitted in partial fulfillment
of the requirements for the degree of
Doctor of Philosophy
(Nuclear Engineering and Radiolgical Sciences)
in The University of Michigan
2022

Doctoral Committee:

Associate Professor Ryan McBride, Chair
Associate Research Scientist Nicholas Jordan
Assistant Professor Eric Johnsen
Associate Professor Carolyn Kuranz
Professor Charles Seyler

Jeffrey M. Woolstrum
jeffwool@umich.edu
ORCID iD: 0000-0002-6118-0995

This work was made possible by my incredibly supportive family and all of my friends.

ACKNOWLEDGEMENTS

This research was supported by the NNSA Stewardship Sciences Academic Programs under DOE Cooperative Agreement DE-NA0003764.

Sandia National Laboratories is a multimission laboratory managed and operated by National Technology and Engineering Solutions of Sandia LLC (NTESS), a wholly owned subsidiary of Honeywell International Inc., for the U.S. Department of Energy's National Nuclear Security Administration (NNSA) under contract DE-NA0003525. This paper describes objective technical results and analysis. Any subjective views or opinions that might be expressed in the paper do not necessarily represent the views of the U.S. Department of Energy or the United States Government.

TABLE OF CONTENTS

DEDICATION ii

ACKNOWLEDGEMENTS iii

LIST OF FIGURES vi

ABSTRACT xiii

CHAPTER

I. Introduction 1

1.1 A Brief Introduction to Z-Pinch Liner Implosions 1
1.2 PERSEUS: Magnetohydrodynamics and Hall physics 6
1.2.1 Relaxation Model 7
1.2.2 Vacuum Resistivity 9
1.3 Plasma Instabilities 12
1.3.1 Magneto-Rayleigh-Taylor Instability 12
1.3.2 Hall-MHD Model and Reduced Model 13

II. Extended Magnetohydrodynamics Simulations of Thin-Foil Z-Pinch Implosions with Comparison to Experiments 18

2.1 Thin-Foil Z-Pinches 19
2.2 Simulations of Previous Experiments Conducted on MAIZE . 20
2.3 Axial Roll-Up of Instability Structures in Thin-Foil Liner Simulations 31
2.4 Support Rod Diameter Effects on Helical Mode Persistence . 38
2.5 Precursor Plasma Column Morphology 42

III. Origin of Helical Instabilities in Axially Premagnetized Thin-Foil Liner Z-pinch Implosions using Hall Magnetohydrodynamics 45

3.1 Simulation Setup 46
3.2 Hall Interchange Instability As a Seed for Helical MRTI . . . 49
3.3 Boundary Conditions Effects 55
3.4 Comparison of Hall-MHD and MHD 59
3.5 Discussion 67

IV. Discussion and Summary 72

V. Future Work 75

APPENDIX 79

BIBLIOGRAPHY 85

LIST OF FIGURES

Figure

1.1 (a) Simulation of a MagLIF liner imploding showing the three stages of the concept: premagnetization, laser preheat, and compression. (b) Time-integrated x-ray self-emission of the stagnation column. Images courtesy of Ref. [24]. 2

1.2 Support rod structure needed to handle ultrathin foils during installation and vacuum pump down on MAIZE. The effects of this structure are explored in Chapter II, where it is shown that the support rod plays a key role in the late time morphology of the instability structures. 3

1.3 (a) Penetrating x-ray radiograph from Ref. [16], showing the helical nature of MRTI in an axially premagnetized MagLIF liner implosion experiment on the Z facility at Sandia National Laboratories. (b) Visible-light self-emission image showing helical instability structures from an axially premagnetized thin-foil liner implosion on the 1-MA MAIZE LTD at the University of Michigan, from Ref. [21]. (c) Image from PERSEUS showing a simulated axially premagnetized thin-foil liner implosion with helical MRTI without the need for artificial helical seeding. 4

1.4 Helical perturbation in the azimuthal component of the current density, plotted on an iso-density surface (10^{24} m^{-3}) at 75 ns. This highlights one of the perturbation effects of the Hall interchange instability, which leads to helical formations in the current on the liner plasma outer surface. 6

2.1 Simulation setups and implosion overview. (a,b) Initial setups showing examples of the electrode geometries and power feeds used, where red represents solid density aluminum and blue is vacuum. The setup in (a) includes an axial feed and was driven by a boundary condition at the lower edge of the image (i.e., at a specified axial position). The setup in (b) used a simplified electrode geometry and was driven by a boundary condition at the left and right edges of the image (i.e., at a specified radius). It was found that including the axial feed was unnecessary and only added unnecessary volume to the simulation space, reducing the grid resolution; thus, the setup in (b) was used for most of this chapter. (c)-(h) Example density slices taken during a representative liner implosion. 22

2.2 Simulated liner implosion trajectories from PERSEUS and from a simplified 1-D thin-shell model, as well as the MAIZE electrical current used to drive the simulated implosions. The average liner radius plotted for PERSEUS was found by integrating the liner density in both the axial (z) and azimuthal (θ) directions. This figure should be contrasted with Fig. 1b in Ref. [19]. The simplified 1-D thin-shell simulation (sometimes referred to as a "0-D" model) is shown for reference and demonstrates that PERSEUS captures early time expansion of the liner and late time bounce of the liner off of the inner support rod, which can also be seen in experiment (see Fig. 1b in Ref. [19]). 23

2.3 Mode merging of instability lobes in simulation. The duration of this single mode-merging event is approximately 30 ns. Both the duration and the overall dynamics of this mode-merging event agree well with the experimental results presented in Fig. 7(b) of Ref. [21]. 26

2.4 PERSEUS instability amplitude as a function of normalized distance moved, $\hat{d} \equiv 1 - r(t)/r(0)$. The instability amplitude is subject to the iso-density surface chosen and becomes difficult to determine as the liner begins to bounce off of the inner support rod. This is due to the lower effective resolution as the imploding liner moves through the cartesian grid, which can make it difficult to determine an accurate instability amplitude. 27

2.5 Iso-density surface images taken at a number density of 6×10^{18} cm^{-3} and a time of 117 ns, showing (a) the highlighted helical instability lobes that develop on the liner and (b) the corresponding helical line traces used to identify the effective azimuthal mode number. The origin of these helical instabilities is being studied and will be presented in depth in III. 29

2.6 Effective azimuthal mode number m as a function of time. The mode numbers were extracted from the simulation data using the helical fitting technique described by Awe et al. in Ref [14]. This technique uses the parametric equations given in the text to trace 3D helices onto a 2D image. The results plotted here indicate that the instability structure initially consists of many intertwined helices ($m \approx 7$), and that these helices merge into fewer helices throughout the implosion process. The mode merging ceases upon stagnation ($t \approx 140$ ns), with a dominant mode number of $m \approx 2$ (two intertwined helices). These results are consistent with the experimental results presented in Refs. [25] and [21]. 30

2.7 Two timesteps from a 3D liner implosion which shows a helical instability lobe exhibiting axial roll-up characteristics in the liner plasma. This is driven by radially dependent $\mathbf{E} \times \mathbf{B}$ velocity shear within the plasma. 32

2.8 Slice from a 3D simulation showing the 4 probe locations used to map the velocity values v_z(r) plotted in Fig. 2.9. This slice view also highlights the roll-up behavior of the MRT instability lobes. 33

2.9 Graph of upward velocity $v_z(r)$, revealing the velocity shear present in the instability lobes (i.e., the plasma has larger values of v_z at larger radii). These velocity measurements were taken at 117 ns. . . 34

2.10 Plot of magnetic field vectors (blue) and electric field vectors (red) around the helical lobe plasma, which leads to $\mathbf{E} \times \mathbf{B}$ drift radially inward (into the liner/page) above the lobe and outward below the lobe. This is a contributing feature to instability roll-up. In this figure, $\hat{r}$ is into the page and $\hat{z}$ is the vertical axis. 35

2.11 The radial component of $\mathbf{E} \times \mathbf{B}$. The darker red regions are directed radially inward more strongly. These regions are generally found on the top of the MRT instability lobes and contribute to the axially asymmetric roll-up features by creating a horizontal shear in $\mathbf{E} \times \mathbf{B}$ drift in addition to the axial velocity shear. Note that the $\hat{x}$ direction in this plot is the radial direction and the positive direction is to the right in this figure. 36

2.12 Axial component of $\mathbf{E} \times \mathbf{B}$ within a cross-sectional slice of the plasma column. This shows that at the edges of the plasma column, there is generally a significant increase in upwards $\mathbf{E} \times \mathbf{B}$ drift. 37

2.13 Comparison of thin-foil implosions for 4 different cases of on-axis support rod radii: (a) 0.5 mm; (b) 0.25 mm; (c) 0.1 mm; (d) 0 mm (no rod). The time chosen for this comparison is 10 ns after stagnation. The iso-density surface shown is 1×10^{19} cm^{-3}. The image in part (a) should be contrasted with Fig. 5 in Ref. [19] . . . 39

2.14 Time evolution comparison of thin-foil liner implosions for on-axis support rod radii of (a) 0.5 mm and (b) 0 mm (no rod). The time labels are relative to peak current. For ease of contrasting, the coloring is based on distance from the cylindrical axis and is tinted slightly red for the case with no support rod and slightly blue for the case with the support rod. The iso-density surface shown is 1×10^{19} cm^{-3}. 41

2.15 Simulation of a thin-foil liner implosion with no support rod on axis. The lack of a support rod allows a precursor plasma column to assemble on axis with various instability structures. A particularly well-defined structure is identified by the white arrow. This structure is tracked through stagnation and into the explosion phase. These six frames illustrate that the morphology of the low-density precursor plasma, which arrives on axis ahead of the imploding liner bulk, is largely responsible for setting the morphology of the imploding liner bulk during stagnation and explosion. This figure should be contrasted with Fig. 13(b) in Ref. [51] 44

3.1 Initial conditions of the simulation setup that shows the coronal layer (6×10^{14} cm^{-3}) and the liner plasma (3×10^{19} cm^{-3}). In addition, two single cell layers between the liner plasma and coronal plasma are included that help to step the density down and reduce the sharp density gradient. Note a uniform 2-T axial magnetic field is applied throughout the simulation volume. 48

3.2 Helical MRTI forming in the dense liner plasma 185 ns into the current pulse. The iso-density surface shown is for 10^{24} m^{-3}. Magnetic field lines are traced in blue and current density streamlines are traced in red. 50

3.3 Helical perturbation in the azimuthal component of the current density, plotted on an iso-density surface (10^{24} m^{-3}) at 75 ns. This highlights one of the perturbation effects of the Hall interchange instability, which leads to helical formations in the current on the liner plasma outer surface. 51

3.4 Perturbation in the azimuthal component of the current density, plotted with an iso-density surface slice of the liner plasma (10^{23} m^{-3}) at six time steps to show the process of the perturbations forming in the coronal layer and embedding into the dense liner plasma. The cylindrical axis of symmetry is the right edge of each image, while the outer simulation boundary is the left edge of the images. 53

3.5 Perturbation in the radial component of current density, plotted on a 2-D slice from the simulation volume over top of which an iso-density surface transparency of the dense liner plasma (10^{23} m^{-3}) at four time steps to show the process of the perturbations forming in the coronal layer and extending into the liner plasma. 54

3.6 Plot of the azimuthal perturbation amplitude growth rate. The amplitude was taken by an axial line-out through the coronal plasma subject to the Hall interchange instability. The growth rate found from this analysis compares very closely to the growth rate predicted by theory. The error bars are determined from one standard deviation in the perturbation amplitude. 56

3.7 Plot of the axial wave number of the perturbation in the azimuthal current. The wave number is set within a few nanoseconds of the simulation and remains fairly constant throughout the period when the interchange instability is still the most important instability ($\lesssim$80 ns). 57

3.8 Plot of a 2-D slice of J_θ from a 3-D simulation of a thin-foil z-pinch with open outflow boundary conditions on the upper and lower z boundaries at 50 ns. The Hall instability bunching of J_θ in the coronal layer is evident as well as the filament of J_θ discussed in Seyler's gas-puff simulations [54]. 60

3.9 Plot of the azimuthal current density from a 2-D slice of the full 3-D simulation at 75 ns with Hall physics omitted. This image also has a partially transparent grey iso-density slice (10^{24} m^{-3}) to show the liner plasma. In this image, the lack of Hall physics prevents the Hall instability dynamics, in the azimuthal current, to take place and from the current bunching which has been discussed throughout this dissertation. The cylindrical axis of symmetry (centerline) is the rightmost edge of the image. 61

3.10 Plot of the azimuthal current density from a 2-D slice of the full 3-D simulation at 75 ns with Hall physics included. This image also has a partially transparent grey iso-density slice (10^{24} m^{-3}) to show the liner plasma. 62

3.11 Plot of the azimuthal current from a 2-D slice of the full 3-D simulation at 100 ns with Hall physics omitted. This image again has a partially transparent grey iso-density slice (10^{24} m^{-3}) to show the liner plasma. In this later time step (relative to Fig. 3.9), the azimuthal current has compressed against the outer surface of the liner plasma and shows no perturbation structures. 63

3.12 Plot of the azimuthal current from a 2-D slice of the full 3-D simulation at 100 ns with Hall physics included. This image again has a partially transparent grey iso-density slice (10^{24} m^{-3}) to show the liner plasma. In this later time step with Hall physics (relative to Fig. 3.10), the azimuthal current in the coronal layer continues to display the bunching and vortices that are the result of the Hall instability. 64

3.13 Plot of the azimuthal current density at 100 ns with Hall physics omitted. This image is of a full 3-D iso-density surface (10^{24} m^{-3}) to show the liner plasma's outer surface. In this plot, the azimuthal current does not show a predominant, consistent pattern. 65

3.14 Plot of the azimuthal current density at 100 ns with Hall physics included. This image is of a full 3-D iso-density slice (10^{24} m^{-3}) to show the liner plasma's outer surface. In this plot, the azimuthal current shows a regular helical pattern. 66

3.15 Plot from a simulation including Hall MHD of the liner plasma at an iso-density surface of 10^{23} m^{-3} with magnetic field traced in blue and current density traced in red at 100 ns. The current is helical and generally force-free due to effects from the Hall term. Note also that the current traces have a switch-back like feature which is due to the current vortices created by the Hall instability. 68

3.16 Plot from an MHD simulation that does not include Hall physics of the liner plasma at an iso-density surface of 10^{23} m^{-3} with magnetic field traced in blue and current density traced in red at 100 ns. The current does show some force free behavior at this time step, but note that the magnetic field is less helical compared with the HMHD simulation at the same time step. Also, the current traces lack the switch-back feature because the Hall instability is not present. . . . 69

A.1 Plot of the azimuthal perturbation amplitude growth rate for a simulation with grid resolution of 125 μm^3. The amplitude was taken by an axial line-out through the coronal plasma subject to the Hall interchange instability. The growth rate found from this analysis compares very closely to the growth rate predicted from theory (Eq. 1.36). The error bars are determined from one standard deviation in the perturbation amplitude. 82

A.2 Plot of the azimuthal perturbation amplitude growth rate for a simulation with grid resolution of 62.5 μm^3. The amplitude was taken by an axial line-out through the coronal plasma subject to the Hall interchange instability. The growth rate found from this analysis compares very closely to the growth rate predicted from theory (Eq. 1.36). The error bars are determined from one standard deviation in the perturbation amplitude. This plot was from a higher resolution simulation in which the instability structures began forming earlier by about 5-10 ns as compared with the lower resolution simulation presented in Fig. A.1. 83

A.3 Plot of the azimuthal perturbation amplitude growth rate from a simulation with grid resolution of $\sim$83 μm^3. The amplitude was taken by an axial line-out through the coronal plasma subject to the Hall interchange instability. The growth rate found from this analysis compares very closely to the growth rate predicted from theory (Eq. 1.36). The error bars are determined from one standard deviation in the perturbation amplitude. This plot was from an intermediate resolution simulation. 84

ABSTRACT

Presented in this dissertation is a new Hall physics driven mechanism for describing the seeding and formation of helical instability structures in axially premagnetized thin-foil liner z-pinch implosions driven by the 1-MA, 100-ns MAIZE pulsed power generator at the University of Michigan. This mechanism involves several effects within a low-density coronal plasma layer around the thin-foil liner that forms when the driving current pulse is applied. This low-density coronal layer is then subject to Hall physics, specifically a Hall interchange instability, which leads to several effects including current advection, current vortices, magnetic field advection, axial flux amplification, and other phenomena that all contribute to a helical seeding of the magneto-Rayleigh-Taylor instability (MRTI). These Hall physics effects are studied numerically using the 3D Hall magnetohydrodynamics code, PERSEUS [C.E. Seyler and M.R. Martin, Phys. Plasmas 18, 012703 (2011)]. This study has important implications for the magnetized liner inertial fusion (MagLIF) program at Sandia National Laboratories, where similar helical instability structures have been observed in axially premagnetized thick-walled liner implosions on the 18–30 MA Z facility.

This dissertation also used PERSEUS to explore the late time effects of the on-axis support rod used to hold the thin-foil liners upright in the MAIZE facility as well as make a comparison of MRTI behavior between simulation and experiment. The simulation results [J.M. Woolstrum, et. al., Phys. Plasmas 27, 092705 (2020)] show that by limiting the maximum implosion convergence obtainable, the on-axis support rod plays a key role in preserving the integrity of the helical MRTI structures beyond the implosion phase, into the stagnation and explosion phases of the experiments

(as observed on MAIZE [D.A. Yager-Elorriaga, et. al., Phys. Plasmas 25, 056307 (2018)]). The simulation results also show that if the support rod were removed, the morphology of the stagnation column during the explosion phase would be determined by the morphology of the precursor plasma column that establishes itself on axis prior to the arrival of the bulk of the imploding liner material.

CHAPTER I

Introduction

1.1 A Brief Introduction to Z-Pinch Liner Implosions

Z-pinches have been studied extensively as a platform for Inertial Confinement Fusion (ICF), specifically as part of the Magnetized Liner Inertial Fusion (MagLIF) [1, 2] efforts on the 100-ns, 20-MA Z machine at Sandia National Laboratories [3]. MagLIF makes use of cylindrical metal tubes ("liners") that are imploded using the strong electrical currents produced by the Z machine. These currents are directed axially along the liner's outer surface. This creates a $\mathbf{J} \times \mathbf{B}$ force density that drives the implosion radially inward [4]. These liners, which have an initial radius of about 3 mm, a wall thickness of about 0.5 mm, and a height of about 10 mm, are unstable to the acceleration-driven Magneto-Rayleigh-Taylor (MRT) Instability (MRTI) [5–23], and to magnetic-compression-driven instabilities such as the $m = 0$ "sausage mode", the $m = 1$ "kink mode", and general $m \geq 1$ helical modes, where m is the azimuthal mode number that also represents the number of intertwined helices in the instability structure [14, 19, 21, 23]. These are fast-growing instabilities that are detrimental to implosion uniformity and thus to efforts in magnetically driven ICF [1, 9, 11, 13–16].

In MagLIF, both the fuel and the metallic liner surrounding the fuel are premagnetized with an axial magnetic field B_z to limit thermal conduction losses from the hot fuel to the cold liner. Figure 1.1 shows the three stages of MagLIF (magnetiza-

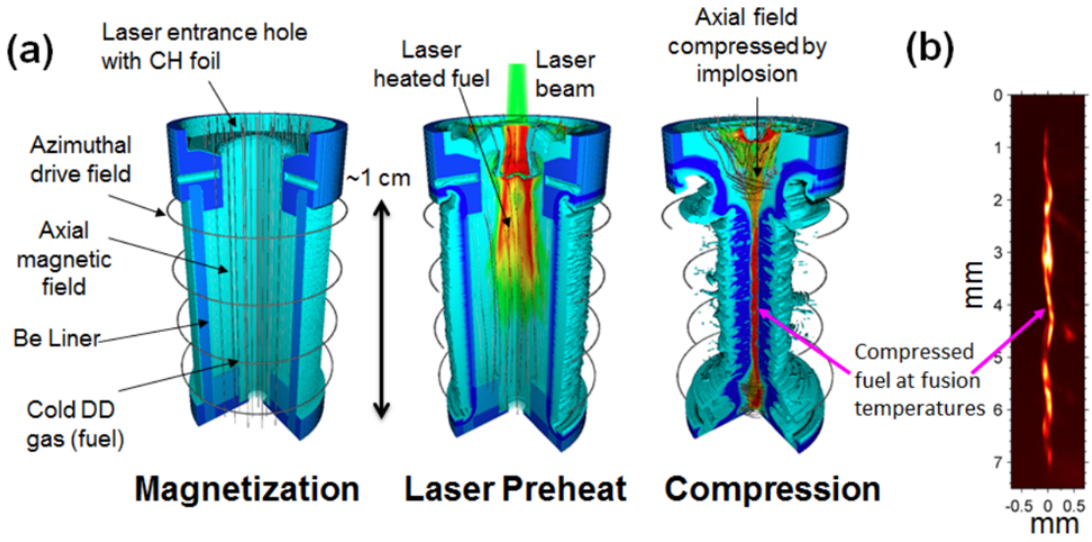

Figure 1.1: (a) Simulation of a MagLIF liner imploding showing the three stages of the concept: premagnetization, laser preheat, and compression. (b) Time-integrated x-ray self-emission of the stagnation column. Images courtesy of Ref. [24].

tion, laser preheat, and compression) as well as a time-integrated x-ray self-emission image of the stagnation column [24]. From penetrating radiography experiments on the Z-machine, the combination of the premagnetizing B_z field with the implosion-driving B_θ field was found to result in helical instability structures with $m \approx 6$ [14]. Furthermore, when $B_z = 0$, these helical modes are absent, and the instability structures becomes azimuthally correlated [13, 15]. The development of the helical modes for $B_z \neq 0$ was surprising because B_θ was expected to quickly dominate over B_z, since B_θ grows rapidly as the current on Z surges to ~20 MA, while B_z was expected to stay roughly constant, at its initial value of about 10 T. As the fastest growing modes of MRTI satisfy $\mathbf{k} \cdot \mathbf{B} = 0$, seeing helical modes suggests that B_z was large enough to make B_z/B_θ significant. Additionally, at the time of the original experiments with $B_z \neq 0$, computer simulations had not predicted the formation of helical instability structures.

To study metal liner implosion instabilities on a university-scale pulsed power machine (~1 MA in ~100 ns) requires significantly less mass in the liner. Because of

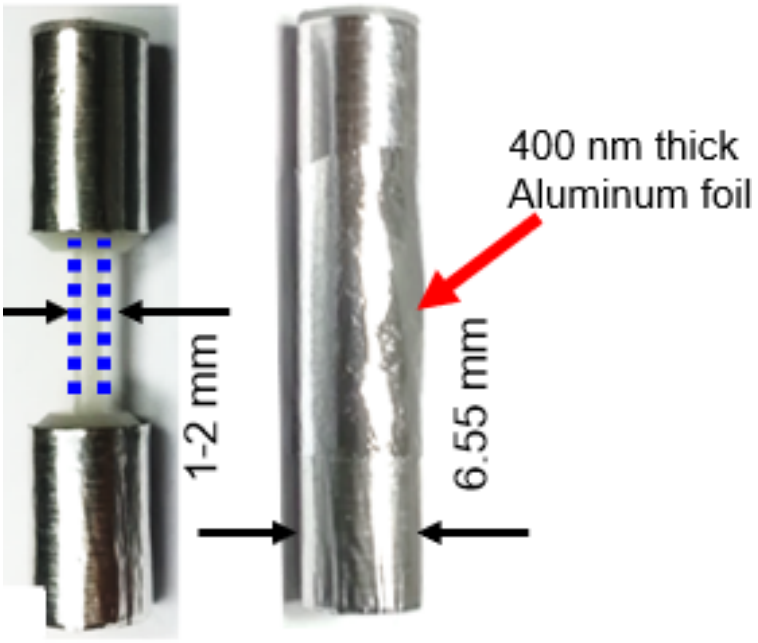

Figure 1.2: Support rod structure needed to handle ultrathin foils during installation and vacuum pump down on MAIZE. The effects of this structure are explored in Chapter II, where it is shown that the support rod plays a key role in the late time morphology of the instability structures.

this, university-scale thin-foil liners are constructed by wrapping an ultrathin sheet of metal foil (e.g., 400-nm-thick aluminum) around a dumbbell-shaped support structure (see Figure 1.2). The supported thin-foil liner is then installed between the anode and cathode of a pulsed power machine. Thin-foil liners of this type have been used in experiments on the MAIZE facility at the University of Michigan and on the COBRA facility at Cornell University [19, 21, 22, 25, 26]. The use of thin-foil liners on MAIZE and COBRA has enabled the study of helical instability structures like those seen in MagLIF experiments on the Z facility. Note that helical MRTI has also been observed in axially premagnetized gas-puff z-pinch implosions [18].

The origin of helical instabilities in axially premagnetized liner implosions is a topic of ongoing research within the community and has several proposed explanations ranging from low-density power-feed plasma being swept in from large radius and compressing the pre-imposed axial magnetic field up against the liner's outer

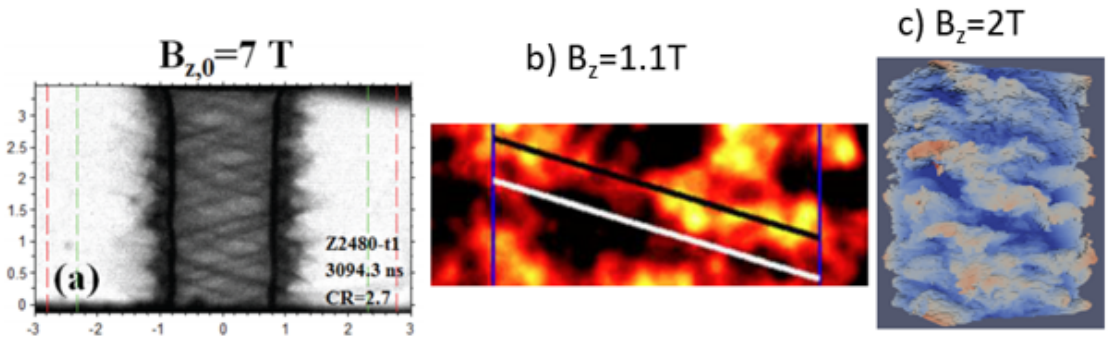

Figure 1.3: (a) Penetrating x-ray radiograph from Ref. [16], showing the helical nature of MRTI in an axially premagnetized MagLIF liner implosion experiment on the Z facility at Sandia National Laboratories. (b) Visible-light self-emission image showing helical instability structures from an axially premagnetized thin-foil liner implosion on the 1-MA MAIZE LTD at the University of Michigan, from Ref. [21]. (c) Image from PERSEUS showing a simulated axially premagnetized thin-foil liner implosion with helical MRTI without the need for artificial helical seeding.

surface, [20, 27] to electrothermal instability (ETI) effects [14, 17, 26, 28]. In Figure 1.3, three images are shown with helical MRTI. In Fig. 1.3(a), an x-ray radiograph is presented, showing some of the first reported helical MRTI structures observed in an axially premagnetized MagLIF experiment on the Z-machine [16]. In Fig. 1.3(b), a time-gated, visible-light, self-emission image from an axially premagnetized thin-foil liner experiment on MAIZE is presented [21]. In Fig. 1.3(c), an image from a 3-D PERSEUS simulation of an axially premagnetized thin-foil liner experiment is presented. It is important to note that there is no helical perturbation prescribed in PERSEUS to produce the helical MRTI; instead, a random density perturbation is seeded throughout the liner plasma, and yet helical MRTI still develops due to the pre-imposed B_z field. The simulation results shown in this dissertation make use of PERSEUS which was developed at Cornell University by Martin and Seyler [29]. The code is discussed in depth throughout this dissertation.

This dissertation presents a new explanation for the origin of helical instabilities

in axially premagnetized thin-foil z-pinches implosions. This explanation involves magnetic-field-aligned plasma effects due to a Hall Instability in the low-density coronal plasma immediately surrounding the dense liner. This new seeding mechanism arose from the following considerations. First, it has been found experimentally that very little plasma forms in the power feeds of university-scale (1-MA) pulsed power machines (without doing something very deliberate to generate plasma) [30]. Nevertheless, helical MRTI develops in axially premagnetized liner experiments at the 1-MA level [21]. Because of this, low-density power-feed plasmas are not included at large radius in the simulations of these experiments at the 1-MA level. Thus, significant compression of the pre-imposed axial field does not occur in our simulations, yet helical instabilities still develop as long as Hall physics is included in the simulations. This is in contrast to previous simulation studies also with Hall physics included, where MagLIF liner implosions on the much larger 20-MA Z facility were simulated, and power-feed plasmas were found to compress the pre-imposed axial magnetic field to significant levels on the liner's outer surface, making B_z comparable to the implosion-driving B_θ at the liner's outer surface [20]. Second, the simulations presented herein do not account for the initial solid-metal state of the thin-foil liner, and thus solid-metal ETI effects cannot be responsible for the helical instabilities observed in our simulations.

In recent experimental work [31, 32], a coronal plasma layer has been found to form around current-carrying thin-foils due to surface contaminant blow-off and out-gassing. In the Z-machine, low-density plasma is generated from out-gassing of not only the liner, but also the electrode surfaces due to the intense currents. In low-density plasma, a Hall interchange instability can develop, leading to several effects, including strongly force-free electron currents, axial magnetic field amplification, current advection, and bunching of both magnetic field lines and current density channels. To see an example of the effect of this instability on azimuthal current see Figure 1.4,

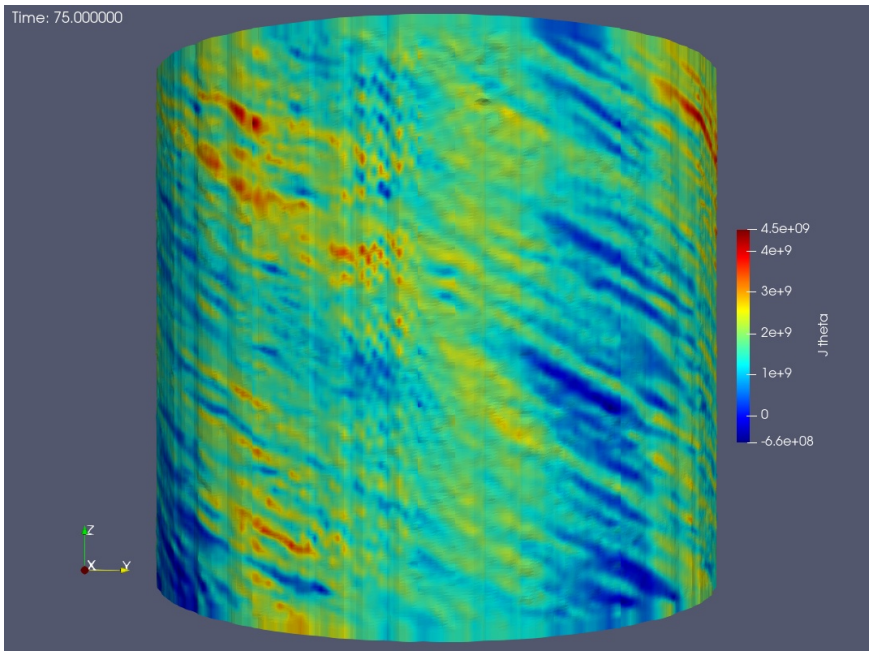

Figure 1.4: Helical perturbation in the azimuthal component of the current density, plotted on an iso-density surface (10^{24} m^{-3}) at 75 ns. This highlights one of the perturbation effects of the Hall interchange instability, which leads to helical formations in the current on the liner plasma outer surface.

where an iso-density of 1×10^{24} m^{-3} is shown with the azimuthal current plotted to show the strong helical patterning. Such dynamics can seed helical MRTI along the liner's outer surface and may cause other effects that have yet to be explored at Z-machine parameters. This form of the Hall interchange instability has been studied theoretically in Refs. [33–35] through analytic and computational methods. Other forms of Hall instabilities have been studied in Refs. [36–40].

1.2 PERSEUS: Magnetohydrodynamics and Hall physics

PERSEUS is an extended-magnetohydrodynamics (XMHD) code, which includes Hall physics (HMHD). PERSEUS was developed by Martin and Seyler [29] to explore high energy density physics with a new approach that allows the code to incorporate Hall physics and a large range of densities, covering over 9 orders of magnitude. This section will discuss the specifics of the code and how PERSEUS incorporates Hall

physics. The basic model given by:

$$\frac{\partial \rho}{\partial t} + \nabla \cdot (\rho \mathbf{u}) = 0 \tag{1.1}$$

$$\frac{\partial (\rho \mathbf{u})}{\partial t} + \nabla \cdot (\rho \mathbf{u}\mathbf{u} + \mathbf{I}p) = \mathbf{J} \times \mathbf{B} \tag{1.2}$$

$$\partial_t \varepsilon + \nabla \cdot [\mathbf{u}(\varepsilon + p)] = \mathbf{J} \cdot \mathbf{E} \tag{1.3}$$

$$\frac{\partial \mathbf{B}}{\partial t} + \nabla \times \mathbf{E} = 0 \tag{1.4}$$

$$\frac{\partial \mathbf{E}}{\partial t} = c^2(\nabla \times \mathbf{B}) - \frac{1}{\epsilon_0}\mathbf{J} \tag{1.5}$$

$$\frac{\partial \mathbf{J}}{\partial t} = -\nabla \cdot (\mathbf{u}\mathbf{J} + \mathbf{J}\mathbf{u} - \frac{1}{ne}\mathbf{J}\mathbf{J} - \frac{e}{m_e}\mathbf{I}P) + \frac{ne^2}{m_e}[\mathbf{E} + \mathbf{u} \times \mathbf{B} - \frac{1}{ne}\mathbf{J} \times \mathbf{B} - \eta \mathbf{J}], \tag{1.6}$$

where $n = \rho Z/(m_i)$ is the electron density, P is the total scalar pressure, and $P_e = ZP/(Z+1)$. These are solved using a combination implicit-explicit algorithm that makes use of a relaxation scheme to include low frequency Hall effects while maintaining timesteps comparable to MHD. Note the Hall term is the second to last term on the RHS of Equation 1.6.

1.2.1 Relaxation Model

A relaxation model is a useful way to recast a conservative hyperbolic system with a source term into a new system of equations that may be easier to solve numerically. These equations "relax" back to the original equation if the relaxation term, ϵ, approaches zero ($\epsilon \to 0$). To show this, consider the following simple one-dimensional example of a relaxation system:

$$u_t + F(u)_x = \frac{1}{\epsilon} S(u) \tag{1.7}$$

where u is a vector of variables, $F(u)$ is a vector of fluxes of u, and $S(u)$ is a stiff source term, meaning it must be handled over small time steps, as indicated by the $\frac{1}{\epsilon}$ term. As $\epsilon \to 0$, the equation relaxes to a solution with no source term since

$S(u)$ must go to zero or the RHS would become infinitely large. Note that u is still time dependent, but $S(u) = 0$ constrains the dynamics, and a proper solution to the system will correctly yield the dynamics of u and the equilibrium relaxation solution of $S(u) = 0$.

Any conservative hyperbolic system with source terms can be replaced by a synthetic relaxation system that will yield the original set of equations as the relaxation term becomes very large (i.e., $\epsilon \to 0$). A conservative equation is one in which the property being modeled is conserved, such as a continuity equation for mass, for example. When the relaxation term $(\frac{1}{\epsilon})$ becomes very large, it forces the source term to go to zero to stop that term from approaching infinity. This eliminates the source term and the system reverts to the relaxed form, which is the original system. For example, consider a 1-D system with the following hyperbolic equation:

$$u_t + F(u)_x = 0. \tag{1.8}$$

In the relaxation form, this is written as

$$u_t + v_x = 0 \tag{1.9}$$

$$v_t + H(v)_x = -\frac{1}{\epsilon}[v - F(u)]. \tag{1.10}$$

Therefore, as $\epsilon \to 0$, the bracketed term on the RHS of Eq. 1.10 (the source term) must go to zero. This means that $v = F(u)$ and the original system of Eq. 1.8 is recovered. Note that in the relaxation form, the vector of variables u_t is related to v_x by Eq. 1.9, and $H(u)$ becomes the vector of fluxes, while $F(u)$ becomes part of the source term. The reason for considering using this type of system is that it can lead to numerical methods that are much easier to solve relative to the ones needed to solve the original hyperbolic system.

1.2.1.1 Relaxation Model and the Generalized Ohm's Law

When the frequency, ω, for the phenomenon of interest is much less than the characteristic electron plasma and electron cyclotron frequencies ($\omega \ll \omega_{pe}, \Omega_e$), the generalized Ohm's law becomes a natural relaxation model, with the relaxation terms becoming the large terms on the right-hand sides of Equations 1.5 and 1.6. The large terms are determined by considering the ratio of the speed of light to a characteristic speed of the simulation. For example, terms with a c^2 coefficient are large, meaning that both terms on the RHS of equation 1.5 are retained. In addition, when considering the ratio of the characteristic spatial scale to the electron inertial length, the terms with a $1/m_e$ coefficient are retained from equation 1.6, which leads to equation 1.12. This leaves the following relaxation equilibrium:

$$\nabla \times \mathbf{B} = \mu_0 \mathbf{J} \tag{1.11}$$

$$\mathbf{E} + \mathbf{u} \times \mathbf{B} - \frac{1}{ne}\mathbf{J} \times \mathbf{B} - \eta \mathbf{J} = -\frac{1}{ne}\nabla P_e. \tag{1.12}$$

1.2.2 Vacuum Resistivity

In low-density regions in MHD, where there are not enough charge carriers to conduct current from the resistive Ohm's Law, issues can arise. This is due to the scalar nature of resistivity in high temperature plasmas being essentially independent of density, allowing for the current in low-density regions to be much higher than physically allowable (e.g., in reality, charge carriers cannot exceed the speed of light). Extended MHD with the Hall term gives rise to a tensor conductivity that is magnetic field dependent, which can greatly limit cross-field current. Also, the electron inertial terms inhibit instantaneous rise in parallel current until the electron-ion collisions limit the current flow. For resistive MHD, a model for the scalar resistivity that

depends on density and is very large in low density is often used:

$$\eta = \eta_s + \eta_0 \frac{n_{\text{floor}}}{n} \tag{1.13}$$

This simple model modifies Spitzer resistivity (η_s) with a vacuum resistivity (η_0). In PERSEUS, when XMHD or HMHD is used, the unmodified Spitzer resistivity is used, as the Hall and electron inertia terms are sufficient to restrict current in low density/vacuum regions. Note that the relaxation method used in PERSEUS for resistive MHD allows for the choice of an arbitrarily high vacuum resistivity without timestep concerns and without the need to track plasma/vacuum boundaries. This means that when PERSEUS is run using only resistive MHD (as opposed to using Hall MHD), the resistivity for low density plasma is properly handled and the choice for the vacuum resistivity constant (η_0) is relatively unimportant as long as it is large enough. Seyler and Martin [29] compared this resistive MHD model with the HMHD model and found good agreement. In XMHD or HMHD, the conductivity tensor, $\bar{\bar{\sigma}}$, has components that are Pederson, Hall, and parallel conductivities derived from setting the right-hand side of Eq. 1.12 to zero. This results in:

$$\mathbf{J} = \bar{\bar{\sigma}} \cdot (\mathbf{E} + \mathbf{u} \times \mathbf{B}). \tag{1.14}$$

Because this is a consequence of the Hall term, it is implicitly included in PERSEUS when using the XMHD model. The conductivity tensor and its components are discussed in detail in Ref. [20]. An important outcome of this conductivity tensor is that the parallel component is the most conducting term. This leads to the Hall term driving current along the magnetic field, which in turn can lead to a force free configuration of the current and magnetic field.

1.2.2.1 The Algorithm

Early versions of PERSEUS made use of an implicit-explicit MUSCL scheme (Monotone Upwind Scheme for Conservative Laws), which is a scheme developed by van Leer and is capable of handling systems with shocks and steep gradients. The equations are discretized using a finite volume approach that uses Local Lax-Friedrichs methods for flux calculations. This flux method is as follows:

$$F_{i+\frac{1}{2}} = \frac{F^{+}_{i+\frac{1}{2}} - F^{-}_{i+\frac{1}{2}}}{2} - c_s^2(n_{i+1} - n_i), \tag{1.15}$$

where c_s is a characteristic speed such as the sound speed, and the second term on the right-hand side is a diffusive/stabilizing term. This locally solves for characteristic speed instead of employing an expensive global solve scheme. If the electron inertial term ($\lambda_e^2 = m_e/n_0e^2\mu_0$), which is part of the relaxation term within the algorithm of PERSEUS, is under resolved (meaning it is smaller than the resolution of the simulation grid), the relaxation solution (Equation 1.11) is forced; conversely when the electron inertial scale is resolved, the model correctly solves for the current density. This is due to the electron inertial term being part of the relaxation term (see Ref. [29]). The time advance is implicit with respect to the Hall, resistive, and electron inertial terms. Because the Hall terms do not contain spatial derivatives, the algorithm only requires a direct solution of a 3×3 matrix at each cell. The flux terms and source terms in Equations 1.5 and 1.6 are treated explicitly.

For the simulations presented specifically in Chapter III, the version of PERSEUS used made use of a fifth order central finite volume method with a positivity preserving limiter that keeps the density and pressure above the floor [41]. This method allowed for a considerable accuracy improvement as compared with the third order method used in the simulations of Chapter II. Both methods are capable of handling $\gtrsim 9$ orders of magnitude density variation, from solid density down to the floor. The fifth

order method allowed for exploration of the seeding mechanism of helical instabilities which will be discussed in detail in Chapter III. In this method, the Hall-MHD Ohms law in Eq. (1.12) is solved using the relaxation method described in Section 1.2.1.1 and Reference [29]. The divergence constraint ($\nabla \cdot \mathbf{B} = 0$) is maintained using either divergence cleaning [42] or a constrained transport central difference method [43].

1.3 Plasma Instabilities

Z-pinches are an inherently unstable system and are subject to several different types of instabilities as discussed previously. The work presented in this dissertation focuses on two instabilities: magneto-Rayleigh-Taylor instabilities (MRTI) and Hall instabilities (HI), and this section will cover a theoretical discussion of these instabilities. First, MRTI is briefly discussed as it is perhaps the most ubiquitous instability in the field and has received the most study. Next, a discussion of the Hall instability is presented. Chapter III discusses how this Hall instability can seed MRTI and provide a new explanation for the helical instability structures observed in axially premagnetized z-pinches, which is still a topic of much debate within the field.

1.3.1 Magneto-Rayleigh-Taylor Instability

The Magneto-Rayleigh-Taylor Instability (MRTI) is very similar to the pure hydrodynamic Rayleigh-Taylor instability, where a lower density fluid is accelerated into a higher density fluid. In the pure hydrodynamic case, the Atwood number, $A = (\rho_{\text{heavy}} - \rho_{\text{light}})/(\rho_{\text{heavy}} + \rho_{\text{light}})$, is a dimensionless number that contributes to the growth rate of the Rayleigh-Taylor instability. In a magnetized plasma context, the density of the light fluid can be zero, and thus the Atwood number can be unity. This is because in MRTI, the lower density fluid can be fully (or partially) replaced by the magnetic field. In the analysis here, the magnetic field is an azimuthal field, B_θ, driven by the fast current pulse from the pulsed power machine (i.e., this is a

typical z-pinch configuration). This creates a magnetic field curvature, which along with $\mathbf{J} \times \mathbf{B}$ forces, acts like an acceleration term that drives the instability growth. If it is assumed that the magnetofluid is incompressible, then the linearized equation of motion becomes:

$$\rho_0 \frac{\partial \mathbf{v_1}}{\partial t} = -\nabla \bar{P}_1 + \frac{\mathbf{B_0} \cdot \nabla \mathbf{B_1} + \mathbf{B_1} \cdot \nabla \mathbf{B_0}}{\mu_0} - \rho_1 g \hat{\mathbf{y}}, \tag{1.16}$$

where $\bar{P}_1 = P_1 + \frac{\mathbf{B_0} \cdot \mathbf{B_1}}{\mu_0}$. The growth rate can be derived as shown in Bellan's textbook, *Fundamentals of Plasma Physics* [44], to be:

$$\gamma^2 \sim g \rho_0^{-1} \frac{\rho_0}{\partial t} - \frac{(\mathbf{k} \cdot \mathbf{B}_0)^2}{\mu_0 \rho_0}. \tag{1.17}$$

This MHD version of the Rayleigh-Taylor instability is also known as the Kruskal-Schwarzschild instability. Note that the $\mathbf{k}_0 = 0$ geometry is the fastest growing mode for this instability. In other words, the magnetic field can suppress the instability and slow its growth (if not stop it all together given a strong enough field), but this only occurs when the instability wave vector $\mathbf{k}$ is not aligned with $\mathbf{B}_0$. As discussed previously, axially premagnetized experiments such as MagLIF have an initial axial field, B_z ~7 Tesla, which is quickly dominated by the driving azimuthal field B_θ established by the 20-MA, 100-ns rise-time current pulse. This would imply that the fastest growing modes of the MRTI would be modes with $\mathbf{k} = k_z \hat{\mathbf{z}}$ (i.e., azimuthally symmetric modes with $m = 0$, where m is the azimuthal mode number). However, as discussed earlier, this is not the case—the MRTI structures are observed to be helical, with $m \geq 1$ and $\mathbf{k} = k_\theta \hat{\boldsymbol{\theta}} + k_z \hat{\mathbf{z}}$.

1.3.2 Hall-MHD Model and Reduced Model

In this section, a reduced Hall-MHD model is used to derive a local dispersion relation for the Hall interchange instability. This type of analysis is explored in a

similar context in References [33,34]. PERSEUS includes Hall physics by inclusion of the Hall term in the generalized Ohm's law (GOL), which is the 3rd term on the LHS of Equation 1.23 below. The Hall term is necessary to observe the effects discussed in this dissertation. The Hall-MHD model that will be used for this analysis is as follows:

$$\partial_t n + \nabla \cdot (n\mathbf{u}) = 0 \tag{1.18}$$

$$\partial_t(\rho\mathbf{u}) + \nabla \cdot (\rho\mathbf{u}\mathbf{u} + p) = \mathbf{J} \times \mathbf{B} \tag{1.19}$$

$$\partial_t \varepsilon + \nabla \cdot [\mathbf{u}(\varepsilon + p)] = \mathbf{J} \cdot \mathbf{E} \tag{1.20}$$

$$\partial_t \mathbf{B} = -\nabla \times \mathbf{E} \tag{1.21}$$

$$\nabla \times \mathbf{B} = \mu_0 \mathbf{J} \tag{1.22}$$

$$\mathbf{E} + \mathbf{u} \times \mathbf{B} - \frac{1}{ne}\mathbf{J} \times \mathbf{B} - \eta\mathbf{J} = 0, \tag{1.23}$$

where $\varepsilon = \frac{1}{2}\rho u^2 + p/(\gamma - 1)$ is the internal energy density, and the average ionization is assumed to be one ($Z = 1$). Equations 1.18–1.20 are the continuity equations for mass, momentum, and energy respectively, while Eqs. 1.21 and 1.22 are Faraday's and Ampère's law. Equation 1.23 is the generalized Ohm's law with the Hall term included. The variables $\mathbf{u}$, $\mathbf{J}$, $\mathbf{E}$, $\mathbf{B}$, ρ, n, p are velocity, current, electric field, magnetic field, mass density, number density, and pressure.

The reduced description of these equations is an asymptotic analysis in which the constant equilibrium axial field B_0 is much larger than either the perturbed axial field or the transverse field, i.e., $B_0 \gg B_z$ and $B_0 \gg B_\perp$. We take $\partial_z \ll \nabla_\perp$, meaning that the perturbations in the axial direction are much smaller than the perturbations in the perpendicular field, which is consistent with the previous assumption, so that $B_0\partial_z \sim B_\perp \cdot \nabla_\perp$. The mass velocity is taken to be small but not zero. The pressure perturbations are assumed to be zero, as is the plasma resistivity. The most familiar application of this scaling leads to the so-called reduced MHD equations, sometimes

called the Strauss equations [45]. The application here is to the Hall-MHD equations in the frequency range between the ion and electron cyclotron frequencies. The high-frequency reduced Hall-MHD model, applicable to plasma motion faster than the ion gyrofrequency and slower than the electron gyrofrequency, consists of the following equations [33, 34]:

$$\partial_t \phi = \frac{1}{n_0 e \mu_0}[(\hat{z} \times \nabla\psi) \cdot \nabla\nabla_\perp^2 \psi + B_0 \partial_z \nabla_\perp^2 \psi + B_0 \nabla_\perp^2 \chi + \frac{B_0}{n_0}(\hat{z} \times \nabla n) \cdot \nabla\phi] \quad (1.24)$$

$$\partial_t \psi = \frac{1}{n_0 e \mu_0}[(\hat{z} \times \nabla\psi) \cdot \nabla\phi + B_0 \partial_z \phi] \quad (1.25)$$

$$\partial_t \chi = -\frac{B_0}{\rho_0 \mu_0}\phi \quad (1.26)$$

$$\partial_t n + n_0 \nabla_\perp^2 \chi = 0, \quad (1.27)$$

where $\phi = \delta B_z$ is the perturbed axial magnetic field, ψ is the magnetic flux function, from which $B_\perp = \hat{z} \times \nabla\psi$, χ is the velocity potential. For high frequencies the velocity is completely compressible such that $\mathbf{u}_\perp = \nabla_\perp \chi$. Equations 1.24 and 1.25 are derived from Faraday's law using the Hall-MHD Ohm's law (Equation 1.23). Equation 1.26 is the linearized momentum equation for purely compressible modes, and Eq. 1.27 is the continuity equation for purely compressible motion. The reduced equations are adequate for analyzing the stability about an equilibrium satisfying the stated approximations.

These equations can be linearized about a slab equilibrium with $B_{0z}(x) = B_0 + \phi_0(x)$, $n_0(x)$ (i.e., a density profile in x), and $B_{0y}(x) = \psi_0'(x)$, where the prime means differentiation with respect to the argument. Additionally, a space-time dependence that is consistent with local analysis can be assumed for the equilibrium and perturbation fields (the terms with δ in the equations below) such that the perturbation

fields do not have any dependence on x:

$$B_z(x,y,z,t) = B_0 + \phi_0(x) + \delta\phi \exp[i(k_y y + k_z z - \omega t)] \tag{1.28}$$

$$B_\perp(x,y,z,t) = B_{0y}(x) + \delta\psi \exp[i(k_y y + k_z z - \omega t)] \tag{1.29}$$

$$\chi(x,y,z,t) = \delta\chi \exp[i(k_y y + k_z z - \omega t)] \tag{1.30}$$

$$n(x,y,z,t) = n_0(x) + \delta\mathrm{n} \exp[i(k_y y + k_z z - \omega t)]. \tag{1.31}$$

The linearized form of this reduced model is then:

$$\begin{aligned} -i\omega\delta\phi = \frac{1}{n_0 e\mu_0}[&-ik_y^3\delta\psi\psi_0'(x) - ik_z k_y^2 B_0\delta\psi + \psi_0''' \\ &+B_0(-k_y^2)\delta\chi + \frac{B_0}{n_0}(n_0'(x)ik_y\delta\phi - ik_y\phi_0'(x)\delta n] \end{aligned} \tag{1.32}$$

$$-i\omega\delta\psi = \frac{1}{n_0 e\mu_0}[ik_y\delta\psi\phi_0'(x) + ik_y\delta\phi\psi_0'(x) + ik_z B_0\delta\phi] \tag{1.33}$$

$$-i\omega\delta\chi = \frac{-B_0}{\rho_0\mu_0}\delta\phi \tag{1.34}$$

$$-i\omega\delta n + n_0(-k_y^2)\delta\chi = 0. \tag{1.35}$$

Combining and solving Eqs. 1.32–1.35 gives the local dispersion relation:

$$\omega^2[(\omega-\omega_H)\omega - \omega_0(\omega-\omega_H) - k^2\sigma^2] - k^2 v_A^2(\omega^2-\omega_H^2) = 0, \tag{1.36}$$

where $v_A^2 = B_0^2/\rho_0\mu_0$ (v_A is the Alfvén speed), $k = k_y$, $\omega_0 = k\frac{B_0 n_0'}{n_0^2 e\mu_0}$, $\omega_H = k\frac{\phi_0'}{n_0 e\mu_0}$, $\sigma \equiv [kB_{0y}(x)+\kappa B_0]/(n_0 e\mu_0)$, and $\kappa = k_z$. This gives unstable solutions, requiring ω_H to be non-zero. For relevant plasma parameters (e.g., $B_0 = 2$ T, $n_0 = 6\times10^{20}$ m^{-3}, and $k = 0.4$ mm^{-1}), the dispersion relation in Eq. 1.36 gives growth rates of approximately 0.12 ns^{-1}. This growth rate will be compared to simulation results in Chapter III. Note, this instability requires a gradient in the axial magnetic field. The density gradient can work to either make the growth rate larger or smaller depending on whether the density gradient is the same or opposite sign to the magnetic field at the

same local radius. This means that at early times, the maximal growth rate occurs where the density falls off rapidly ($n_0' < 0$) and the axial magnetic field gradient has $B_z' > 0$.

CHAPTER II

Extended Magnetohydrodynamics Simulations of Thin-Foil Z-Pinch Implosions with Comparison to Experiments

In this chapter, simulations of thin-foil liner z-pinches are shown that explore several effects related to the support rod structure that is necessary to hold the thin-foil liner upright in MAIZE's anode-cathode gap prior to the implosion. The radius of this support rod sets a limit on the maximum convergence ratio achievable for the implosion. In recent experiments with a support rod and a pre-imposed axial magnetic field, helical instability structures in the imploding foil plasma were found to persist as the foil plasma stagnated on the rod and subsequently expanded away from the rod [21]. The PERSEUS simulation results presented in this dissertation suggest that it is the support rod which is responsible for the helical structures persisting beyond stagnation. Furthermore, the simulations show that as the radius of the support rod decreases (i.e., as the convergence ratio increases), the integrity and persistence of the helical modes diminish. In the limit with no support rod, the simulations show that the structure of the final stagnation column is governed by the structure of the central precursor plasma column.

2.1 Thin-Foil Z-Pinches

To study metal liner implosion instabilities on a university-scale pulsed power machine ($\sim$1 MA in 100 ns) requires a significant reduction in liner wall thickness relative to MagLIF liners on Z. Thinner liner walls are needed to reduce the overall liner mass while preserving the initial liner radius of 3 mm. Thin liner walls can be achieved by wrapping a sheet of thin metal foil (e.g., 400-nm-thick aluminum) into the shape of a cylinder. Thin-foil liners of this type have been used in experiments on the MAIZE facility at the University of Michigan [19, 25, 46], and the COBRA facility at Cornell University [22, 47]. Because the foil liners are so thin, they are also incredibly fragile and require a support rod structure (Figure 1.2) to ensure their structural integrity when handling (e.g., during liner assembly and installation into the MAIZE anode-cathode structure) as well as during vacuum pump-down on MAIZE, where the gap spacing of the anode-cathode structure can decrease by $\sim$1 mm in the axial direction of the liner as the MAIZE facility's mechanical deflection of the top vacuum lid due to the 1 atm pressure differential.

The development of an imploding thin-foil liner platform on MAIZE enabled subsequent experimental studies on liner implosion dynamics. These studies included experiments with axially premagnetized liners, where discrete helical modes were observed [19, 21, 25]. In thin-walled foil liner experiments [21] and in thick-walled MagLIF liner experiments [14], the helical pitch angle ϕ and the azimuthal mode number m of the helical instability structures were found to be governed by the strength of the initial applied B_z field. Additionally, the pitch angle in both the thin and thick-walled cases can be described by the relationship $\phi \approx m/(kR)$, where k is the axial wave number, and R is the imploding liner radius at the time of the image, while the helical pitch $p = 2\pi m/k$ was found to be approximately constant in both the thin- and thick-walled cases for the implosion times observed [14], [21]. (Note that the helical pitch is the axial distance traveled along a helix when advancing by 2π

radians in the azimuthal direction; the pitch is not the pitch angle.) The similarities observed between the two cases are remarkable given that thin-foil liners are much more susceptible to instability feedthrough than thick-walled MagLIF liners. For example, a liner's robustness to instability feedthrough is often characterized in terms of the liner's initial aspect ratio $AR_0 \equiv R_{\text{outer},0}/\Delta R_0$, where $R_{\text{outer},0}$ is the initial radius of the liner's outer surface, and AR_0 is the liner's initial wall thickness. Smaller AR_0 liners are expected to be more robust than higher AR_0 liners, while higher AR_0 liners can obtain higher implosion velocities. In MagLIF, the tradeoff between implosion velocity and liner stability is expected to result in optimum fusion performance with $\Delta R_0 \sim 6$ liners, which have been studied extensively on Z [13–15, 17]. By contrast, the thin-foil liners studied in Refs. [19, 21, 25] and [26], have $\Delta R_0 \sim 6000$. Another important difference between the thin and thick-walled cases is the fact that the wall thickness in a MagLIF liner is usually greater than the electrical skin depth of the liner material, whereas in thin-foil liner experiments, the resistive skin depth is much greater than the liner wall thickness. This causes thin-foil liners to explode (expanding the wall thickness) very early in the current pulse, due to the stresses caused by intense ohmic heating. By contrast, MagLIF liner walls are usually compressed by the driving magnetic pressure gradient, sometimes leading to shock formation within the thick liner wall [15]. For the thin-foil liner experiments, the early expansion of the foil thickness prior to the start of the implosion effectively reduces the initial aspect ratio to $\Delta R_{0,\text{effective}} \sim 15$, which could help explain some of the similarities observed between initially thin and thick-walled cases.

2.2 Simulations of Previous Experiments Conducted on MAIZE

An overview of the initial 3D PERSEUS simulation geometry and some example images of the imploding liner plasma are presented in Figure 2.1. As in the experiments, the simulations included a pre-imposed axial magnetic field of 2 T. The liner

plasma density was mass matched to represent a 400-nm-thick aluminum foil liner expanded out into a 1 eV cylindrical plasma shell with a wall thickness of 250 microns. The density perturbation of less than 1% was randomly distributed throughout the liner plasma. PERSEUS was also modified to read in an experimentally measured current pulse to drive the implosion (see Figure 2.2) in this chapter. A Spitzer resistivity model was used in these simulations.

A detailed discussion of the grid resolution used can be found in Appendix B. The PERSEUS implosion trajectory presented in Figure 2.2 was extracted from the simulation data presented in Figure 2.1. To obtain the PERSEUS radii plotted, several 1D radial density profiles were acquired from the PERSEUS simulation data at various axial positions (z) and for various azimuthal directions (θ). The outer edge of each radial profile was then recorded by considering the steep drop off in density. The averages of these positions are the PERSEUS radii plotted in Figure 2.2, while the standard deviations determine the error bars.

At present, PERSEUS only allows for a single material to be modeled. Thus, to model both the imploding aluminum plasma shell and the plastic support rod, the support rod was initialized as cold, solid density aluminum with its conductivity artificially decreased so that it was non-conducting. A momentum mask (which prevented any movement of the rod due to thermal expansion or ablation by artificially imposing zero momentum at every timestep while active) was also applied to the rod during the liner implosion phase and then removed at a time just before liner stagnation. This was done to prevent rod ablation from impacting the inner surface of the imploding liner. To mimic ionization of the rod's surface, a thin (2-cell) layer of low-density plasma was initialized around the rod. This allowed for the flow of a small amount of current along the rod's surface. It is difficult to know the exact behavior of the rod since it has not been explored in experiment, but this approach is believed to be reasonable and sufficient for the purposes of this study.

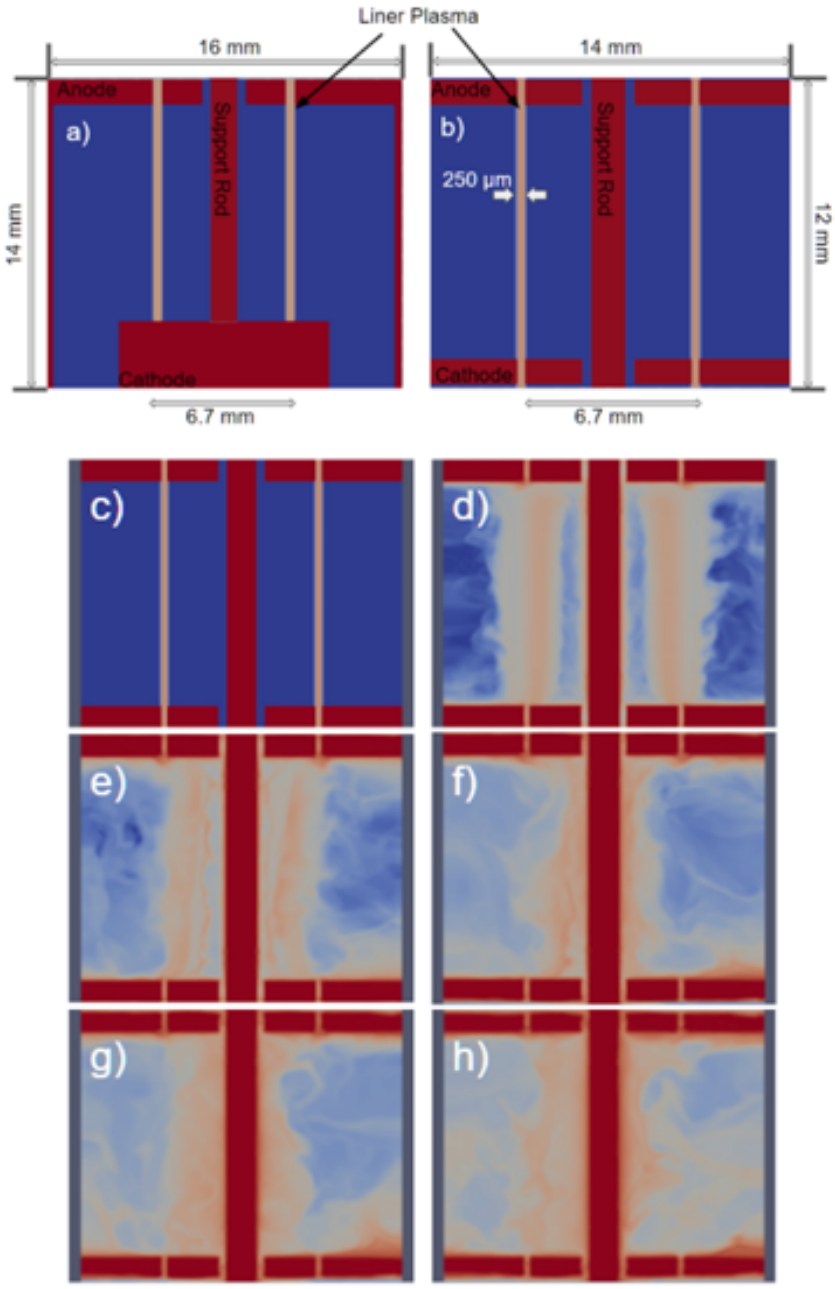

Figure 2.1: Simulation setups and implosion overview. (a,b) Initial setups showing examples of the electrode geometries and power feeds used, where red represents solid density aluminum and blue is vacuum. The setup in (a) includes an axial feed and was driven by a boundary condition at the lower edge of the image (i.e., at a specified axial position). The setup in (b) used a simplified electrode geometry and was driven by a boundary condition at the left and right edges of the image (i.e., at a specified radius). It was found that including the axial feed was unnecessary and only added unnecessary volume to the simulation space, reducing the grid resolution; thus, the setup in (b) was used for most of this chapter. (c)-(h) Example density slices taken during a representative liner implosion.

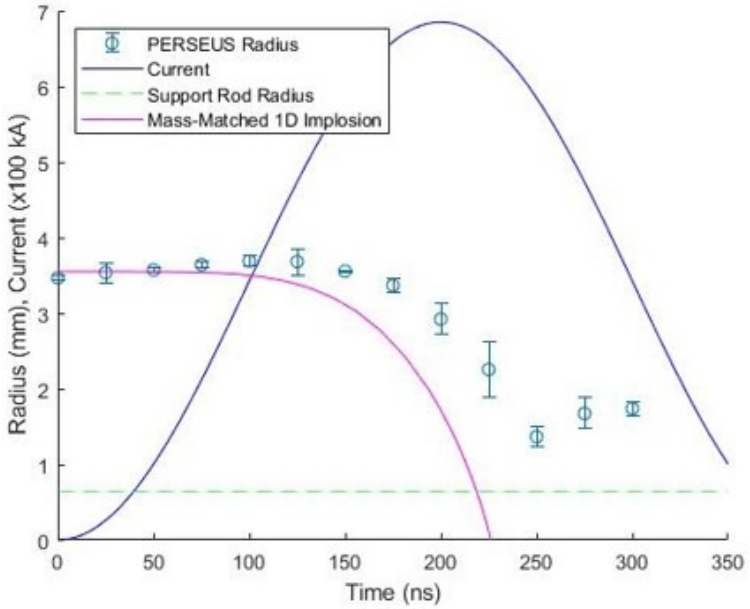

Figure 2.2: Simulated liner implosion trajectories from PERSEUS and from a simplified 1-D thin-shell model, as well as the MAIZE electrical current used to drive the simulated implosions. The average liner radius plotted for PERSEUS was found by integrating the liner density in both the axial (z) and azimuthal (θ) directions. This figure should be contrasted with Fig. 1b in Ref. [19]. The simplified 1-D thin-shell simulation (sometimes referred to as a "0-D" model) is shown for reference and demonstrates that PERSEUS captures early time expansion of the liner and late time bounce of the liner off of the inner support rod, which can also be seen in experiment (see Fig. 1b in Ref. [19]).

In Figure 2.2, the PERSEUS liner trajectory reaches stagnation just after the time when the current reaches its maximum value. The stagnation phase begins when the liner begins to decelerate due to plasma pressure building up between the imploding liner wall and the support rod on axis. During stagnation, the liner trajectory appears to undulate. This is due to shocks reverberating in the plasma between the imploding liner wall and the support structure on axis. After stagnation, the liner trajectory enters the explosion phase. In Figure 2.2, the duration of the implosion phase is approximately 125 ns, and the duration of the stagnation phase is approximately 50 ns. These durations are in good agreement with those observed experimentally in Ref. [19], Fig 1 (b).

In our PERSEUS simulations, and in the experiments of Refs. [19, 21, 25, 46], the on-axis support rod sets a maximum possible convergence ratio of $C_{r,\max} \equiv \frac{r(0)}{r_{\rm rod}} = 5.15$. However, this $C_{r,\max}$ is never achieved in the simulations or observed in the experiments (note that the experiments only observed the outer edge of the imploding liner plasma). At least for the simulations (and possibly for the experiments), this is due to an appreciable amount of low-density plasma being advected to the support rod ahead of the bulk of the imploding liner material. This advected "precursor" plasma accumulates along the rod while also carrying an appreciable amount of current ($\sim$30%). This precursor plasma, with its associated plasma pressure and magnetic pressure, is compressed by the imploding liner material, which limits the convergence ratio to something less than $C_{r,\max}$.

Overall, the simulated trajectory in Figure 2.2 is very similar to what was found in the experiments (again see Fig. 1(b) in Ref. [19]). However, one notable difference is that the liner begins imploding earlier in the simulated case (both PEREUS and the simple thin-shell model). In experiments, the liner began the implosion phase around 125 ns into the current pulse, while in PERSEUS, the liner begins the implosion phase around 75 ns into the current pulse. This results in the PERSEUS liner

reaching stagnation earlier than in the experimental case. This discrepancy could be due to the use of a Spitzer-Harm conductivity model, which lacks the ability to model the precipitous drop in conductivity that occurs when the solid metal foil transitions to a liquid-vapor state. By artificially varying the conductivity values, the implosion timings were found to vary by 10s of nanoseconds, where higher conductivity values lead to earlier implosion times, because larger gradients in the implosion-driving magnetic field pressure can be supported. The conductivity values were varied through a weighting factor that determines the relative weight of a fixed conductivity value versus a value calculated using the coulomb logarithm. From these two values, an overall conductivity value for each cell is calculated.

Another possible explanation for the discrepancy in the overall implosion times is that perhaps the current delivered to the load in the experiments was lower than the measured value. For example, the load current diagnostics in the experiments of Refs. [19, 21, 25] were B-dot probes located at a radius of 45 cm, which is large compared to the radius of the liner (3 mm). This means that any current loss occurring between the probe locations and the liner surface would go undetected while also causing a later-than-expected implosion time, given the measured current trace. To test this explanation, a simple PERSEUS simulation was run, which showed that lowering the current by 15% caused the liner to implode $\sim$25 ns later. Furthermore, in the experiments of Ref. [19], the peak current varied from shot to shot by up to 20% of the average peak current measured. Meanwhile, our PERSEUS simulations in this chapter used the current trace from the experiment with the highest peak current (shot 1172, with a peak current of 680 kA). Thus, the shot-to-shot variations and the measurement uncertainties could explain much of the differences observed in the implosion times. Note that efforts are presently underway to improve load current measurements on MAIZE and thus further address this issue in the future [48]. Despite the discrepancy in the start time of the implosion phase, the simulated durations

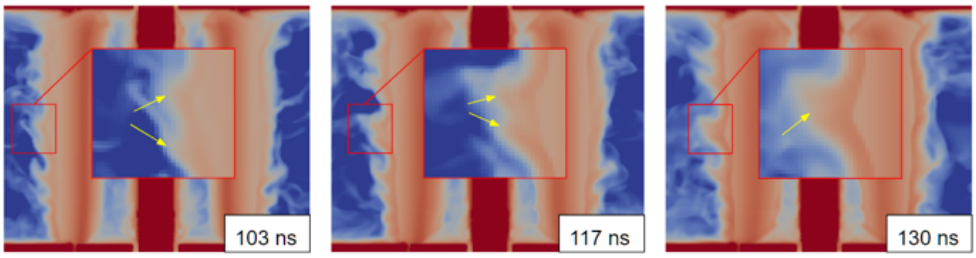

Figure 2.3: Mode merging of instability lobes in simulation. The duration of this single mode-merging event is approximately 30 ns. Both the duration and the overall dynamics of this mode-merging event agree well with the experimental results presented in Fig. 7(b) of Ref. [21].

of the implosion and stagnation phases are in good agreement with experiment.

During the implosion phase, instability structures begin to develop. Considering the axial mode number (spatial frequency) $k_z = 2\pi/\lambda$, where λ is the wavelength of the instability in the axial direction, the first modes to appear are short-wavelength modes (high spatial frequency), which cascade to larger wavelength modes throughout the implosion [13, 21]. This cascading process occurs via a series of discrete mode merger events [21]. The discrete mode merger events observed in the PERSEUS simulations (see Figure 2.3) appear very similar to those observed in experiments (see Fig. 7(b) in Ref. [21]). In both the simulation and in the experiment of Ref. [21], the discrete merging of two instability lobes occurs over a period of approximately 30 ns.

As the instability structures cascade to longer wavelengths, they also grow to larger amplitudes [13, 21]. In Figure 2.4, the PERSEUS instability amplitude is presented as a function of normalized distance moved, $\hat{d} \equiv 1 - r(t)/r(0)$. To obtain these amplitudes, the edge of the imploding plasma column (at an iso-density surface of 10^{23} m^{-3}) is tracked and fit with a sum of sine functions (the fitting was done using the MATLAB "sin8" fitting routine). This resulted in an average instability amplitude for each time step that was analyzed. The amplitude data were then fit with an exponential function of the form $A = A_0 \exp(\gamma t)$, where A_0 is determined by the initial seeding and γ is the growth rate. Since a random density perturbation was used in

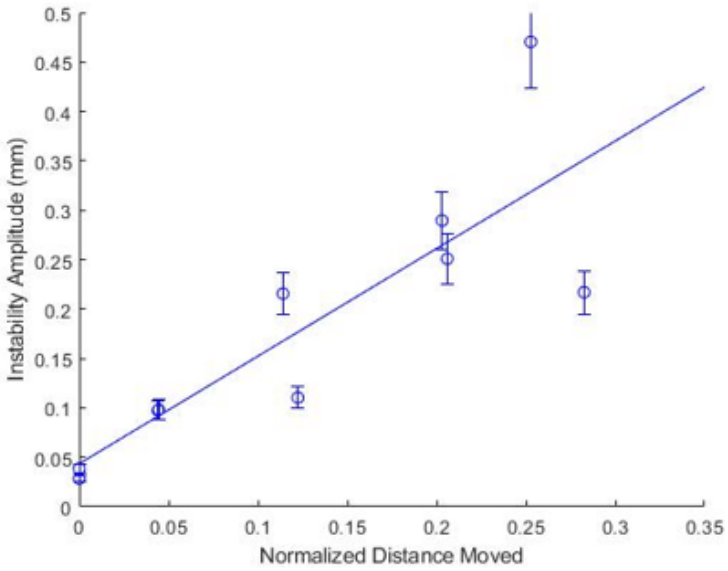

Figure 2.4: PERSEUS instability amplitude as a function of normalized distance moved, $\hat{d} \equiv 1 - r(t)/r(0)$. The instability amplitude is subject to the iso-density surface chosen and becomes difficult to determine as the liner begins to bounce off of the inner support rod. This is due to the lower effective resolution as the imploding liner moves through the cartesian grid, which can make it difficult to determine an accurate instability amplitude.

these simulations, A_0 was not well defined (i.e., this is a perturbation to density rather than a perturbation to the liner-vacuum interface). Nevertheless, the exponential fits allow us to determine the growth rates and an effective A_0. The simulated growth rate was 34.5 $\pm$ 5.5 μs^{-1}, which was $\sim$3 times larger than the experimentally measured values, which typically ranged from 7 to 13 μs^{-1}. However, in this particular case, the experiments of Ref. [21] were non-imploding in order to investigate magnetic compression instability development decoupled from the acceleration-driven MRT instability. Thus, it is not surprising that the overall instability growth rates in the PERSEUS simulations (which do include MRT contributions) are larger than in the experiments of Ref. [21]. The uncertainty in the simulated growth rate is largely due to limitations in spatial resolution. The lack of resolution causes aliasing to occur (on a Cartesian grid) that influences the measured growth rate at different azimuthal locations on the liner. This means that the measured growth rate can depend on the azimuthal viewing angle. The effect of viewing angle is driven by mode merging events at different azimuths around the liner occurring at different times. In simulations, the effects of viewing angle can be mitigated by rotating the 3D data such that the chosen viewing angle for data analysis takes into account the azimuthally asymmetrical mode merger events. This is not possible in experiment, thus viewing angle effects may play a more significant role in experiment.

Helical modes were observed in all simulations run with $B_{z0} \neq 0$ (see Figure 2.5). To characterize these modes, we used the analysis technique presented by Awe et al. [14], where the observed helical structures can be fit using the parametric equations: $y(\theta) = a \cdot \sin(\theta)$, and $z(\theta) = p \cdot \theta / 2\pi$. Here, a is the radius of the imploding liner at the time of the image, and p is the pitch of the helix. Note that p remains approximately constant throughout the implosion, which is consistent with the fact that axial plasma outflows are not permitted in the experiments or the simulations. Presented in Figure 2.5(a) is a series of helical lobes highlighted on the surface of the

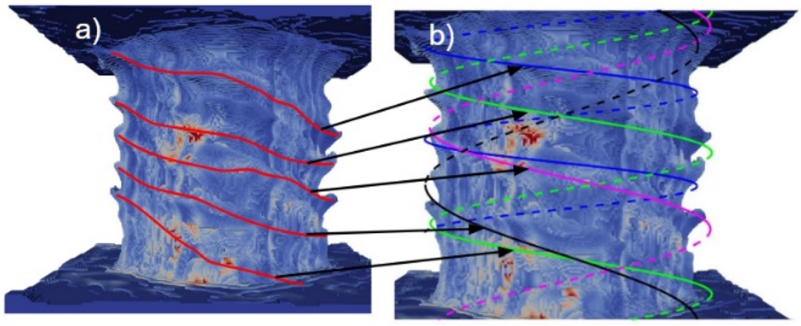

Figure 2.5: Iso-density surface images taken at a number density of 6×10^{18} cm^{-3} and a time of 117 ns, showing (a) the highlighted helical instability lobes that develop on the liner and (b) the corresponding helical line traces used to identify the effective azimuthal mode number. The origin of these helical instabilities is being studied and will be presented in depth in III.

liner (an iso-density surface taken at a number density of 6×10^{18} cm^{-3}). In Figure 2.5(b), we show the corresponding helical traces from the parametric equations above; these parametric fits are used to identify the effective azimuthal mode number.

The choice of iso-density surface was made such that the instability structures were the most pronounced. This typically meant a surface iso-density of 6×10^{18} cm^{-3}. Changing this value by an order of magnitude higher or lower does not affect the results presented in this Chapter. Note that if the density threshold for the iso-surface is set too low, then random clumps of low-density plasma begin to obscure a decent view of the helical structures, while if the density threshold is set too high, the structures are not present.

The parametric fitting technique is able to trace well-defined helical lobes, but it does not handle the more complex structures that result from discrete mode merging events that occur at different azimuths at different times. Nevertheless, this simplified tracing method is included to capture the general trends of the mode development and to give a rough idea of the effective azimuthal mode number (i.e., the number of intertwined helices) which was confirmed by rotating the 3D data. The results from this analysis for six different times can be seen in Figure 2.6. Late in time, the modes

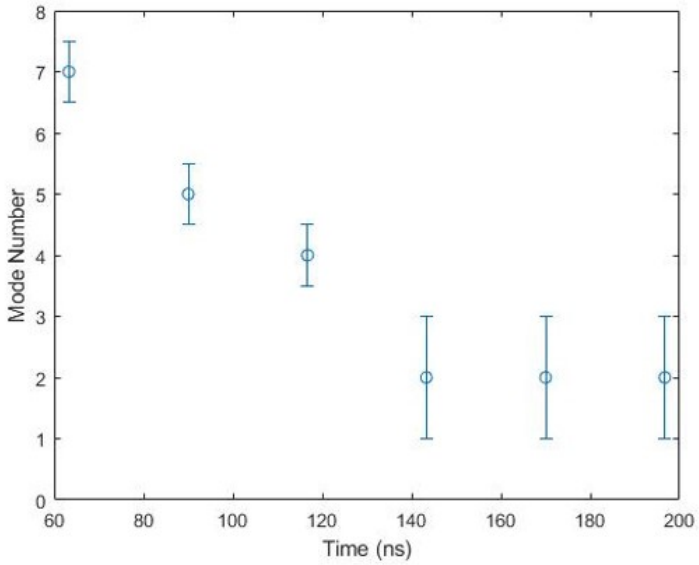

Figure 2.6: Effective azimuthal mode number m as a function of time. The mode numbers were extracted from the simulation data using the helical fitting technique described by Awe et al. in Ref [14]. This technique uses the parametric equations given in the text to trace 3D helices onto a 2D image. The results plotted here indicate that the instability structure initially consists of many intertwined helices ($m \approx 7$), and that these helices merge into fewer helices throughout the implosion process. The mode merging ceases upon stagnation ($t \approx 140$ ns), with a dominant mode number of $m \approx 2$ (two intertwined helices). These results are consistent with the experimental results presented in Refs. [25] and [21].

become less pronounced as the plasma becomes denser and choosing an optimal iso-density surface becomes more challenging. These traces indicate that the number of intertwined helices early in time is quite large ($m \approx 7$) compared to the final number at stagnation ($m \approx 2$). This analysis also shows that one helical trace can become very close to another helical trace (see Figure 2.5), which is a consequence of instability lobes being in the process of merging (Figure 2.3). Also note that since the helical modes are almost always in a state of merging, the effective azimuthal mode number is rarely (if ever) an exact integer value, hence the uncertainties indicated in Figure 2.6. Note that the experimental data of Refs. [19, 21, 25] were acquired using laser shadowgraphy (with a laser wavelength of 532 nm) and visible self-emission imaging. A straightforward way to compare the PERSEUS simulation results to the experimental results would be to use PERSEUS simulation output data to generate synthetic laser shadowgraphs and self-emission images. However, PERSEUS is presently not equipped to do this.

2.3 Axial Roll-Up of Instability Structures in Thin-Foil Liner Simulations

In the simulations of thin-foil liner implosions presented throughout this dissertation, a velocity shear is observed in the axially directed plasma flow near the outer edge of the low-density plasma. This causes the MRT instability lobes to roll over in the upwards direction (like breaking waves). This shear is the result of electron flow in the low-density plasma ($< 6 \times 10^{22}$ m^{-3}), which establishes electric and magnetic fields that drive these roll-up features.

In Figures 2.7 and 2.8, an example is shown of the axial roll-up features. These images were produced using a number-density iso-surface of 1×10^{24} m^{-3}. In Figures 2.7 and 2.8, the plasma on the outer tip of the instability lobe has more upward

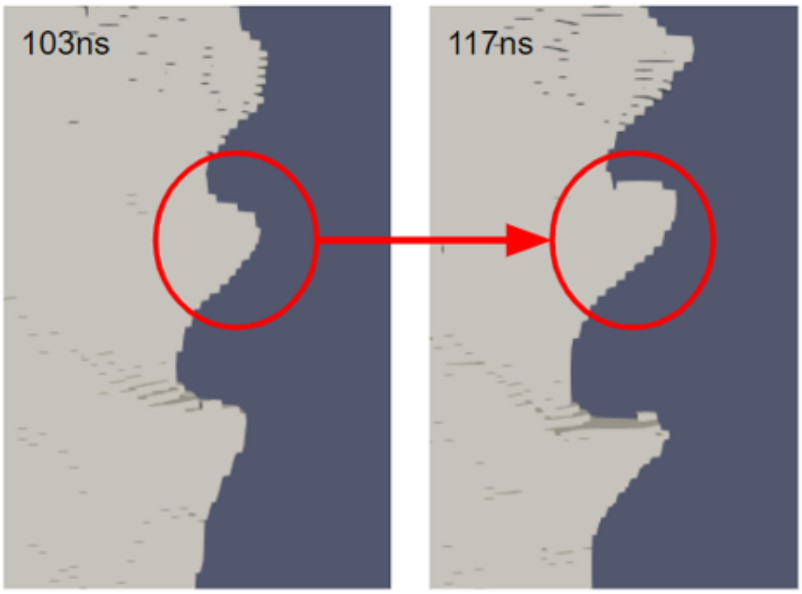

Figure 2.7: Two timesteps from a 3D liner implosion which shows a helical instability lobe exhibiting axial roll-up characteristics in the liner plasma. This is driven by radially dependent $\mathbf{E} \times \mathbf{B}$ velocity shear within the plasma.

axial velocity v_z than the plasma further inward on the lobe. The velocity shear in the instability lobes was quantified using the probe locations indicated in Figure 2.8. The measured axial velocities v_z(r) are plotted in Figure 2.9. In Figure 2.8, probes 1, 2, and 3 show a clear velocity shear, where the plasma at larger radii have a larger v_z. This leads to the roll-up features illustrated in Figures 2.7 and 2.8. This is less pronounced in probe 4, but the trend is still there to a smaller extent.

In Figure 2.10, both electric and magnetic fields are plotted. When evaluating the $\mathbf{E} \times \mathbf{B}$ drift, it is found that above the lobe, the $\mathbf{E} \times \mathbf{B}$ drift is inward (into the page, towards the center of the liner on the axis of symmetry), while below the lobe, the $\mathbf{E} \times \mathbf{B}$ drift is outward. The flow of plasma is complicated and nonuniform during the implosion of the liner, but these $\mathbf{E} \times \mathbf{B}$ drifts bias that flow and drive the roll-up features.

In Figures 2.11 and 2.12, the components of $\mathbf{E} \times \mathbf{B}$ are plotted when the current pulse has reached peak current (at 200 ns) and significant helical MRTI structures have formed and are beginning to exhibit roll-up features. In Figure 2.11, the radial

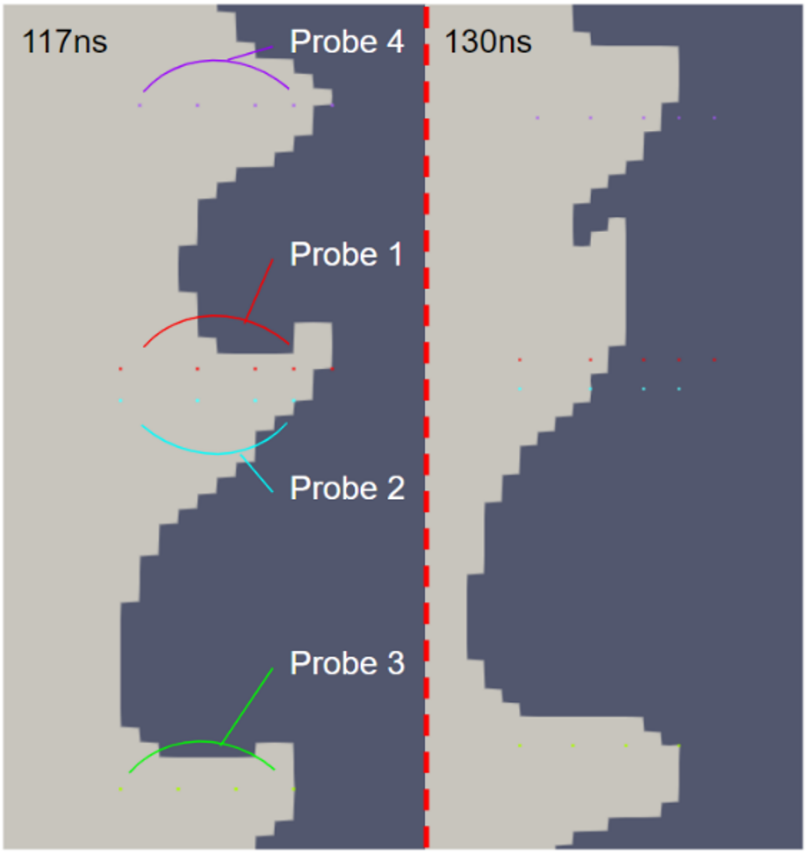

Figure 2.8: Slice from a 3D simulation showing the 4 probe locations used to map the velocity values $v_z(\mathrm{r})$ plotted in Fig. 2.9. This slice view also highlights the roll-up behavior of the MRT instability lobes.

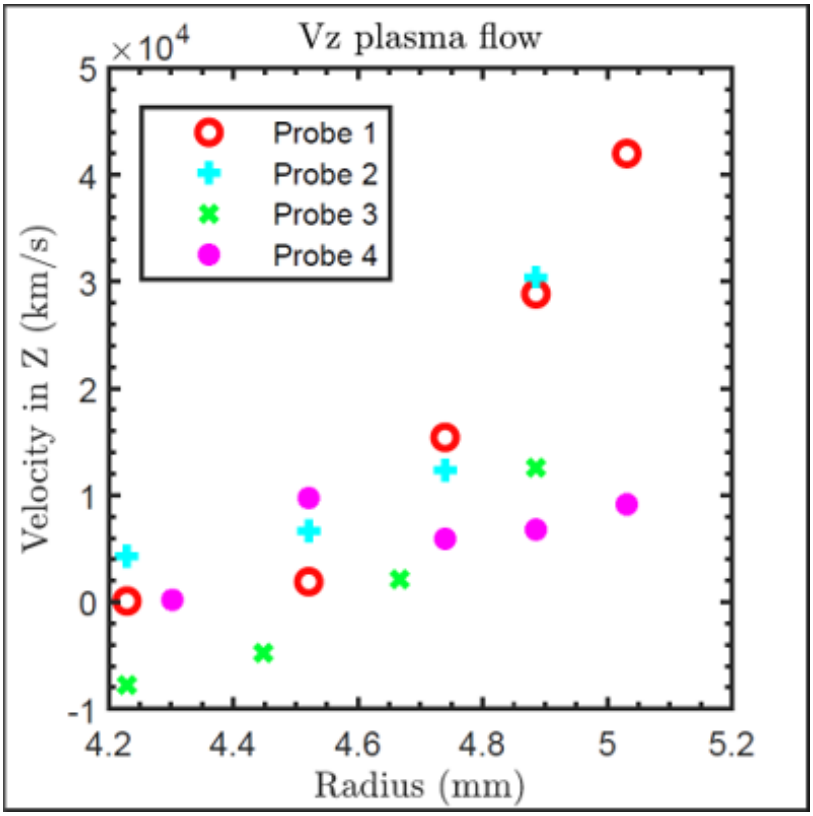

Figure 2.9: Graph of upward velocity $v_z(r)$, revealing the velocity shear present in the instability lobes (i.e., the plasma has larger values of v_z at larger radii). These velocity measurements were taken at 117 ns.

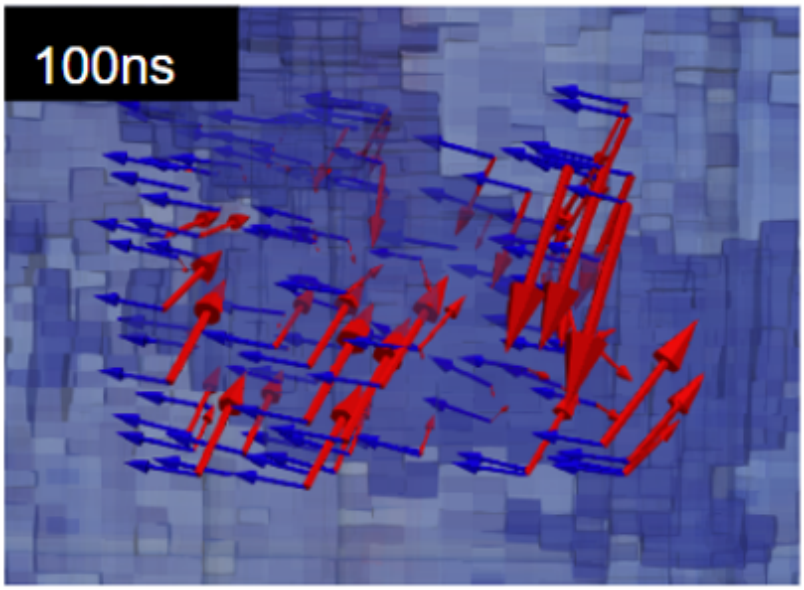

Figure 2.10: Plot of magnetic field vectors (blue) and electric field vectors (red) around the helical lobe plasma, which leads to $\mathbf{E} \times \mathbf{B}$ drift radially inward (into the liner/page) above the lobe and outward below the lobe. This is a contributing feature to instability roll-up. In this figure, $\hat{r}$ is into the page and $\hat{z}$ is the vertical axis.

component of $\mathbf{E} \times \mathbf{B}$ is plotted with red regions showing drift inwards and blue regions showing little to no radial drift. The inward drift is generally found on the top of the helical MRT lobes. This contributes to the roll-up feature by forcing the upper half of the MRT lobes radially inward, while the lower half is not affected by this drift creating a horizontal shear. While this effect is not as pronounced as the axial velocity shear it still acts as a contributing factor to the roll-up asymmetry of the MRTI.

In Figure 2.12, we plot the axial component of $\mathbf{E} \times \mathbf{B}$ on a cross-sectional slice of the plasma column at $\sim$150 ns. Here it is seen that there is a radial distribution of drift velocity, where the outer edges of the plasma column see a notably larger upward drift velocity. This is not unexpected given the velocities plotted in Figure 2.9. The outermost edge of the plasma column sees a drift velocity that can be up to an order of magnitude larger than the drift velocities more radially inward. This again

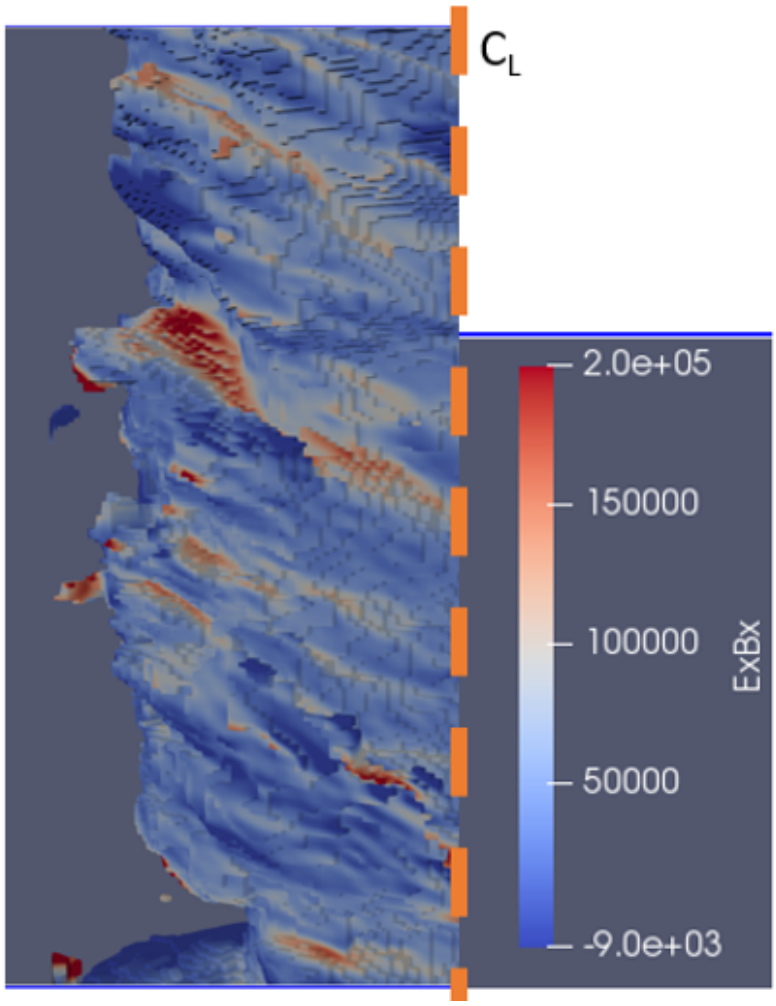

Figure 2.11: The radial component of $\mathbf{E} \times \mathbf{B}$. The darker red regions are directed radially inward more strongly. These regions are generally found on the top of the MRT instability lobes and contribute to the axially asymmetric roll-up features by creating a horizontal shear in $\mathbf{E} \times \mathbf{B}$ drift in addition to the axial velocity shear. Note that the $\hat{x}$ direction in this plot is the radial direction and the positive direction is to the right in this figure.

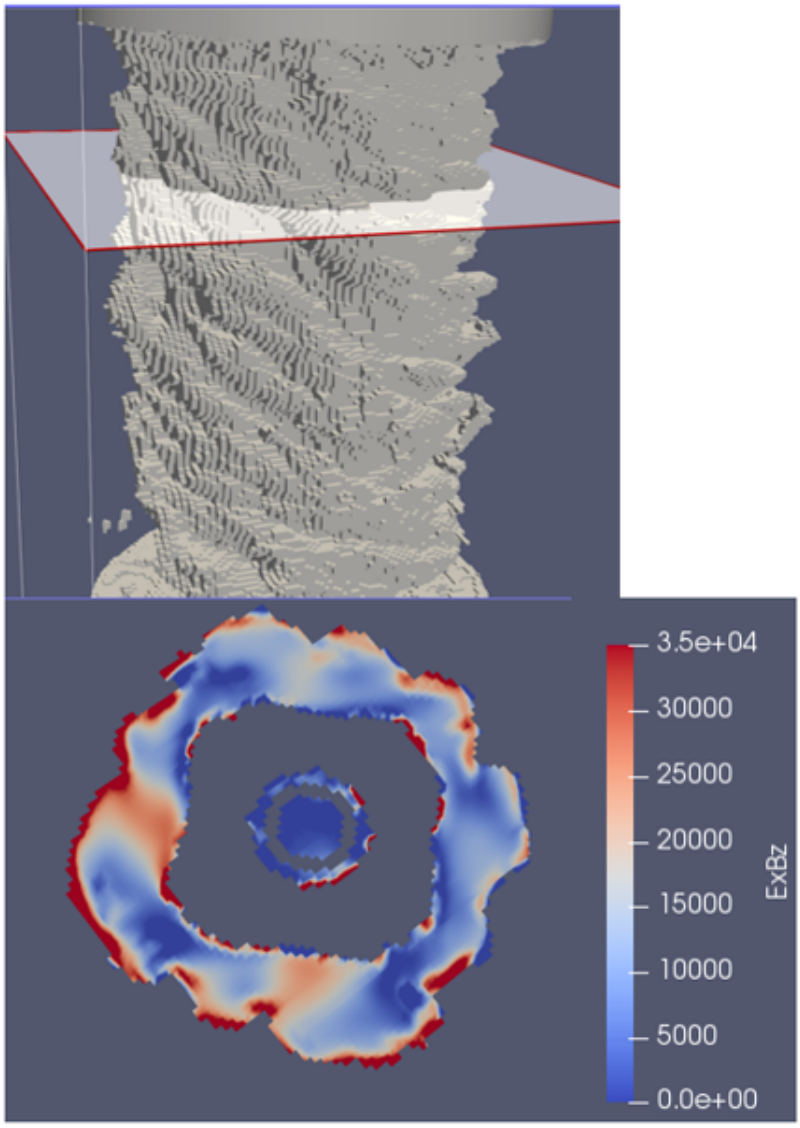

Figure 2.12: Axial component of $\mathbf{E} \times \mathbf{B}$ within a cross-sectional slice of the plasma column. This shows that at the edges of the plasma column, there is generally a significant increase in upwards $\mathbf{E} \times \mathbf{B}$ drift.

contributes to the axially asymmetric roll-up feature seen in z-pinches. For example, similar axial roll-up features have been observed along the outer edges of ablating wires in wire-array z-pinch experiments [49, 50]. Due to the electrons carrying most of the current, their motion also dictates the electric field geometry which includes a significant radial component directed inward. This combines with the magnetic field such that the $\mathbf{E} \times \mathbf{B}$ drift motion is as shown in Figures 2.11 and 2.12.

2.4 Support Rod Diameter Effects on Helical Mode Persistence

In past experiments where a z-pinch driven thin-foil liner implosion was pre-magnetized with a uniform externally applied B_z field, it had been observed that helical modes developed during the implosion phase and persisted into the explosion phase [21]. These experiments included an on-axis support rod (Figures 1.2 and 2.1). Initial modeling attempts for this dissertation work did not include this on-axis support rod, and the persistence of helical modes was not observed during stagnation or during the subsequent explosion phase. This led to the hypothesis that the persistence of the helical modes into the explosion phase was caused by the support rod limiting the convergence ratio of the implosion. This hypothesis was then tested by including a support rod in the simulations. The results show that, indeed, the helical structures remain intact into the explosion phase, after bouncing off the support rod. To find the radius where the support rod takes effect (i.e., to find the maximum convergence ratio where helical structures persist), four cases were simulated: an implosion with support rod radius of 0.50 mm, 0.25 mm, and 0.10 mm, as well as a case with no support rod. In each case, helical instabilities form during the implosion phase as expected. During the explosion phase, however, differences are observed. To compare each case, the plasma column at 10 ns post-stagnation is presented in Figure 2.13.

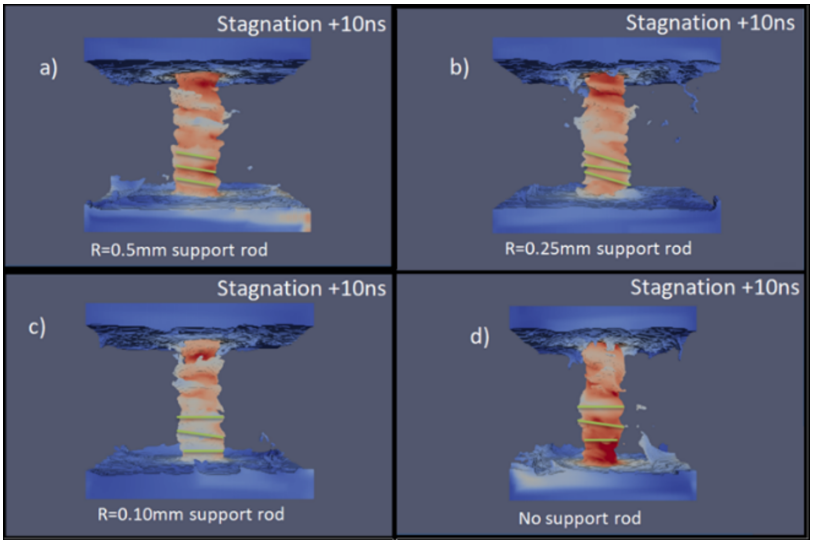

Figure 2.13: Comparison of thin-foil implosions for 4 different cases of on-axis support rod radii: (a) 0.5 mm; (b) 0.25 mm; (c) 0.1 mm; (d) 0 mm (no rod). The time chosen for this comparison is 10 ns after stagnation. The iso-density surface shown is 1×10^{19} cm^{-3}. The image in part (a) should be contrasted with Fig. 5 in Ref. [19]

For each case, an iso-density surface was chosen at 1×10^{19} cm^{-3} and then color contrasted so that the plasma structures on the liner could be more easily identified. The instability structures are then traced and highlighted in Figure 2.13 to more clearly show the differences in each of the four scenarios. Figure 2.13(a) shows that with a support rod of 0.5 mm, the helical structures are preserved past stagnation, which is consistent with the experimental results of Ref. [21]. Figure 2.13(d) shows that with no support rod, the helical structure is almost entirely lost. There appears to be little-to-no difference between Figure 2.13(c) and Figure 2.13(d), indicating that a support rod radius of 0.1 mm has little-to-no effect on preserving the helical structures post stagnation. Figure 2.13(a), (b), and (c) show that the helical structure is increasingly preserved as the support rod radius is increased.

Presented in Figure 2.14 is a more detailed time evolution comparison of the case with a support rod of radius of 0.5 mm [Figure 2.14(a)] and the case with no support rod [Figure 2.14(b)]. In each case, there are clear helical structures at peak current

(labeled as "+0 ns"), but as the liners reach stagnation and then expand outward, the helical structures are preserved in the explosion phase of the case with the support rod and not in the case with no support rod. For ease of comparison, the plots in Figure 2.14 are colored according to distance from the axis so that the differences in structure are more apparent post stagnation.

For the case with no support rod, a plasma column forms on axis from low-density "precursor" plasma being blown in ahead of the bulk of the imploding liner material. The morphology of the on-axis precursor plasma, prior to the arrival of the bulk of the imploding liner material, has been found to set the morphology of the final bulk stagnation column in wire-array z-pinch experiments [51] as well as in the thin-foil liner simulations presented in this dissertation [23]. A more detailed analysis of this behavior is presented in the next section. For now, we simply note that the addition of a massive on-axis support rod prevents this relatively low-density precursor plasma from morphing (due to instabilities) into a shape other than that of the much more massive on-axis support rod. Instead, the precursor plasma accumulates along the smooth surface of the support rod, creating a uniform cushion for the bulk of the liner material to implode onto. This cushion, along with the rod radius, dictates the maximum convergence ratio that the imploding liner will obtain.

The maximum convergence ratio achieved in each of the four cases is listed in Table 2.1. Because of the instability structure, it is difficult to determine the minimum radius achieved by the liner at stagnation. To determine a minimum radius and thus a convergence ratio, each of the four cases was analyzed at the point of stagnation as follows. Only plasma of density equal to or greater than the initial liner density of 6×10^{19} cm^{-3} was considered. This is plasma three orders of magnitude less than solid density. Plasma of density below this threshold was ignored. Next, the average radius of this plasma column was determined by measuring the radius of each instability peak and trough along one side of the plasma column. These values were then

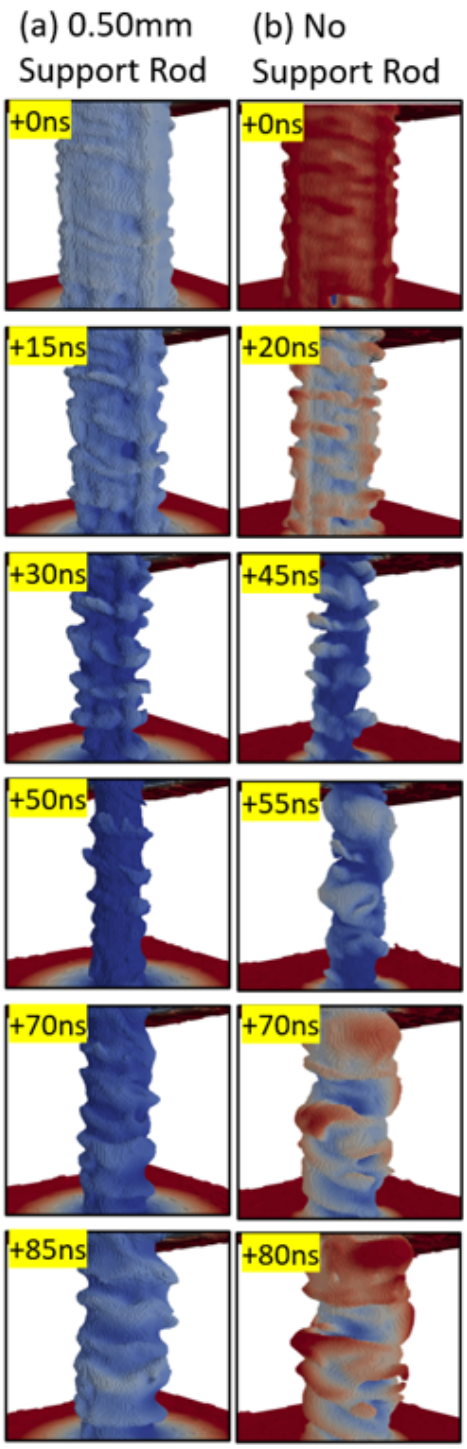

Figure 2.14: Time evolution comparison of thin-foil liner implosions for on-axis support rod radii of (a) 0.5 mm and (b) 0 mm (no rod). The time labels are relative to peak current. For ease of contrasting, the coloring is based on distance from the cylindrical axis and is tinted slightly red for the case with no support rod and slightly blue for the case with the support rod. The iso-density surface shown is 1×10^{19} cm^{-3}.

averaged to obtain an approximate average radius of the column. Referring to Table 2.1, the convergence ratio does not vary strongly with the radius of the support rod for support rod radii of 0.25 mm and smaller. Furthermore, the convergence ratio for the 0.5-mm case is notably smaller than the other three cases. The 0.5-mm case is also the case where helical instability structures were best preserved after stagnation.

Support Rod Radius (mm)	Average Radius at Stagnation (mm)	Convergence Ratio (Cr)
0.5	1.045	2.87
0.25	0.62	4.84
0.1	0.791	3.79
0	0.756	3.95

Table 2.1: Minimum radius and maximum convergence ratio obtained for each of the four support-rod cases simulated.

2.5 Precursor Plasma Column Morphology

Without a support rod, a precursor plasma column is able to form from plasma blown in ahead of the imploding liner bulk. This precursor plasma column sets up on axis early in time, before the bulk of the imploding liner material stagnates on top of it. In our PERSEUS simulations, the morphology of the precursor column determines the morphology of the final stagnation column. This is shown in Figure 2.15, where we highlight the formation of structures in this central plasma column that then develop into the dominant structures of the stagnating and exploding plasma bulk. In Figure 2.15, the formation of a well-defined plasma structure in the precursor and stagnation columns is highlighted by the white arrow. Similar behavior has been observed previously in wire-array z-pinch experiments (see Fig. 13(b) in Ref. [51]). Although precursor plasma columns are often observed in wire-array z-pinch experiments, they are more difficult to observe in liner implosion experiments.

This is because the imploding liner wall obscures a direct side-on view of the precursor plasma for most diagnostics (i.e., non-penetrating diagnostics). Nonetheless, precursor plasmas in metal liner experiments have been detected by inserting B-dot probes inside the imploding liner [15]. They can also be imaged using end-on diagnostics [52]. Though a detailed discussion of wire-array z-pinch physics is beyond the scope of this dissertation, we note that the physics of wire ablation and precursor plasma formation in wire-array z-pinches is a bit different from precursor plasma formation in thin-foil liner experiments. Nevertheless, the fact that PERSEUS appears to capture the physical connection between the morphology of the precursor plasma column and the morphology of the stagnation column, as has been observed in wire-array z-pinch experiments [51], is encouraging.

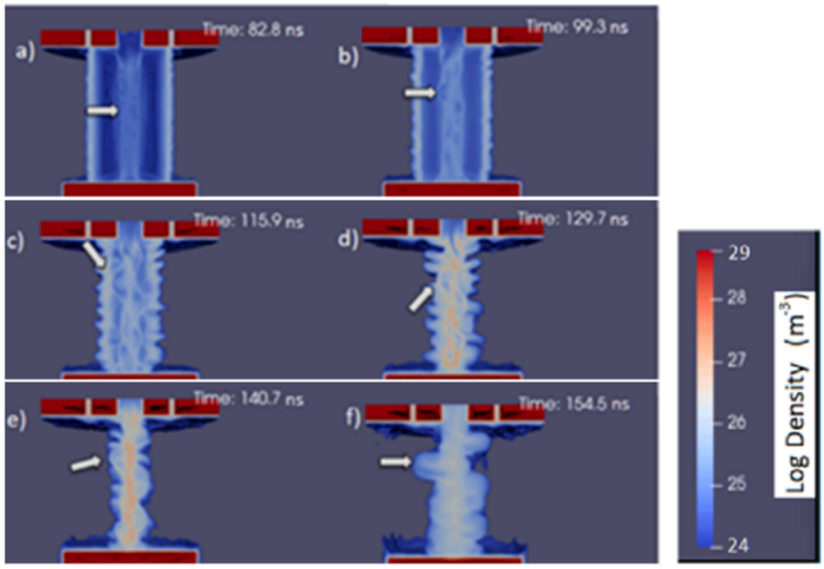

Figure 2.15: Simulation of a thin-foil liner implosion with no support rod on axis. The lack of a support rod allows a precursor plasma column to assemble on axis with various instability structures. A particularly well-defined structure is identified by the white arrow. This structure is tracked through stagnation and into the explosion phase. These six frames illustrate that the morphology of the low-density precursor plasma, which arrives on axis ahead of the imploding liner bulk, is largely responsible for setting the morphology of the imploding liner bulk during stagnation and explosion. This figure should be contrasted with Fig. 13(b) in Ref. [51]

CHAPTER III

Origin of Helical Instabilities in Axially Premagnetized Thin-Foil Liner Z-pinch Implosions using Hall Magnetohydrodynamics

As the previous chapter discussed, helical MRTI structures have been observed in z-pinch-driven liner implosion experiments with a pre-imposed axial magnetic field. In this chapter, it will be shown that the formation of these helical structures can be described by a Hall magnetohydrodynamics (HMHD) model. PERSEUS was used to study these helical instabilities, and the results show that a Hall Instability in the low-density coronal plasma immediately surrounding the dense liner is responsible for producing helically bunched plasma striations as well as an associated magnetic field and current density. This seeds the helical pitch angle of the MRTI even when other proposed helical seeding mechanisms are either not present in the experiments or not accounted for in the simulations. For example, this mechanism does not require low-density power-feed plasmas to be swept in from large radius or the development of electrothermal instabilities. The Hall Instability is thus a new, independent explanation for the origin of the helical instabilities observed in axially premagnetized liner experiments. Simulation results supporting this mechanism are presented.

3.1 Simulation Setup

The simulations presented in this section used a fifth order central finite-volume method with considerable accuracy improvements over the third order method used in the simulations in the previous section. As a result, the increased accuracy has allowed better analysis of the simulation data that has shown that helical instabilities can be produced through Hall physics alone and that initial helical seeding is unnecessary [20,23]. In Figure 3.1 the simulation setup is presented, which includes a plasma liner of uniform initial density and uniform initial temperature, with a low-density coronal plasma layer immediately surrounding the denser liner. The current pulse that drives the simulation is a sine-squared pulse with a rise time of 200 ns and a peak current of 600 kA.

The simulation setup was chosen to match the conditions of university-scale thin-foil experiments as much as possible. However, due to the computational challenges of properly resolving the ablation of a 400-nm-thick aluminum foil liner, the simulation is not allowed to fully evolve until times later than 25 ns into the current pulse, at which point the liner is expected to have already ablated into a 1-eV liner plasma of 250-μm thickness. During the times from 0 to 25 ns into the current pulse, the electromagnetic fields are allowed to evolve while the plasma is held motionless. These pre-ablated conditions come from the results of highly resolved HYDRA simulations conducted previously to study the early-time foil ablation process in detail [53]. These pre-ablated conditions are used as the initial conditions for the PERSEUS simulations presented herein. These pre-ablated initial conditions, as well as the effects of the on-axis plastic support rod (which is necessary to support the thin-foil liners in experiments), are discussed in further detail in Chapter II and Ref. [23].

Immediately surrounding the dense liner plasma is a low-density coronal plasma layer, initialized with a thickness of 1 mm, a temperature of 5 eV, and a density of 6×10^{14} cm^{-3}, which is 20$\times$ the density floor in PERSEUS. The version of PERSEUS

used in this work is capable of handling 9 orders of magnitude density variation. Between the coronal layer and the liner plasma are two single cell layers that step the density down from the liner plasma density to the coronal density to prevent artificial numerical effects from developing due to sharp density gradients. This coronal layer heats rapidly to a few hundred eV within ∼10 ns. The dynamics of this layer, including its ability to seed helical MRTI, is the subject of this Chapter.

Each PERSEUS simulation included over 7 million cells, with cell sizes of approximately $62.5 \times 62.5 \times 32$ μm^3, for a total simulation volume of $14 \times 14 \times 6.125$ mm^3. The simulations were run on 64 cores on the Great Lakes computing clusters at the University of Michigan. The simulated temporal extent was 250 ns with time steps on the order of one picosecond. Multiple conductivity models were used, including a Lee-More-Desjarlais resitivity model combined with a Spitzer model, a Spitzer model, a constant conductivity model, and a zero resistivity model. It should be expected, however, that there is non-negligible numerical resistivity that will allow some penetration of magnetic field into the liner even in the absence of an applied resistivity. It was found that the choice of conductivity model had negligible impact on the Hall instability effects discussed. Electrons velocities are limited through electron inertia; however, this was found to not have significant impact on the behavior of the Hall instability structures. This will be discussed further in a later section. In total, each simulation required upwards of 60 wall-clock hours to run. A random density perturbation of less than 1% was applied to the liner cells and to the corona cells to seed instability growth. A 2-T axial magnetic field was applied throughout the simulation volume initially (and maintained at the radial boundary for the duration of the simulation) to match previous university-scale axially premagnetized z-pinch experiments [21].

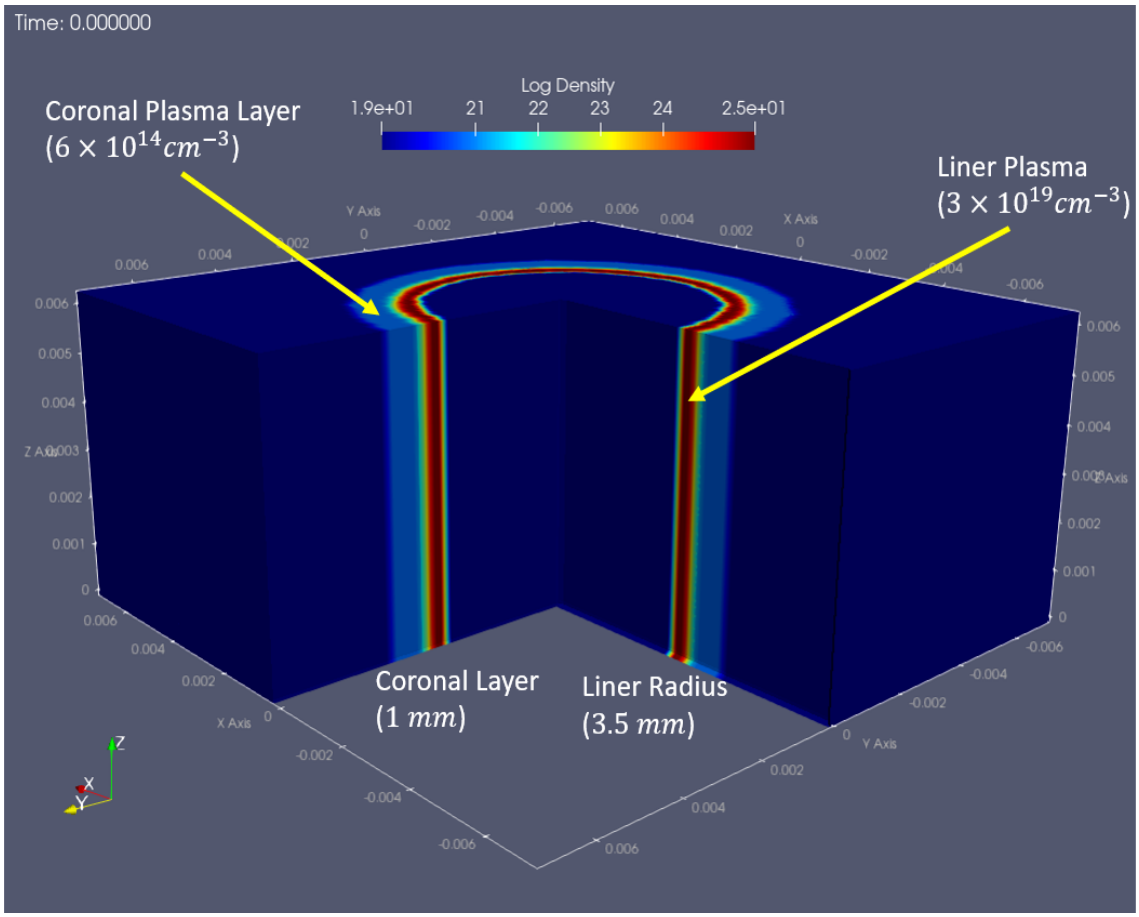

Figure 3.1: Initial conditions of the simulation setup that shows the coronal layer (6×10^{14} cm^{-3}) and the liner plasma (3×10^{19} cm^{-3}). In addition, two single cell layers between the liner plasma and coronal plasma are included that help to step the density down and reduce the sharp density gradient. Note a uniform 2-T axial magnetic field is applied throughout the simulation volume.

3.2 Hall Interchange Instability As a Seed for Helical MRTI

In an Ideal-MHD context, the interchange instability manifests as magnetic field and plasma trading position, also known as a flute instability driven by magnetic curvature. In the absence of magnetic curvature the Hall term can drive an interchange instability through electron drifts. With the Hall term, the interchange instability manifests itself in several ways. One of the major effects is that the current is advected into helical bunches and vortices are formed in the current. This is driven by magnetic energy release. The result is that helical striations in the azimuthal current are formed in the coronal plasma and are imprinted on the dense liner plasma that is surrounded by the coronal layer. In addition, the current is strongly force-free, meaning it is aligned with the magnetic field and it stays force-free well into the implosion (>185 ns). The magnetic field also maintains its helicity in large part because of the force-free current being helical as well. The result of the force-free current is that there is a significant amount of azimuthal current which leads to axial flux amplification. This adds more axial magnetic field helping to maintain the magnetic field helicity which also leads to seeding of helical MRTI. The axial magnetic field is amplified by a factor of $\sim 8\times$ over the course of the current pulse rise time. The force-free currents can be seen in Figure 3.2, at 185 ns into the current pulse, where the magnetic field lines are traced in blue, the current is traced in red, and the dense liner plasma is shown at an iso-density surface (10^{24} m^{-3}) with helical MRTI clearly formed.

As discussed, the interchange instability strongly influences the flow of currents in the coronal plasma. This leads to a helical perturbation in the current that is magnetic field aligned. This perturbation grows quickly and maintains its helical pitch as the magnetic field remains relatively helical due to flux amplification from the azimuthal component of the helical current. The perturbation in the azimuthal component of current density is shown in Figure 3.3.

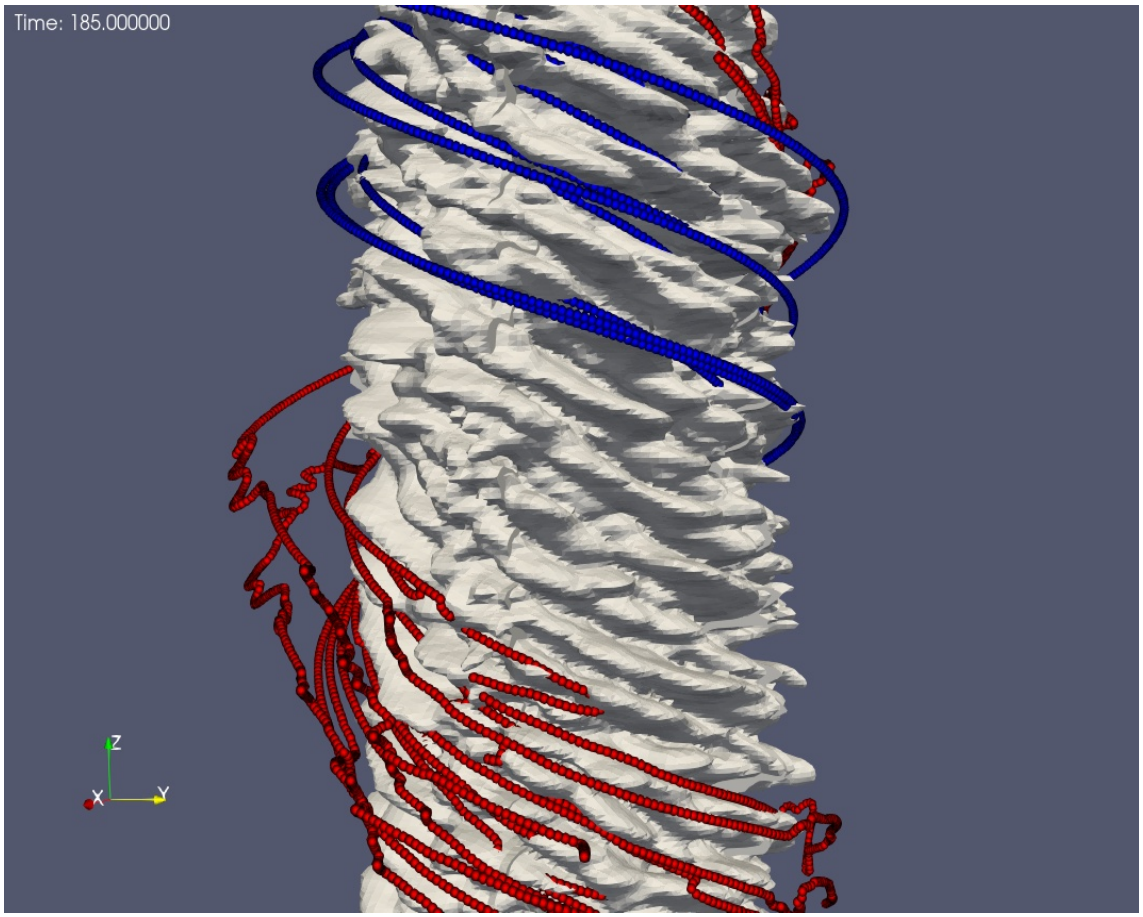

Figure 3.2: Helical MRTI forming in the dense liner plasma 185 ns into the current pulse. The iso-density surface shown is for 10^{24} m^{-3}. Magnetic field lines are traced in blue and current density streamlines are traced in red.

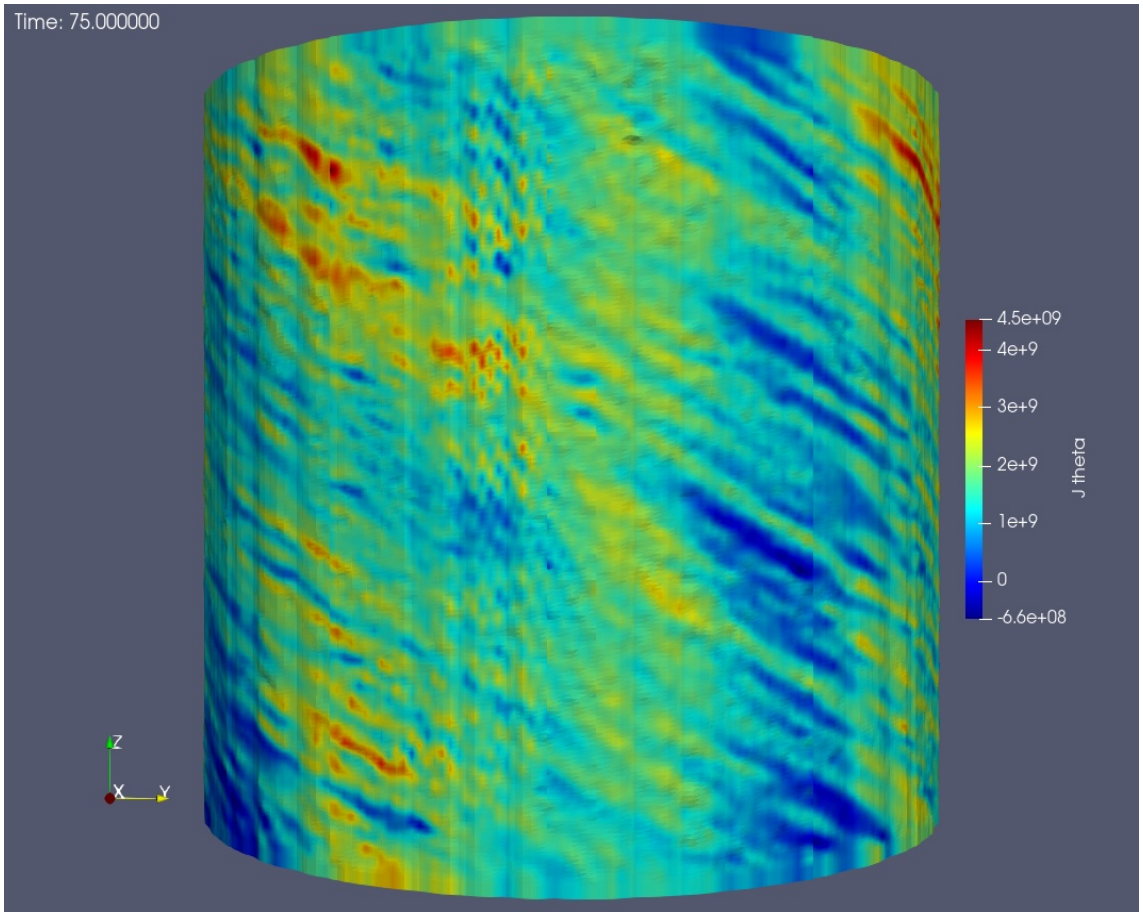

Figure 3.3: Helical perturbation in the azimuthal component of the current density, plotted on an iso-density surface (10^{24} m^{-3}) at 75 ns. This highlights one of the perturbation effects of the Hall interchange instability, which leads to helical formations in the current on the liner plasma outer surface.

To demonstrate how the perturbations in the current, within the coronal plasma layer, lead to seeding of the MRTI structures on the liner plasma, Figures 3.4 and 3.5 are shown, which consist of several slices of the full 3-D data at several time steps. In these figures, a transparent iso-density slice of the liner plasma (of density 10^{23} m^{-3}) is overlaid on top of plots of the azimuthal (Fig. 3.4) and radial (Fig. 3.5) components of the current density. This shows how the perturbations in the coronal layer embed into the liner plasma and work to seed the wavelength and mode number of the MRTI structures. In Figure 3.4, the perturbations in current in the coronal layer embed into the liner plasma, and at 170 ns, where the MRTI structures are outlined on the outer surface of the liner plasma, the current perturbations correlate directly with the MRT instability lobes. The Hall interchange instability drives these current perturbations early in the coronal plasma current and forms within the first 50 ns of the simulation.

A growth rate for the observed instability is determined by taking an axial line-out through the coronal plasma layer of the azimuthal current bunches and measuring the perturbation amplitude. The growth rate from this analysis is found to be 0.1 ns^{-1} +/- 0.02 ns^{-1}. From Eq. (1.36) in the theoretical analysis presented in Sec. 1.3.2, the expected growth rate is 0.12 ns^{-1} +/-0.05 ns^{-1}. The theoretical growth rate is highly dependent on initial magnetic field, coronal plasma density, and axial wave number. It should be noted that local analysis, which was used to determine the simulated growth rate, often over estimates instability growth rates. A plot of this growth rate is shown in Figure 3.6. The error bars are determined by one standard deviation in the instability amplitudes at each time step. In addition, the axial wave number is plotted below in Figure 3.7. The instability wave number is set almost immediately as the plasma is allowed to evolve at 25 ns as discussed above in Sec. 3.1. This wave number remains relatively constant while the Hall interchange instability is still the dominant instability effect. Note that in the growth rate analysis, there is a steep drop off at

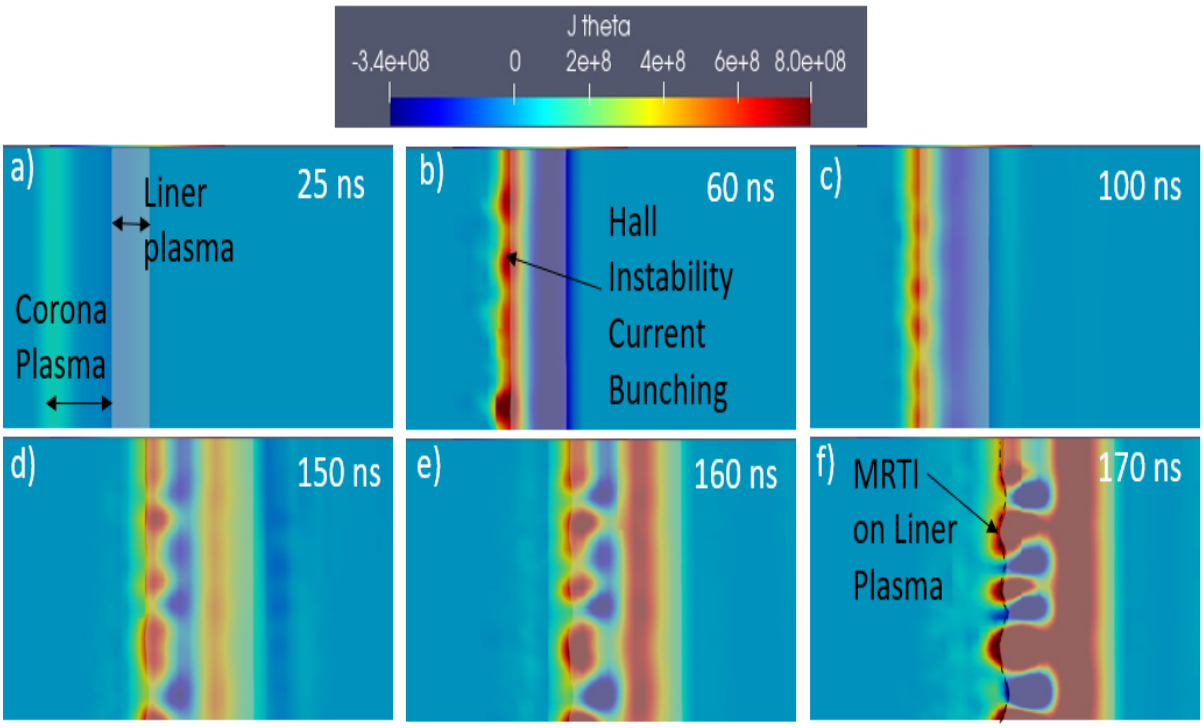

Figure 3.4: Perturbation in the azimuthal component of the current density, plotted with an iso-density surface slice of the liner plasma (10^{23} m^{-3}) at six time steps to show the process of the perturbations forming in the coronal layer and embedding into the dense liner plasma. The cylindrical axis of symmetry is the right edge of each image, while the outer simulation boundary is the left edge of the images.

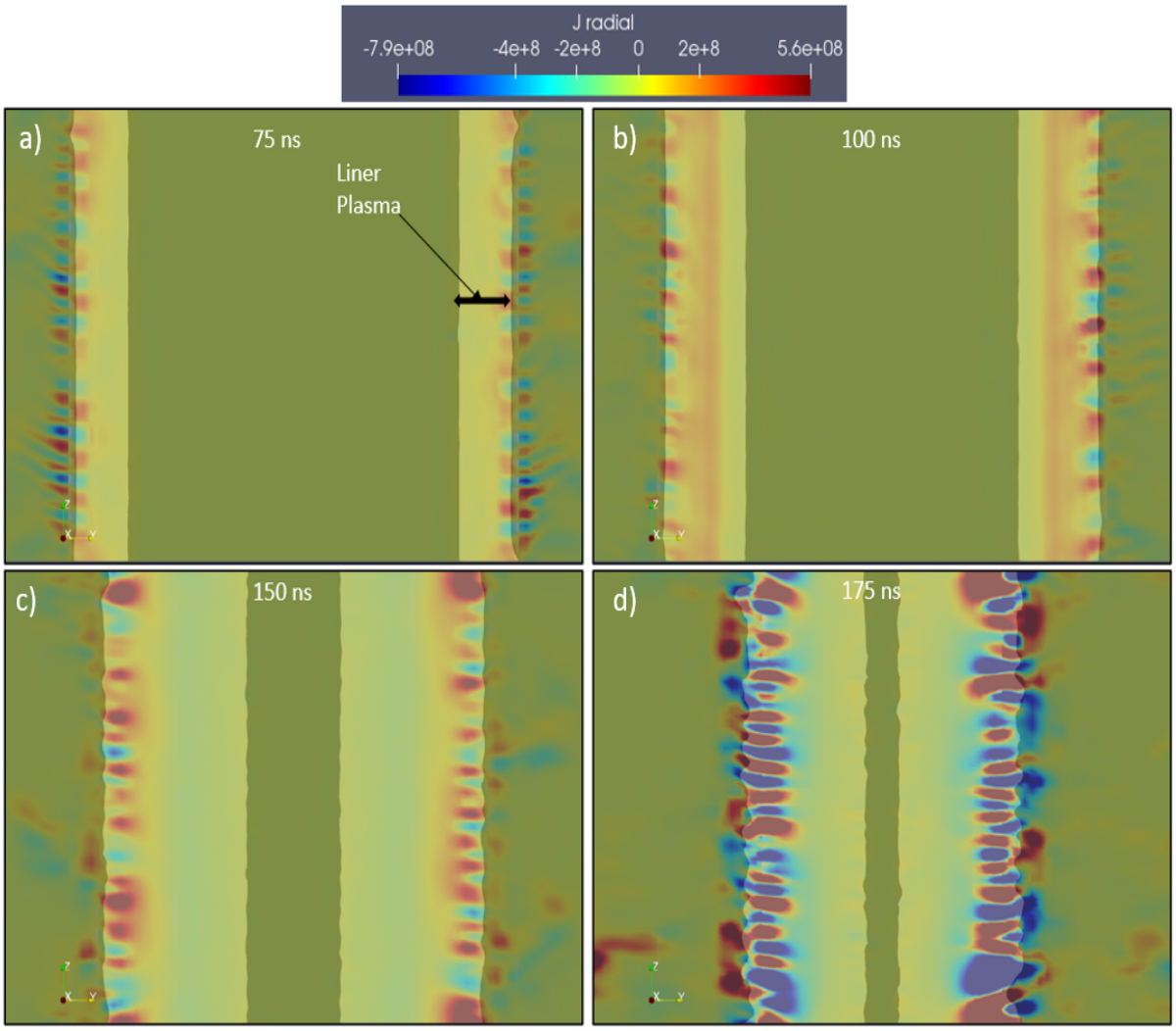

Figure 3.5: Perturbation in the radial component of current density, plotted on a 2-D slice from the simulation volume over top of which an iso-density surface transparency of the dense liner plasma (10^{23} m^{-3}) at four time steps to show the process of the perturbations forming in the coronal layer and extending into the liner plasma.

75 ns. This is likely due to other slower growing instabilities like MRTI becoming more dominant and disrupting the interchange instability. Note that for this growth rate analysis, the resistivity in the simulation was set to zero throughout. This was done due to the fact that the theoretical analysis and theoretical growth rate were determined assuming zero resistivity. It was found that changing the conductivity model from a coupled Lee-More-Desjarlais and Spitzer model to a constant value of zero had little effect on the Hall instability dynamics. Electron inertia terms were included in some simulations to provide a limiting mechanism for electron velocities, but it was found that the inertia terms had no discernible effect on the Hall instability dynamics compared to a limiting method using a static limiter term. In either case, the electron velocities never exceeded the speed of light.

3.3 Boundary Conditions Effects

An important factor that determines the dynamics of the coronal layer, and therefore the dynamics of the liner implosion, is the choice of boundary condition on the upper and lower z boundaries. We consider two boundary conditions in this work, namely periodic and open boundaries.

Periodic boundary conditions have the effect of leading to reduced Hall instability effects as compared to an open boundary condition. This is due in part to this boundary condition leading to the compression of the coronal layer onto the outer liner plasma surface faster than what is seen in an open boundary simulation. This is in large part due to periodic boundary conditions on the lower and upper z boundaries not allowing azimuthal flux to leave through the boundary. This prevents several effects that would lead to axial flux amplification, which in turn leads to the coronal layer being compressed by $\mathbf{J} \times \mathbf{B}$ forces within the first 50 ns of the simulation. The consequence is that Hall effects are not able to establish in the coronal layer before its compression and therefore do not have the requisite time to seed helical MRTI in

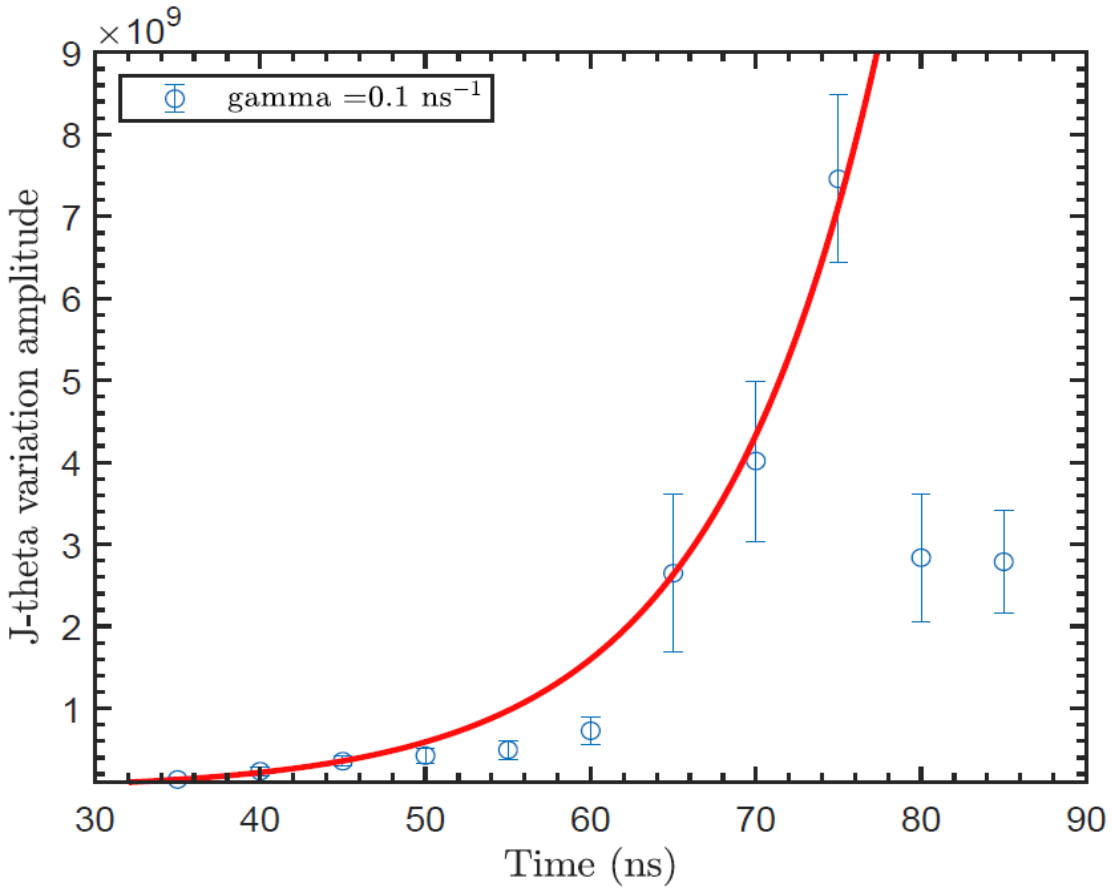

Figure 3.6: Plot of the azimuthal perturbation amplitude growth rate. The amplitude was taken by an axial line-out through the coronal plasma subject to the Hall interchange instability. The growth rate found from this analysis compares very closely to the growth rate predicted by theory. The error bars are determined from one standard deviation in the perturbation amplitude.

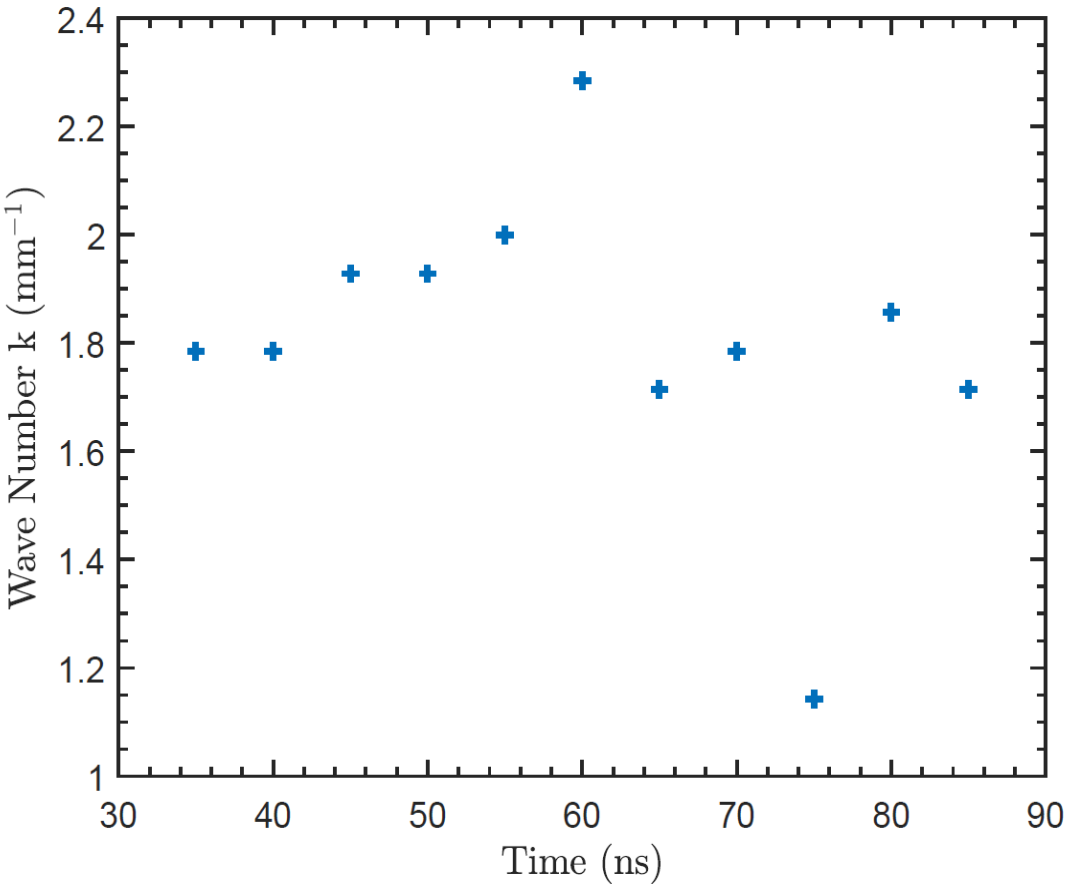

Figure 3.7: Plot of the axial wave number of the perturbation in the azimuthal current. The wave number is set within a few nanoseconds of the simulation and remains fairly constant throughout the period when the interchange instability is still the most important instability ($\lesssim$80 ns).

the liner plasma.

When an open boundary condition is implemented on the axial boundaries, azimuthal flux (and therefore EM energy) is able to leave the simulation domain by outflow which allows for the amplification of axial magnetic flux. This effect was studied in 2-D by Seyler in the context of gas-puff z-pinches [54]. In those gas-puff simulations, it was found that the choice of boundary condition was imperative to producing an increase in B_z due to an axial loss of B_θ flux due to use of a Poynting outflow boundary condition. The driving factor of this effect is the conductivity tensor described in Sec. 1.2.2, which is an effect of including the Hall term. The parallel term (with respect to the magnetic field) in the conductivity tensor is the most conducting and therefore it leads to currents flowing along magnetic field lines. For strongly magnetized electrons, the total current, which is generally force free, is approximately:

$$\mathbf{J} = \mathbf{B}\frac{B_z E_z}{B^2 \eta}. \tag{3.1}$$

More generally this current is $\mathbf{J} = \hat{b}\hat{b} \cdot \mathbf{E}/\eta$, where $\hat{b}$ is the unit vector in the direction of the magnetic field. If this current exists in a small sheath region then outside this current sheath there will be only azimuthal field and inside this sheath will be only axial field. This is indeed what was observed in Ref. [54]. A consequence of the loss of azimuthal flux and increase in axial flux was a reduction in the implosion of the gas puff due to the increase in axial magnetic pressure. This effect was only seen when the Hall term was included in the generalized Ohm's Law (GOL). The hallmark of this effect was the establishment of a long-lived shell of current in the low density plasma surrounding the gas-puff at large radii. For the 3-D thin-foil simulations presented here, a similar current effect is observed early in the simulation. This current effect is shown in Figure 3.8, where the azimuthal current component is plotted on a 2-D slice

of the 3-D data at 50 ns. One difference between the 3-D thin-foil liner simulations presented here in this dissertation and the 2-D gas puff simulations presented in Ref. [54] is that the current filament does not have the same stability. In Figure 3.8, at the top of the simulation, the filament is already being dispersed at 50 ns. It is not observed in the thin-foil simulation beyond ∼80 ns. This difference is due to the use of a Poynting outflow boundary condition used in the gas-puff simulations of Ref. [54] which leads to more outflow of the azimuthal flux as compared with the outflow boundary conditions used here. Whereas the thin-foil simulations shown here implemented an outflow axial boundary condition. The correct axial boundary condition for the thin-foil z-pinch liner is difficult to know and would require careful experimental work to determine and we must leave it to future work.

3.4 Comparison of Hall-MHD and MHD

One of the abilities of PERSEUS is that it is easy to switch Hall physics on and off. This allows for direct comparisons of simulations of the coronal layer with and without Hall physics included. This section presents a series of comparisons to demonstrate that Hall physics is necessary to see the effects discussed in this dissertation.

First, in Figures 3.9–3.12, a series of comparison images of the azimuthal component of current at 75 ns and 100 ns is presented. These four images are 2-D slices from full 3-D simulations and show that when Hall physics is included, the characteristic perturbations in azimuthal current are present, and when Hall physics is omitted, these perturbations are not present. Figures 3.9 and 3.10 show a side-on view of the azimuthal current density in the coronal layer at 75 ns. The liner plasma is represented as a transparent grey iso-density slice (10^{24} m^{-3}) similar to Figures 3.4 and 3.5. At this time step, the liner plasma has not begun to implode. In the MHD case (Fig. 3.9), the azimuthal current lacks the regular bunching that is the result of the Hall instability. By contrast, this regular bunching is seen in the simulations that

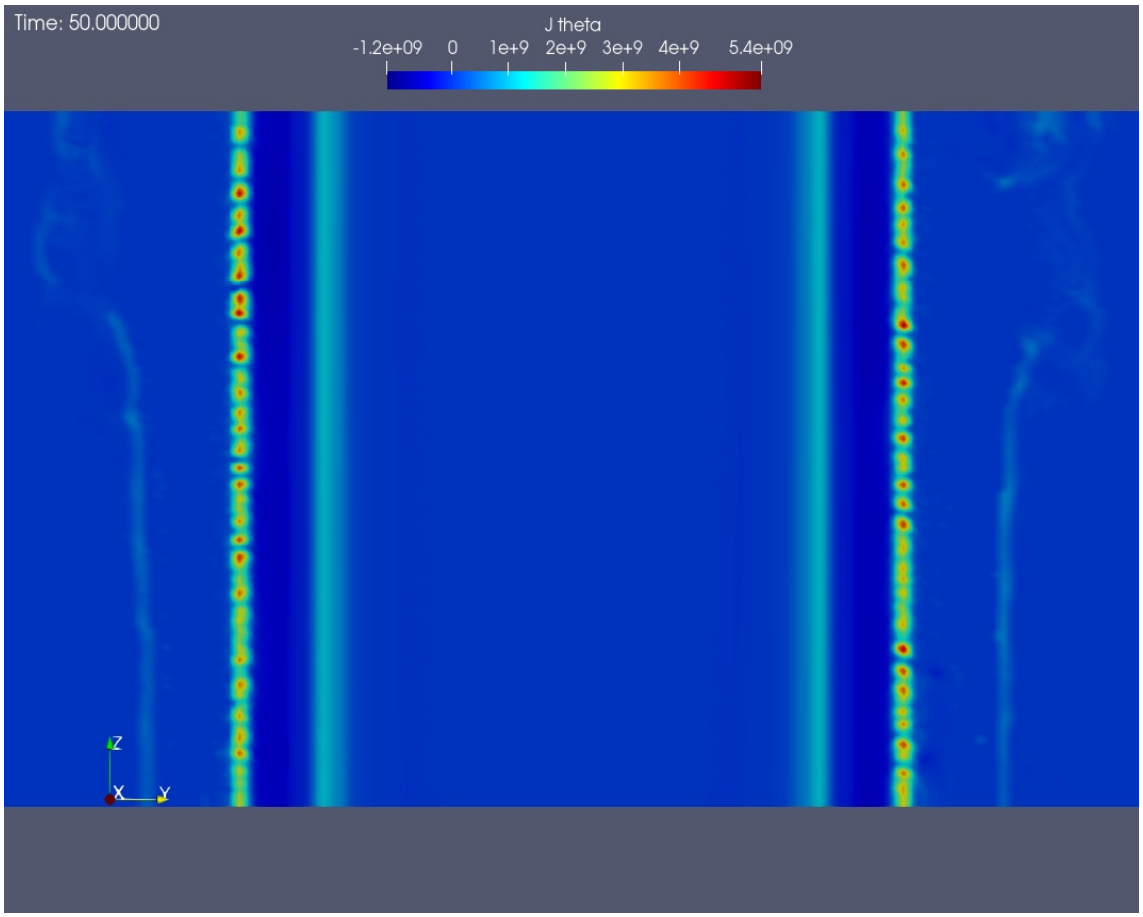

Figure 3.8: Plot of a 2-D slice of J_θ from a 3-D simulation of a thin-foil z-pinch with open outflow boundary conditions on the upper and lower z boundaries at 50 ns. The Hall instability bunching of J_θ in the coronal layer is evident as well as the filament of J_θ discussed in Seyler's gas-puff simulations [54].

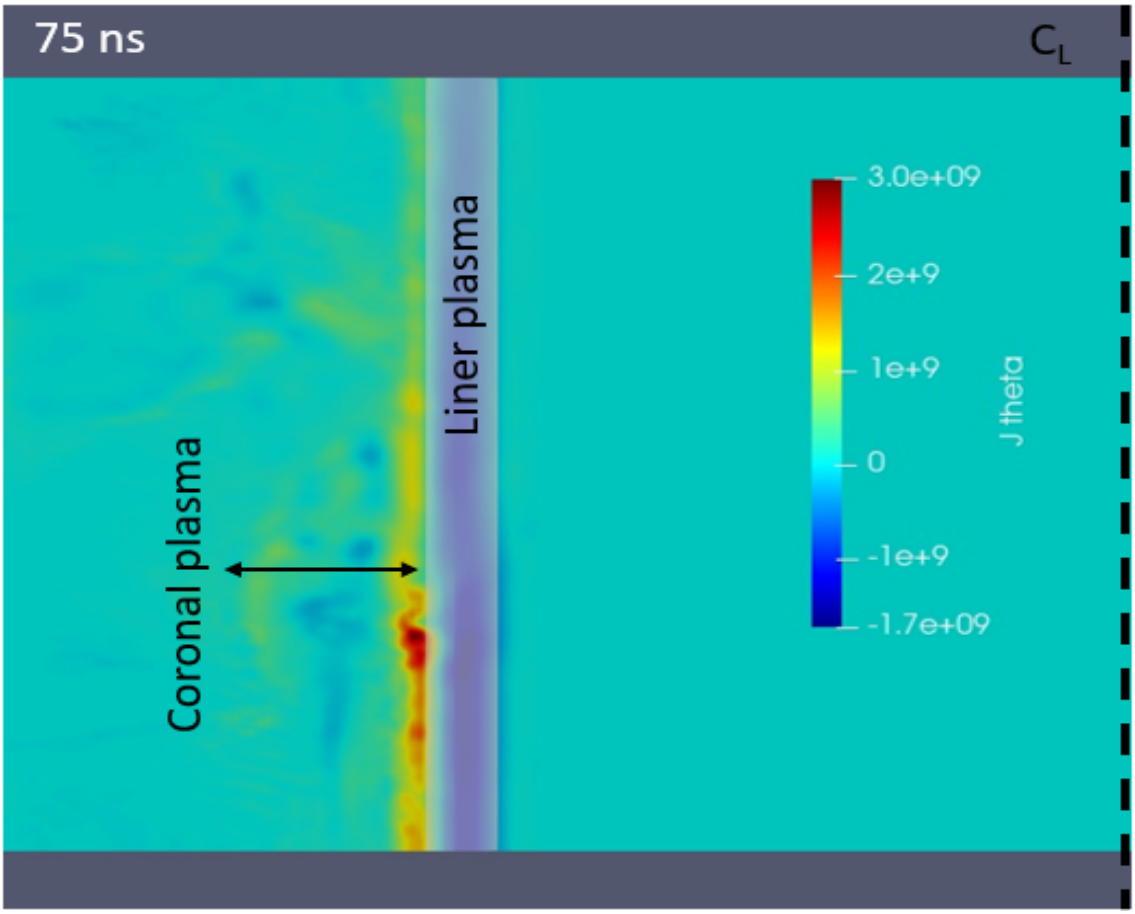

Figure 3.9: Plot of the azimuthal current density from a 2-D slice of the full 3-D simulation at 75 ns with Hall physics omitted. This image also has a partially transparent grey iso-density slice (10^{24} m^{-3}) to show the liner plasma. In this image, the lack of Hall physics prevents the Hall instability dynamics, in the azimuthal current, to take place and from the current bunching which has been discussed throughout this dissertation. The cylindrical axis of symmetry (centerline) is the rightmost edge of the image.

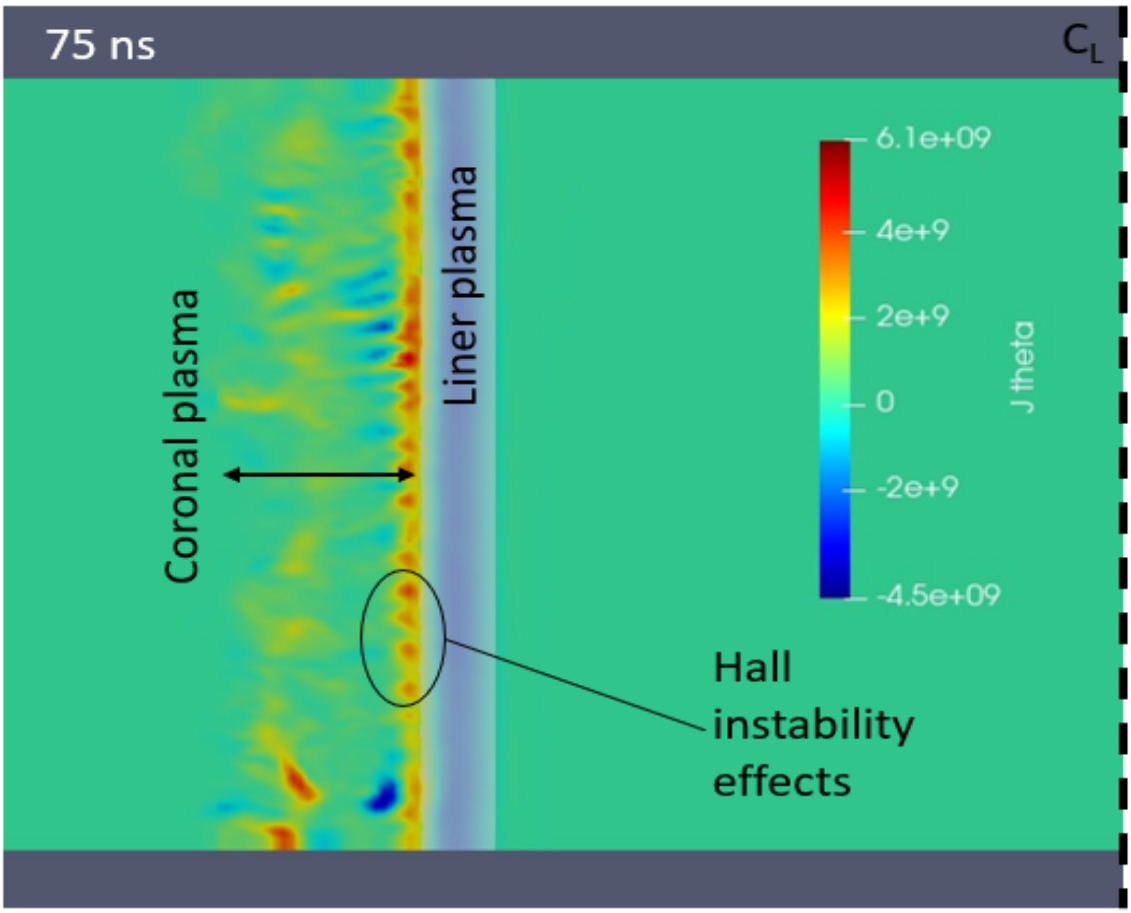

Figure 3.10: Plot of the azimuthal current density from a 2-D slice of the full 3-D simulation at 75 ns with Hall physics included. This image also has a partially transparent grey iso-density slice (10^{24} m^{-3}) to show the liner plasma.

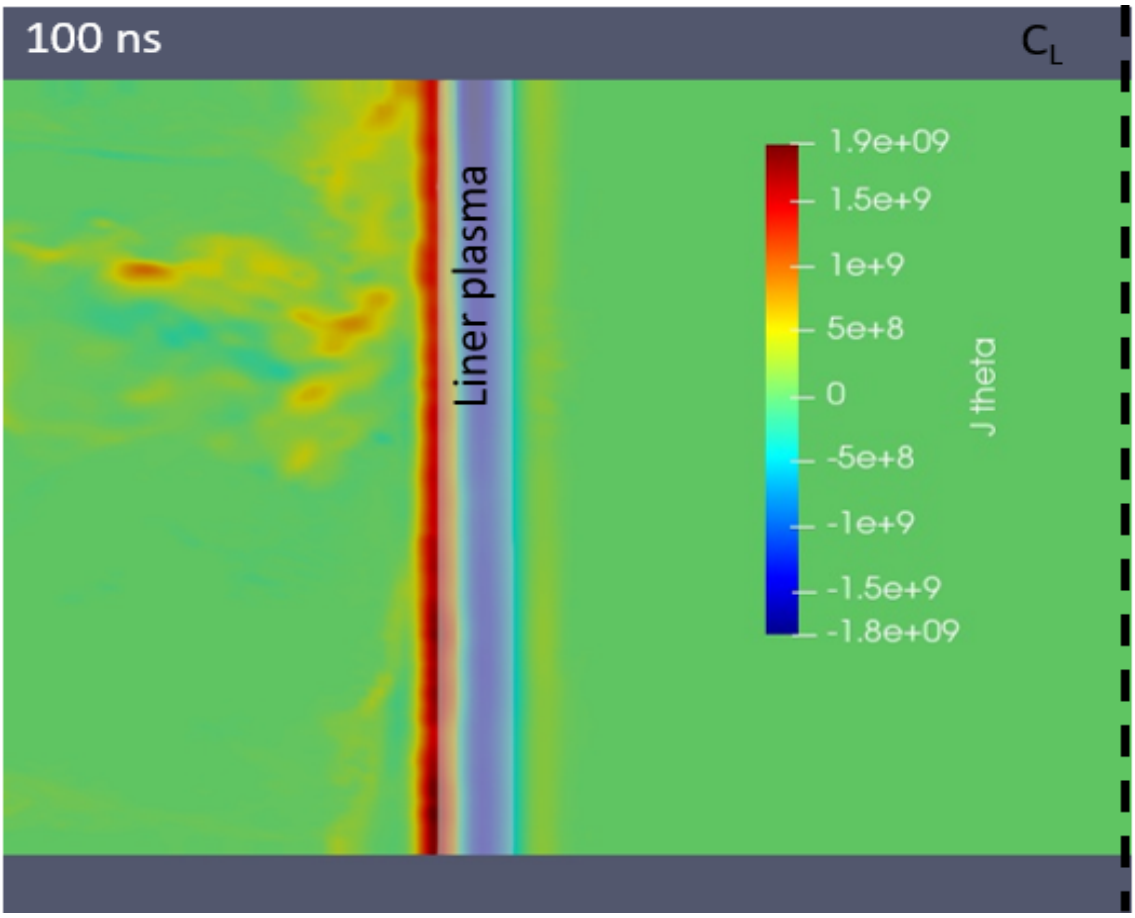

Figure 3.11: Plot of the azimuthal current from a 2-D slice of the full 3-D simulation at 100 ns with Hall physics omitted. This image again has a partially transparent grey iso-density slice (10^{24} m^{-3}) to show the liner plasma. In this later time step (relative to Fig. 3.9), the azimuthal current has compressed against the outer surface of the liner plasma and shows no perturbation structures.

include the Hall term in the generalized Ohm's law (see Fig. 3.10).

Without the Hall term to drive this instability, the azimuthal current has random bunching in the coronal layer, but lacks the regular pattern seen when Hall physics is included. Figures 3.10 and 3.12 show the regular pattern that is due to the interchange instability, while Figures 3.9 and 3.11 lack this. To show how this affects the current on the surface of the liner plasma, two images of iso-density surfaces of 10^{24} m^{-3} are plotted at 100 ns with the azimuthal current displayed. In the MHD case (Figure

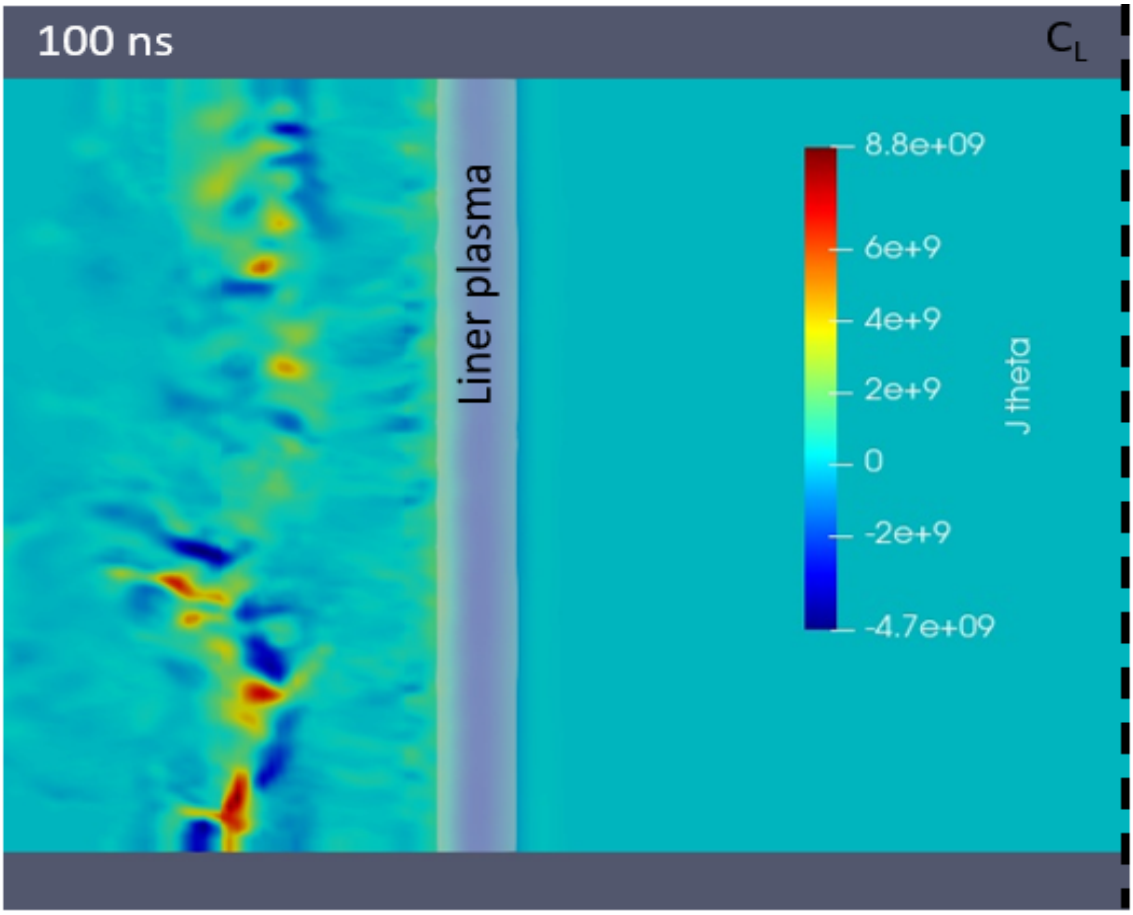

Figure 3.12: Plot of the azimuthal current from a 2-D slice of the full 3-D simulation at 100 ns with Hall physics included. This image again has a partially transparent grey iso-density slice (10^{24} m^{-3}) to show the liner plasma. In this later time step with Hall physics (relative to Fig. 3.10), the azimuthal current in the coronal layer continues to display the bunching and vortices that are the result of the Hall instability.

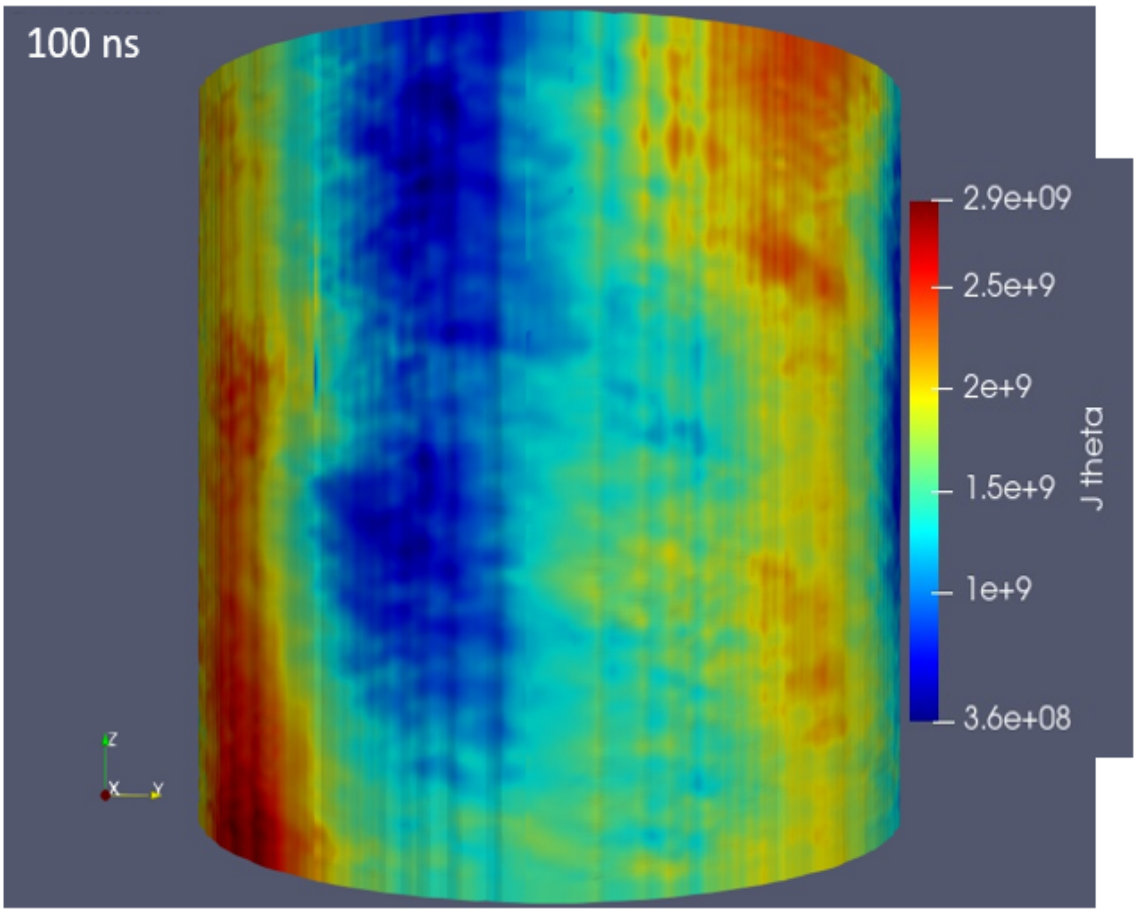

Figure 3.13: Plot of the azimuthal current density at 100 ns with Hall physics omitted. This image is of a full 3-D iso-density surface (10^{24} m^{-3}) to show the liner plasma's outer surface. In this plot, the azimuthal current does not show a predominant, consistent pattern.

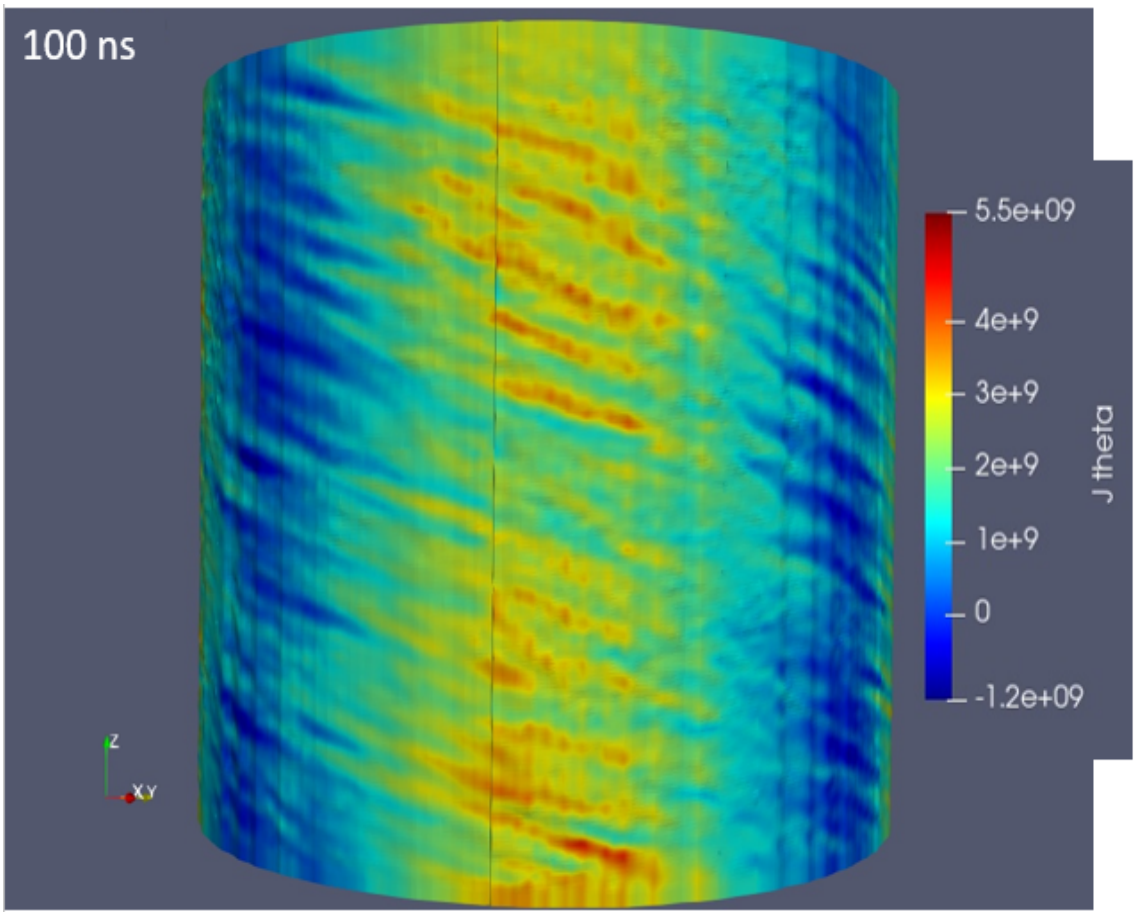

Figure 3.14: Plot of the azimuthal current density at 100 ns with Hall physics included. This image is of a full 3-D iso-density slice (10^{24} m^{-3}) to show the liner plasma's outer surface. In this plot, the azimuthal current shows a regular helical pattern.

3.13), there is no pattern to the azimuthal current, while in the case with Hall physics (Figure 3.14), there is a clear regular helical pattern on the liner's outer-surface. When Hall physics is included, the Hall instability in the coronal layer leads to this helical pattern on the liner's outer surface, which can then provide a seed for the helical MRTI discussed throughout this dissertation.

Another important aspect to the interchange instability (driven by the Hall term) is its adherence to a helical force-free configuration of the current and magnetic field. To demonstrate this, Figures 3.15 and 3.16 are presented, with magnetic field and current density streamlines traced around the liner at a time of 100 ns into the current pulse. In the case with the Hall term included (Figure 3.15), the current has a helical orientation that is well aligned with the magnetic field, and thus the plasma is in a force-free state. In the case without the Hall term (Figure 3.16), the magnetic field and the current have a much more azimuthal orientation. As discussed, when Hall physics is included, current vortices are produced and can be seen in the current traces of Figure 3.15, which shows a switch-back like feature. This feature is not seen in the current traces of the simulation without Hall physics (Figure 3.16).

Due to the lack of Hall instability effects in the MHD case, helical MRTI structures are not observed. The MRT instability is azimuthally correlated, as is the magnetic field after $\sim$160 ns. When Hall physics is included, the MRTI structures are very helical, as seen in Figure 3.2.

3.5 Discussion

As discussed in Sec. 1.3.2, the Hall interchange instability is not dependent on the resistive term in the GOL. This means that the conductivity model is relatively unimportant to the development of the instability perturbations observed in the current components in the coronal plasma layer. This has been confirmed this by using several different conductivity models. These efforts found no qualitative differences

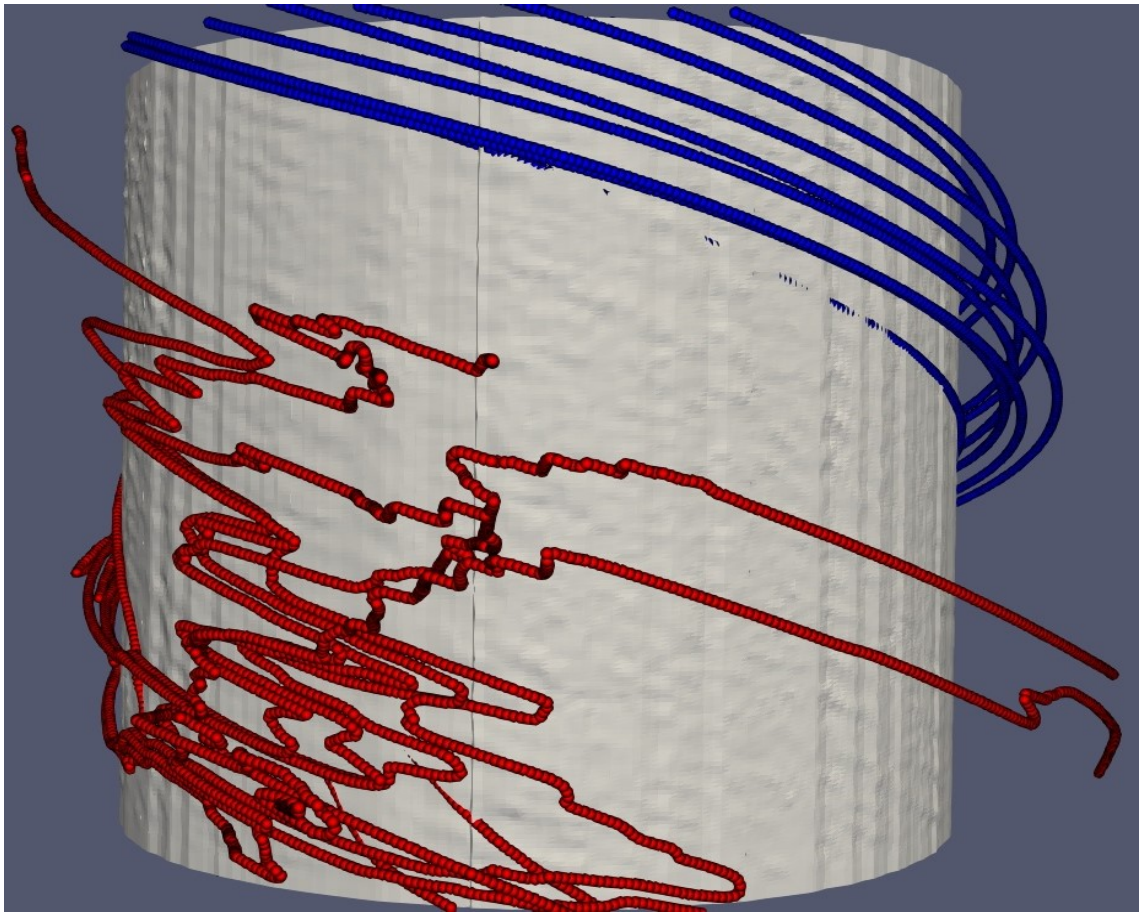

Figure 3.15: Plot from a simulation including Hall MHD of the liner plasma at an iso-density surface of 10^{23} m^{-3} with magnetic field traced in blue and current density traced in red at 100 ns. The current is helical and generally force-free due to effects from the Hall term. Note also that the current traces have a switch-back like feature which is due to the current vortices created by the Hall instability.

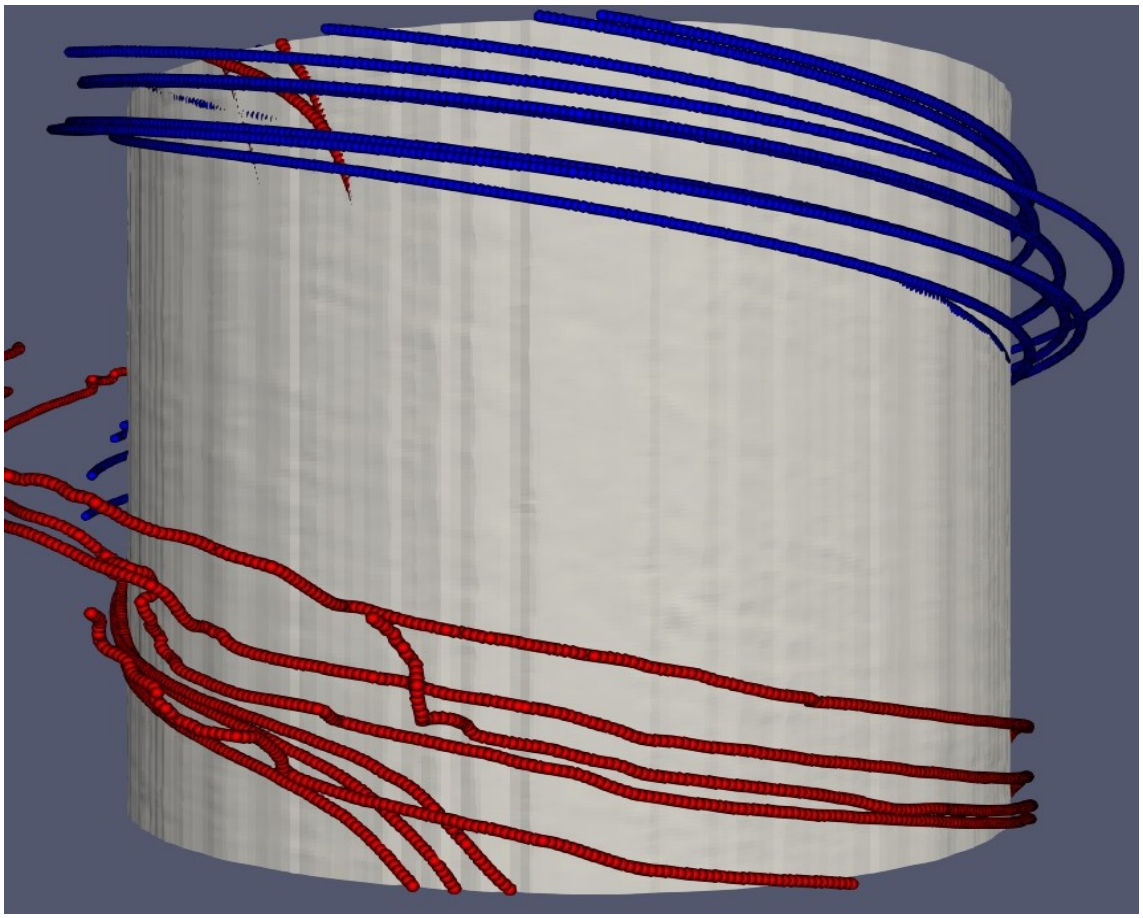

Figure 3.16: Plot from an MHD simulation that does not include Hall physics of the liner plasma at an iso-density surface of 10^{23} m^{-3} with magnetic field traced in blue and current density traced in red at 100 ns. The current does show some force free behavior at this time step, but note that the magnetic field is less helical compared with the HMHD simulation at the same time step. Also, the current traces lack the switch-back feature because the Hall instability is not present.

in the Hall instability effects.

Additionally, the electron inertia terms are similarly unimportant for the development and dynamics of the Hall instability. This was determined by running PERSEUS simulations with electron velocities limited by either an artificial limiting term, or by the inclusion of the electron inertia terms. The effects in both cases were the same. That said, it is important to limit the electron velocities so that they do not exceed the speed of light; otherwise, nonphysical instability structures and effects takeover.

PERSEUS simulations were run in which the coronal layer was non-existent or was compressed against the liner within the first few time steps. In these simulations, the Hall instability effects were not present as there was no coronal plasma layer. As a result, the liner plasma did not produce helical MRTI as it imploded; instead, the MRTI structures were azimuthal. Simulations were also run where the starting density of the coronal layer was increased by a factor of 10, and the Hall effects were not seen. This is due to the fact that the Hall term in the GOL has an inverse relation to density, thus it has its strongest effect (relative to resistive effects) in low-density plasmas. To observe the effects described in this dissertation, it is necessary to achieve as low of a density floor as possible. PERSEUS's capabilities in modeling 9–10 orders of magnitude in density allows it to achieve a low enough density floor for the Hall effects to occur within the coronal plasma layer. A key aspect that determines the preservation of the coronal layer is the choice of fast wave speed within the flux routine of the code. In the version of PERSEUS used in this study, a flux solver is implemented as described by Batten et. al., [55] where the fast wave speed was set to be the Alfvén speed plus the ion sound speed. If this value was set to be just the ion sound speed, the coronal layer was not preserved. The choice of fast wave speed determines if the outer surface of the liner plasma has a pseudo-ablation effect that allows the coronal layer to persist around the liner plasma. This phenomenon is not exactly physical in the code, but it captures the effects of the coronal plasma which is

known to occur in experiment [32]. Modeling the true physical mechanisms involved with the coronal plasma formation is beyond the capabilities of PERSEUS and may require kinetic modeling. That said, the Hall effects that then occur in the coronal plasma layer are well within the scope of PERSEUS' capabilities.

In future simulations and experiments, it will be important to understand how the coronal layer is formed and maintained. Along with this, electro-thermal instability effects are beyond the current capabilities of PERSEUS, as it is extremely difficult to properly resolve the phase transitions of the aluminum thin-foil from solid metal to low-density plasma. Doing so will require more robust conductivity models and/or kinetic models.

CHAPTER IV

Discussion and Summary

For many years, magnetohydrodynamics codes have relied solely on the resistive term in the generalized Ohm's law for simulation z-pinch plasma dynamics. The Hall term was largely ignored as it was difficult to implement and it was believed that the plasmas of interest in a z-pinch setting were outside the low-density Hall regime. The work presented in this dissertation shows that the Hall term is incredibly important to fully capture the complete dynamics of z-pinch plasmas, especially thin-foil liner z-pinches. PERSEUS is a code that is fairly unique at the moment in its capacity to simulate z-pinch plasmas in full 3-D with the inclusion of Hall physics. This is key for exploring and studying the effects described in the work presented in this dissertation. The importance of Hall physics is highlighted by the recent trend within the high energy density physics community to develop new codes that include Hall physics and retro-fit older resistive MHD codes with new routines to include Hall physics.

The value of including the the Hall term is shown in the results presented within this dissertation. As was discussed, incorporating the Hall term in the generalized Ohm's law is necessary to produce the helical MRTI structures in thin-foil liner plasma z-pinches. Although several explanations for seeding mechanisms have been proposed for thick-walled liner z-pinches such as the MagLIF concept at Sandia National

Laboratories, many of these considerations are not applicable to the university-scale thin-foil liners that were studied for this dissertation. For example, it has been proposed [4, 20] that the helical MRTI observed in MagLIF implosions on Z is the result of low-density plasma being produced in the anode-cathode gaps of the 20-MA Z-machine. Prior to the implosion of the liner, this low-density plasma in the anode-cathode gap implodes onto the liner's outer surface. Embedded in this low-density plasma is the pre-imposed B_z field. Thus, the B_z flux is compressed up against the liner's outer surface, thereby amplifying B_z and increasing the ratio of B_z/B_θ at the liner's outer surface. However, recent university experiments have found that very little plasma is produced in the anode-cathode gaps of smaller, 1-MA machines without doing something very deliberate to produce the plasma [30]. Yet, thin-foil liner z-pinch implosions on MAIZE still develop helical instabilities [21]. Thus, another mechanism must be responsible for the helical MRTI, at least for thin-foil liner implosions on smaller, 1-MA machines.

A second seeding mechanism that is thought to play a significant role in the seeding of helical MRTI in MagLIF implosions on Z is the electro-thermal instability (ETI). However, this instability seeding mechanism is not accounted for in the PERSEUS simulations presented herein, because PERSEUS lacks the requisite material and conductivity models. Thus, in these PERSEUS simulations, it is the Hall instability and Hall effects which produce the helical MRTI structures observed.

In addition to exploring the origin of the helical MRTI structures, PERSEUS was used to explore the late time instability dynamics that occur as the imploding liner plasma stagnates on a central support rod. It was found that the presence of the support rod was responsible for helical MRTI structures maintaining their integrity throughout stagnation and into the explosion phase, thus explaining the experimental observations presented in Ref. [21]. It was also found that without the presence of the support rod an on-axis plasma column forms and dictates the morphology of the

stagnation column. Similar behavior has been observed in wire-array z-pinches [51]. In the thin-foil liner simulations, it was found that this precursor plasma column carries approximately $\sim 1\%$ of the total drive current and is unstable to kink-mode instabilities.

CHAPTER V

Future Work

This dissertation demonstrates the importance of Hall physics in fast z-pinch implosions. There are several directions for future work that would continue to explore the effects studied here. First, it will be necessary to study the Hall physics effects in full-scale MagLIF on the Z facility. Going from a 1-MA university scale thin-foil liner to a thick liner designed for fusion experiments at >20 MA will be necessary to understand the impact of Hall physics on this important experimental platform. While Hall physics has been shown to provide an independent seeding mechanism for helical MRTI on thin-foil liners, it is likely that in a thick-walled liner implosion on Z, Hall physics will play a role in conjunction with other effects (e.g., ETI and flux compression in the power feed) to seed helical MRTI.

One important aspect where Hall physics may play a role at larger 20-MA scale machines is in the power feed region. As was discussed previously, on a 1-MA pulsed power device, little to no plasma is created in the power feed region, however, on a 20-MA machine, a significant amount of plasma is formed from blow off from the hot electrode surfaces. This plasma is low-density, magnetized, and has current flowing through it, making it highly susceptible to Hall physics effects. The challenge in modeling this plasma using a Hall MHD code is that it is difficult to model the outer surface of the electrodes and the production of hot plasma from that surface. Robust

conductivity models, including the implementation of lookup tables, coupled with techniques like adaptive mesh refinement, could solve these difficulties. As of the writing of this dissertation, these capabilities are not available in PERSEUS. One way to get around this is to use PERSEUS in conjunction with a kinetic model code like the CHICAGO particle-in-cell code. This would allow for accurate modeling of the formation of plasma in the power feed region [56]. Then a Hall MHD code like PERSEUS can take over to model the plasma as it flows towards the target region. Additionally, it will be important to compare PERSEUS results to codes that have more robust physics models (e.g., multi-material models, conductivity models, and radiation transport models) to determine the degree to which Hall physics is the most dominate effect.

In the effort to create an ignited fusion platform using pulsed power, there is great interest in designing and building a next generation pulsed power (NGPP) machine capable of producing current pulses > 60 MA. Scaling the current MagLIF liners from the 20 MA scale to this new regime will require very detailed simulations and theory. The theory and simulation capabilities demonstrated in this dissertation should prove key to obtaining a complete understanding of the plasma behavior and dynamics. One of the big unknowns moving into the regime of an NGPP machine is the interplay of different seeding mechanisms for the helical MRTI structures. It is unknown at this time which effect will be the dominant driver of helical seeding between flux compression, electrothermal effects, or Hall physics effects. Large scale detailed simulations with codes like PERSEUS that include Hall physics will be necessary to explore that interplay.

Another important aspect to continue from this work is the effects of convergence ratio on the stagnation column stability. This is important for inertial confinement fusion efforts in general. To achieve the highest fusion yield possible from a z-pinch implosion, it is necessary to maintain as much stability in the final stagnation column

as possible. One challenge for continuing this particular line of simulation work from a thin-foil setting to a MagLIF setting is that PERSEUS is a single material code. This makes it impossible to simulate one material for the liner and another material for the fusion fuel. One of the most important factors for determining the fusion yield of a MagLIF liner is the amount of beryllium from the liner's inner surface that mixes into the fusion fuel and limits the fusion burn. Modeling multi-material configuration for stagnation stability efforts in Hall MHD codes will be necessary to fully capture the MagLIF liner performance in simulation.

Beyond simulation work, it will be necessary to compare the results produced by PERSEUS, especially those concerned with the Hall interchange instability, with experimental results. This is difficult because of the low density of the plasma of the coronal layer. While the coronal layer has been observed in experiment [31], it is difficult to measure the Hall interchange instability directly. It may be possible to measure magnetic field perturbations, but this must be left to future work and creative experiments.

This dissertation has already resulted in one peer-reviewed journal article, titled "Extended magnetohydrodynamics simulations of thin-foil Z-pinch implosions with comparison to experiments" [23]. This paper covers helical instability formation and the effects of the on-axis support rod on the thin-foil liner implosions. A second paper, titled "Hall Instability Driven Seeding of Helical Magneto-Rayleigh-Taylor Instabilities in Axially Premagnetized Thin-Foil Liner Z-pinch Implosions", has also been prepared and is presently being submitted to the journal Physics of Plasmas. This second paper discusses the Hall interchange instability and the origins of the helical instability structures. Efforts at the national lab level have turned to Hall physics to help complete our understanding of z-pinches. By applying PERSEUS to MagLIF simulations and z-machine conditions, it will be possible to explore Hall physics effects at the 20 MA regime and lead to many more publications. This will

only be added to by moving into a NGPP 60 MA regime.

APPENDIX

APPENDIX A

Resolution Study of Hall Interchange Instability

Grid resolution is an important factor in achieving accurate simulation results. The version of PERSEUS used for this dissertation was an Eularian code with a Cartesian grid. This means that the grid was a series of cubes (as opposed to a cylindrical grid for example), and the Eularian nature of the grid means that the grid is static, unlike in a Lagrangian code. Also note that no adaptive mesh refinement techniques were implemented. This provides several difficulties when attempting to simulate an inherently cylindrical object like a z-pinch liner. If the grid resolution is too low, aliasing effects can act as seeds for plasma instabilities which can obscure the actual seeding effects that are of interest. Another consideration for the grid resolution is that enough axial resolution has to be implemented to ensure that the magneto-Rayleigh-Taylor instabilities form. To ensure this, a grid resolution of 125 μm^3 was found to be adequate. Higher grid resolutions were also explored and were not found to have significant impact of the behavior of the instabilities that were explored in this work.

To determine the effect of grid resolution on the Hall interchange instability, simulations with the same initial conditions described in Chapter III were run with several different grid resolutions. This allowed for a direct comparison across the different

resolutions. One of the key findings in this study was that there is a limit on grid-resolution that is necessary to resolve the instability structures. This applies both for the Hall interchange instability and for the helical magneto-Rayleigh-Taylor instabilities. For a comparison of the growth rate of the Hall interchange instability, the analysis in Chapter III to determine a growth rate for the Hall interchange instability was repeated for a series of grid resolutions. In each case, an axial line-out of the current instability structures was taken and the variation of the azimuthal component of the current was measured and analyzed to determine a growth rate for the instability. In each case, the growth rate was $\sim$0.1 ns^{-1} or within about 20% of this value.

To compare the growth rates across different grid resolutions, Figure 3.6 from Chapter III is repeated here in Fig. A.1 for reference. The simulation that produced this data had a resolution of 125 μm^3 and was a resolution near the lower limit to observe these instability structures. In the next plot (Figure A.2), a resolution twice that was used such that the cell size was $\sim$ 62.5 μm^3. In the higher resolution simulation, the Hall instability began forming 5-10 ns before what was observed in the lower resolution simulation (Fig. A.1). However, in both simulations, the growth rate was around 0.1 ns^{-1}. In fact, the higher resolution simulation had a growth rate that was even closer to the theoretically predicted growth rate of 0.12 ns^{-1}. In the intermediate resolution plot (Figure A.3) which follows the first two plots, the growth rate is slightly lower but the timing of the instability growth matches the lower resolution simulations very closely. These plots serve to show that resolution does not dictate the growth rate of the Hall instability structures.

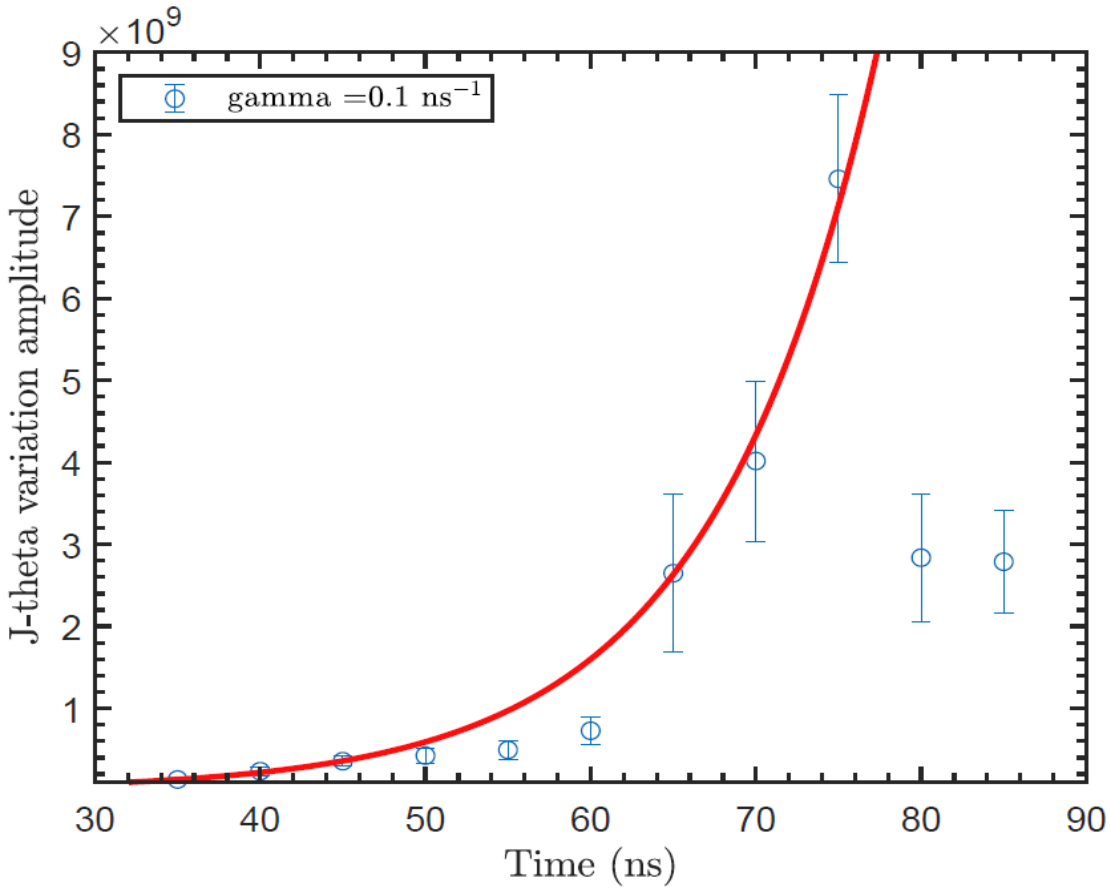

Figure A.1: Plot of the azimuthal perturbation amplitude growth rate for a simulation with grid resolution of 125 μm^3. The amplitude was taken by an axial line-out through the coronal plasma subject to the Hall interchange instability. The growth rate found from this analysis compares very closely to the growth rate predicted from theory (Eq. 1.36). The error bars are determined from one standard deviation in the perturbation amplitude.

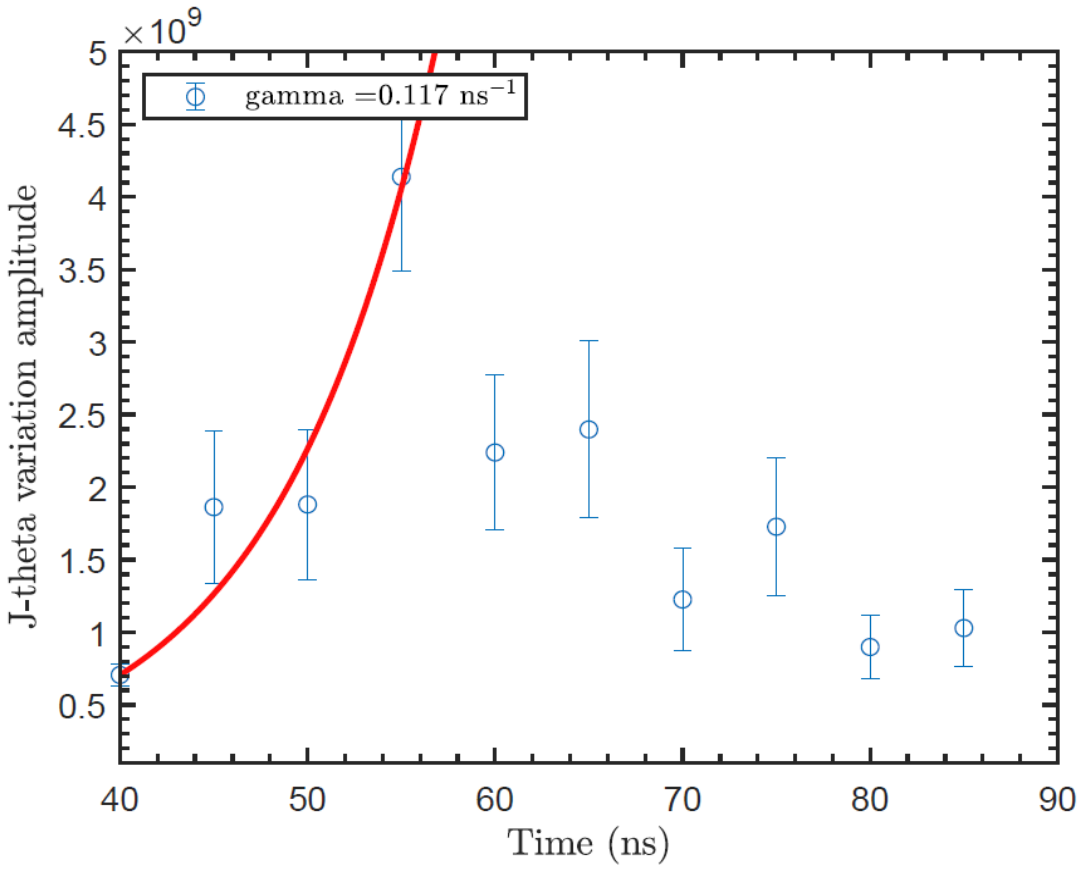

Figure A.2: Plot of the azimuthal perturbation amplitude growth rate for a simulation with grid resolution of 62.5 μm^3. The amplitude was taken by an axial line-out through the coronal plasma subject to the Hall interchange instability. The growth rate found from this analysis compares very closely to the growth rate predicted from theory (Eq. 1.36). The error bars are determined from one standard deviation in the perturbation amplitude. This plot was from a higher resolution simulation in which the instability structures began forming earlier by about 5-10 ns as compared with the lower resolution simulation presented in Fig. A.1.

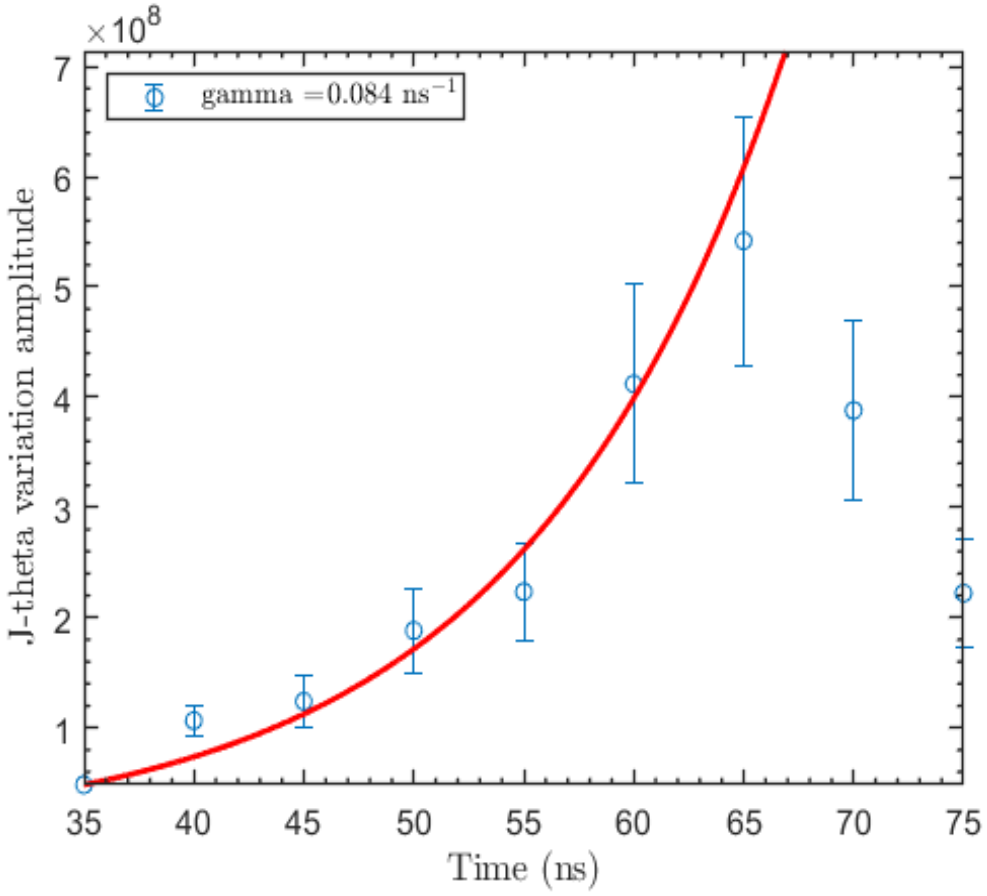

Figure A.3: Plot of the azimuthal perturbation amplitude growth rate from a simulation with grid resolution of ∼83 μm^3. The amplitude was taken by an axial line-out through the coronal plasma subject to the Hall interchange instability. The growth rate found from this analysis compares very closely to the growth rate predicted from theory (Eq. 1.36). The error bars are determined from one standard deviation in the perturbation amplitude. This plot was from an intermediate resolution simulation.

BIBLIOGRAPHY

BIBLIOGRAPHY

[1] S. A. Slutz, M. C. Herrmann, R. A. Vesey, A. B. Sefkow, D. B. Sinars, D. C. Rovang, K. J. Peterson, and M. E. Cuneo. Pulsed-power-driven cylindrical liner implosions of laser preheated fuel magnetized with an axial field. *Physics of Plasmas*, 17(5):056303, may 2010.

[2] M. R. Gomez, S. A. Slutz, A. B. Sefkow, D. B. Sinars, K. D. Hahn, S. B. Hansen, E. C. Harding, P. F. Knapp, P. F. Schmit, C. A. Jennings, T. J. Awe, M. Geissel, D. C. Rovang, G. A. Chandler, G. W. Cooper, M. E. Cuneo, A. J. Harvey-Thompson, M. C. Herrmann, M. H. Hess, O. Johns, D. C. Lamppa, M. R. Martin, R. D. McBride, K. J. Peterson, J. L. Porter, G. K. Robertson, G. A. Rochau, C. L. Ruiz, M. E. Savage, I. C. Smith, W. A. Stygar, and R. A. Vesey. Experimental Demonstration of Fusion-Relevant Conditions in Magnetized Liner Inertial Fusion. *Physical Review Letters*, 113(15):155003, oct 2014.

[3] D. B. Sinars, M. A. Sweeney, C. S. Alexander, D. J. Ampleford, T. Ao, J. P. Apruzese, C. Aragon, D. J. Armstrong, K. N. Austin, T. J. Awe, A. D. Baczewski, J. E. Bailey, K. L. Baker, C. R. Ball, H. T. Barclay, S. Beatty, K. Beckwith, K. S. Bell, J. F. Benage, N. L. Bennett, K. Blaha, D. E. Bliss, J. J. Boerner, C. J. Bourdon, B. A. Branch, J. L. Brown, E. M. Campbell, R. B. Campbell, D. G. Chacon, G. A. Chandler, K. Chandler, P. J. Christenson, M. D. Christison, E. B. Christner, R. C. Clay, K. R. Cochrane, A. P. Colombo, B. M. Cook, C. A. Coverdale, M. E. Cuneo, J. S. Custer, A. Dasgupta, J.-P. Davis, M. P. Desjarlais, D. H. Dolan, J. D. Douglass, G. S. Dunham, S. Duwal, A. D. Edens, M. J. Edwards, E. G. Evstatiev, B. G. Farfan, J. R. Fein, E. S. Field, J. A. Fisher, T. M. Flanagan, D. G. Flicker, M. D. Furnish, B. R. Galloway, P. D. Gard, T. A. Gardiner, M. Geissel, J. L. Giuliani, M. E. Glinsky, M. R. Gomez, T. Gomez, G. P. Grim, K. D. Hahn, T. A. Haill, N. D. Hamlin, J. H. Hammer, S. B. Hansen, H. L. Hanshaw, E. C. Harding, A. J. Harvey-Thompson, D. Headley, M. C. Herrmann, M. H. Hess, C. Highstrete, O. A. Hurricane, B. T. Hutsel, C. A. Jennings, O. M. Johns, D. Johnson, M. D. Johnston, B. M. Jones, M. C. Jones, P. A. Jones, P. E. Kalita, R. J. Kamm, J. W. Kellogg, M. L. Kiefer, M. W. Kimmel, P. F. Knapp, M. D. Knudson, A. Kreft, G. R. Laity, P. W. Lake, D. C. Lamppa, W. L. Langston, J. S. Lash, K. R. LeChien, J. J. Leckbee, R. J. Leeper, G. T. Leifeste, R. W. Lemke, W. Lewis, S. A. Lewis, G. P. Loisel, Q. M. Looker, A. J. Lopez, D. J. Lucero, S. A. MacLaren, R. J. Magyar, M. A. Mangan, M. R. Martin, T. R. Mattsson, M. K. Matzen, A. J. Maurer, M. G. Mazarakis, R. D.

McBride, H. S. McLean, C. A. McCoy, G. R. McKee, J. L. McKenney, A. R. Miles, J. A. Mills, M. D. Mitchell, N. W. Moore, C. E. Myers, T. Nagayama, G. Natoni, A. C. Owen, S. Patel, K. J. Peterson, T. D. Pointon, J. L. Porter, A. J. Porwitzky, S. Radovich, K. S. Raman, P. K. Rambo, W. D. Reinhart, G. K. Robertson, G. A. Rochau, S. Root, D. V. Rose, D. C. Rovang, C. L. Ruiz, D. E. Ruiz, D. Sandoval, M. E. Savage, M. E. Sceiford, M. A. Schaeuble, P. F. Schmit, M. S. Schollmeier, J. Schwarz, C. T. Seagle, A. B. Sefkow, D. B. Seidel, G. A. Shipley, J. Shores, L. Shulenburger, S. C. Simpson, S. A. Slutz, I. C. Smith, C. S. Speas, P. E. Specht, M. J. Speir, D. C. Spencer, P. T. Springer, A. M. Steiner, B. S. Stoltzfus, W. A. Stygar, J. Ward Thornhill, J. A. Torres, J. P. Townsend, C. Tyler, R. A. Vesey, P. E. Wakeland, T. J. Webb, E. A. Weinbrecht, M. R. Weis, D. R. Welch, J. L. Wise, M. Wu, D. A. Yager-Elorriaga, A. Yu, and E. P. Yu. Review of pulsed power-driven high energy density physics research on Z at Sandia. *Physics of Plasmas*, 27(7):070501, jul 2020.

[4] D. D. Ryutov, M. S. Derzon, and M. K. Matzen. The physics of fast Z pinches. *Reviews of Modern Physics*, 72(1):167–223, 2000.

[5] E. G. Harris. Rayleigh-Taylor Instabilities of a Collapsing Cylindrical Shell in a Magnetic Field. *Physics of Fluids*, 5(9):1057, 1962.

[6] D. Colombant, W. Manheimer, and E. Ott. Three-Dimensional, Nonlinear Evolution of the Rayleigh-Taylor Instability of a Thin Layer. *Physical Review Letters*, 53(5):446–449, jul 1984.

[7] R.E. Reinovsky, W.E. Anderson, W.L. Atchison, C.E. Ekdahl, R.J. Faehl, I.R. Lindemuth, D.V. Morgan, Michael Murillo, J.L. Stokes, and J.S. Shlachter. Instability growth in magnetically imploded high-conductivity cylindrical liners with material strength. *IEEE Transactions on Plasma Science*, 30(5):1764–1776, oct 2002.

[8] Aaron R. Miles. Nonlinear Rayleigh–Taylor instabilities in fast Z pinches. *Physics of Plasmas*, 16(3):032702, mar 2009.

[9] D. B. Sinars, S. A. Slutz, M. C. Herrmann, R. D. McBride, M. E. Cuneo, K. J. Peterson, R. A. Vesey, C. Nakhleh, B. E. Blue, K. Killebrew, D. Schroen, K. Tomlinson, A. D. Edens, M. R. Lopez, I. C. Smith, J. Shores, V. Bigman, G. R. Bennett, B. W. Atherton, M. Savage, W. A. Stygar, G. T. Leifeste, and J. L. Porter. Measurements of Magneto-Rayleigh-Taylor Instability Growth during the Implosion of Initially Solid Al Tubes Driven by the 20-MA, 100-ns Z Facility. *Physical Review Letters*, 105(18):185001, oct 2010.

[10] Y. Y. Lau, J. C. Zier, I. M. Rittersdorf, M. R. Weis, and R. M. Gilgenbach. Anisotropy and feedthrough in magneto-Rayleigh-Taylor instability. *Physical Review E*, 83(6):066405, jun 2011.

[11] D. B. Sinars, S. A. Slutz, M. C. Herrmann, R. D. McBride, M. E. Cuneo, C. A. Jennings, J. P. Chittenden, A. L. Velikovich, K. J. Peterson, R. A. Vesey,

C. Nakhleh, E. M. Waisman, B. E. Blue, K. Killebrew, D. Schroen, K. Tomlinson, A. D. Edens, M. R. Lopez, I. C. Smith, J. Shores, V. Bigman, G. R. Bennett, B. W. Atherton, M. Savage, W. A. Stygar, G. T. Leifeste, and J. L. Porter. Measurements of magneto-Rayleigh–Taylor instability growth during the implosion of initially solid metal liners. *Physics of Plasmas*, 18(5):056301, may 2011.

[12] M. E. Cuneo, M. C. Herrmann, D. B. Sinars, S. A. Slutz, W. A. Stygar, R. A. Vesey, A. B. Sefkow, G. A. Rochau, G. A. Chandler, J. E. Bailey, J. L. Porter, R. D. McBride, D. C. Rovang, M. G. Mazarakis, E. P. Yu, D. C. Lamppa, K. J. Peterson, C. Nakhleh, S. B. Hansen, A. J. Lopez, M. E. Savage, C. A. Jennings, M. R. Martin, R. W. Lemke, B. W. Atherton, I. C. Smith, P. K. Rambo, M. Jones, M. R. Lopez, P. J. Christenson, M. A. Sweeney, B. Jones, L. A. McPherson, E. Harding, M. R. Gomez, P. F. Knapp, T. J. Awe, R. J. Leeper, C. L. Ruiz, G. W. Cooper, K. D. Hahn, J. McKenney, A. C. Owen, G. R. McKee, G. T. Leifeste, D. J. Ampleford, E. M. Waisman, A. Harvey-Thompson, R. J. Kaye, M. H. Hess, S. E. Rosenthal, and M. K. Matzen. Magnetically Driven Implosions for Inertial Confinement Fusion at Sandia National Laboratories. *IEEE Transactions on Plasma Science*, 40(12):3222–3245, dec 2012.

[13] R. D. McBride, S. A. Slutz, C. A. Jennings, D. B. Sinars, M. E. Cuneo, M. C. Herrmann, R. W. Lemke, M. R. Martin, R. A. Vesey, K. J. Peterson, A. B. Sefkow, C. Nakhleh, B. E. Blue, K. Killebrew, D. Schroen, T. J. Rogers, A. Laspe, M. R. Lopez, I. C. Smith, B. W. Atherton, M. Savage, W. A. Stygar, and J. L. Porter. Penetrating Radiography of Imploding and Stagnating Beryllium Liners on the Z Accelerator. *Physical Review Letters*, 109(13):135004, sep 2012.

[14] T. J. Awe, R. D. McBride, C. A. Jennings, D. C. Lamppa, M. R. Martin, D. C. Rovang, S. A. Slutz, M. E. Cuneo, A. C. Owen, D. B. Sinars, K. Tomlinson, M. R. Gomez, S. B. Hansen, M. C. Herrmann, J. L. McKenney, C. Nakhleh, G. K. Robertson, G. A. Rochau, M. E. Savage, D. G. Schroen, and W. A. Stygar. Observations of Modified Three-Dimensional Instability Structure for Imploding z-Pinch Liners that are Premagnetized with an Axial Field. *Physical Review Letters*, 111(23):235005, dec 2013.

[15] R. D. McBride, M. R. Martin, R. W. Lemke, J. B. Greenly, C. A. Jennings, D. C. Rovang, D. B. Sinars, M. E. Cuneo, M. C. Herrmann, S. A. Slutz, C. W. Nakhleh, D. D. Ryutov, J.-P. Davis, D. G. Flicker, B. E. Blue, K. Tomlinson, D. Schroen, R. M. Stamm, G. E. Smith, J. K. Moore, T. J. Rogers, G. K. Robertson, R. J. Kamm, I. C. Smith, M. Savage, W. A. Stygar, G. A. Rochau, M. Jones, M. R. Lopez, J. L. Porter, and M. K. Matzen. Beryllium liner implosion experiments on the Z accelerator in preparation for magnetized liner inertial fusion. *Physics of Plasmas*, 20(5):056309, may 2013.

[16] T. J. Awe, C. A. Jennings, R. D. McBride, M. E. Cuneo, D. C. Lamppa, M. R. Martin, D. C. Rovang, D. B. Sinars, S. A. Slutz, A. C. Owen, K. Tomlinson,

M. R. Gomez, S. B. Hansen, M. C. Herrmann, M. C. Jones, J. L. McKenney, G. K. Robertson, G. A. Rochau, M. E. Savage, D. G. Schroen, and W. A. Stygar. Modified helix-like instability structure on imploding z-pinch liners that are pre-imposed with a uniform axial magnetic field. *Physics of Plasmas*, 21(5):056303, may 2014.

[17] T. J. Awe, K. J. Peterson, E. P. Yu, R. D. McBride, D. B. Sinars, M. R. Gomez, C. A. Jennings, M. R. Martin, S. E. Rosenthal, D. G. Schroen, A. B. Sefkow, S. A. Slutz, K. Tomlinson, and R. A. Vesey. Experimental Demonstration of the Stabilizing Effect of Dielectric Coatings on Magnetically Accelerated Imploding Metallic Liners. *Physical Review Letters*, 116(6):065001, feb 2016.

[18] A. G. Rousskikh, A. S. Zhigalin, V. I. Oreshkin, V. Frolova, A. L. Velikovich, G. Yu Yushkov, and R. B. Baksht. Effect of the axial magnetic field on a metallic gas-puff pinch implosion. *Physics of Plasmas*, 23(6):063502, jun 2016.

[19] D. A. Yager-Elorriaga, P. Zhang, A. M. Steiner, N. M. Jordan, P. C. Campbell, Y. Y. Lau, and R. M. Gilgenbach. Discrete helical modes in imploding and exploding cylindrical, magnetized liners. *Physics of Plasmas*, 23(12):124502, dec 2016.

[20] C. E. Seyler, M. R. Martin, and N. D. Hamlin. Helical instability in MagLIF due to axial flux compression by low-density plasma. *Physics of Plasmas*, 25(6):062711, jun 2018.

[21] D. A. Yager-Elorriaga, Y Y Lau, P Zhang, P C Campbell, A M Steiner, N M Jordan, R. D. McBride, and R M Gilgenbach. Evolution of sausage and helical modes in magnetized thin-foil cylindrical liners driven by a Z-pinch. *Physics of Plasmas*, 25(5):056307, may 2018.

[22] Paul C. Campbell, T. M. Jones, J. M. Woolstrum, N. M. Jordan, P. F. Schmit, J. B. Greenly, W. M. Potter, E. S. Lavine, B. R. Kusse, D. A. Hammer, and R. D. McBride. Stabilization of Liner Implosions via a Dynamic Screw Pinch. *Physical Review Letters*, 125(3):035001, jul 2020.

[23] J. M. Woolstrum, D. A. Yager-Elorriaga, P. C. Campbell, N. M. Jordan, C. E. Seyler, and R. D. McBride. Extended magnetohydrodynamics simulations of thin-foil Z-pinch implosions with comparison to experiments. *Physics of Plasmas*, 27(9):092705, sep 2020.

[24] K. D. Hahn, G. A. Chandler, C. L. Ruiz, G. W. Cooper, M. R. Gomez, S. Slutz, A. B. Sefkow, D. B. Sinars, S. B. Hansen, P. F. Knapp, P. F. Schmit, E. Harding, C. A. Jennings, T. J. Awe, M. Geissel, D. C. Rovang, J. A. Torres, J. A. Bur, M. E. Cuneo, V. Yu Glebov, A. J. Harvey-Thompson, M. C. Herrman, M. H. Hess, O. Johns, B. Jones, D. C. Lamppa, J. S. Lash, M. R. Martin, R. D. McBride, K. J. Peterson, J. L. Porter, J. Reneker, G. K. Robertson, G. A.

Rochau, M. E. Savage, I. C. Smith, J. D. Styron, and R. A. Vesey. Fusion-neutron measurements for magnetized liner inertial fusion experiments on the Z accelerator. *Journal of Physics: Conference Series*, 717(1):012020, may 2016.

[25] D. A. Yager-Elorriaga, P. Zhang, A. M. Steiner, N. M. Jordan, Y. Y. Lau, and R. M. Gilgenbach. Seeded and unseeded helical modes in magnetized, non-imploding cylindrical liner-plasmas. *Physics of Plasmas*, 23(10):101205, oct 2016.

[26] Adam M. Steiner, Paul C. Campbell, David A. Yager-Elorriaga, Kyle R. Cochrane, Thomas R. Mattsson, Nicholas M. Jordan, Ryan D. McBride, Y. Y. Lau, and Ronald M. Gilgenbach. The electro-thermal stability of tantalum relative to aluminum and titanium in cylindrical liner ablation experiments at 550 kA. *Physics of Plasmas*, 25(3):032701, mar 2018.

[27] D. D. Ryutov, T. J. Awe, S. B. Hansen, R. D. McBride, K. J. Peterson, D. B. Sinars, and S. A. Slutz. Effect of axial magnetic flux compression on the magnetic Rayleigh-Taylor instability (theory). In *AIP Conference Proceedings*, volume 1639, pages 63–66, 2014.

[28] Kyle J. Peterson, Daniel B. Sinars, Edmund P. Yu, Mark C. Herrmann, Michael E. Cuneo, Stephen A. Slutz, Ian C. Smith, Briggs W. Atherton, Marcus D. Knudson, and Charles Nakhleh. Electrothermal instability growth in magnetically driven pulsed power liners. *Physics of Plasmas*, 19(9):092701, sep 2012.

[29] C. E. Seyler and M. R. Martin. Relaxation model for extended magnetohydrodynamics: Comparison to magnetohydrodynamics for dense Z-pinches. *Physics of Plasmas*, 18(1):012703, jan 2011.

[30] T. J. Smith, P. C. Campbell, G. V. Dowhan, N. M. Jordan, M D Johnston, M E Cuneo, G R Laity, and R. D. McBride. Additively manufactured electrodes for plasma and power-flow studies in high-power transmission lines on the 1-MA MAIZE facility. *Review of Scientific Instruments*, 92(5):053550, may 2021.

[31] R. B. Baksht, A. S. Zhigalin, A. G. Rousskikh, and V. I. Oreshkin. Experimental studies of the shunting discharge developing during a foil explosion in vacuum. *Physics of Plasmas*, 27(4):043510, apr 2020.

[32] R. B. Baksht, S. I. Tkachenko, A. S. Zhigalin, A. G. Rousskikh, and V. I. Oreshkin. A study of the foil explosion in vacuum using spectral streak camera diagnostics. *Physics of Plasmas*, 28(6):062706, jun 2021.

[33] C. E. Seyler. Reduced magnetofluid dynamics in the lower-hybrid frequency range. *Physics of Fluids B*, 3(9):2449–2451, 1991.

[34] C. E. Seyler. Lower hybrid wave phenomena associated with density depletions. *Journal of Geophysical Research*, 99(A10):19513, 1994.

[35] C. E. Seyler and K. Wu. Instability at the electron inertial scale. *Journal of Geophysical Research: Space Physics*, 106(A10):21623–21644, oct 2001.

[36] Edward Liverts and Michael Mond. The Hall instability in accelerated plasma channels. *Physics of Plasmas*, 11(1):55–61, jan 2004.

[37] Zohar Kolberg, Edward Liverts, and Michael Mond. Waves and instabilities in weak inhomogeneous ideal Hall-magnetohydrodynamic plasmas. *Physics of Plasmas*, 12(6):062113, jun 2005.

[38] J. Loverich and U. Shumlak. Nonlinear full two-fluid study of m=0 sausage instabilities in an axisymmetric Z pinch. *Physics of Plasmas*, 13(8):082310, aug 2006.

[39] M Coppins, D. J. Bond, and M. G. Haines. A study of the stability of the Z pinch under fusion conditions using the Hall fluid model. *Physics of Fluids*, 27(12):2886, 1984.

[40] G. V. Vogman, J. H. Hammer, U. Shumlak, and W. A. Farmer. Two-fluid and kinetic transport physics of Kelvin–Helmholtz instabilities in nonuniform low-beta plasmas. *Physics of Plasmas*, 27(10):102109, oct 2020.

[41] Xiangxiong Zhang and Chi-Wang Shu. On positivity-preserving high order discontinuous Galerkin schemes for compressible Euler equations on rectangular meshes. *Journal of Computational Physics*, 229(23):8918–8934, nov 2010.

[42] A. Dedner, F. Kemm, D. Kröner, C.-D. Munz, T. Schnitzer, and M. Wesenberg. Hyperbolic Divergence Cleaning for the MHD Equations. *Journal of Computational Physics*, 175(2):645–673, jan 2002.

[43] Gábor Tóth. The ·B=0 Constraint in Shock-Capturing Magnetohydrodynamics Codes. *Journal of Computational Physics*, 161(2):605–652, jul 2000.

[44] Paul M. Bellan. Fundamentals of Plasma Physics. *Plasma Physics and Controlled Fusion*, feb 2007.

[45] H. R. Strauss. Nonlinear, three-dimensional magnetohydrodynamics of noncircular tokamaks. *Physics of Fluids*, 19(1):134, 1976.

[46] D. A. Yager-Elorriaga, A. M. Steiner, S. G. Patel, N. M. Jordan, Y. Y. Lau, and R. M. Gilgenbach. Technique for fabrication of ultrathin foils in cylindrical geometry for liner-plasma implosion experiments with sub-megaampere currents. *Review of Scientific Instruments*, 86(11):113506, nov 2015.

[47] L. Atoyan, D. A. Hammer, B. R. Kusse, T. Byvank, A. D. Cahill, J. B. Greenly, S. A. Pikuz, and T. A. Shelkovenko. Helical plasma striations in liners in the presence of an external axial magnetic field. *Physics of Plasmas*, 23(2):022708, feb 2016.

[48] P. C. Campbell, J. M. Woolstrum, F. Antoulinakis, T. M. Jones, D. A. Yager-Elorriaga, S. M. Miller, Nicholas M. Jordan, Y. Y. Lau, Ronald M. Gilgenbach, and Ryan D. Mcbride. Diagnostic and Power Feed Upgrades to the MAIZE Facility. *IEEE Transactions on Plasma Science*, 46(11):3973–3981, nov 2018.

[49] Ryan D. McBride, Charles E. Seyler, Sergei A. Pikuz, David A. Hammer, David J. Ampleford, Tania A. Shelkovenko, and Matthew R. Martin. Anode–Cathode Asymmetry in a Wire-Array *Z*-Pinch: Highly Resolved Axial-Shear-Flow Structure Observed on the Outer Edges of Ablating Wires. *IEEE Transactions on Plasma Science*, 39(11):2430–2431, nov 2011.

[50] S.V Lebedev, D.J Ampleford, S.N Bland, S.C Bott, J.P Chittenden, C. Jennings, M.G Haines, J.B.A Palmer, and J. Rapley. Implosion dynamics of wire array Z-pinches: experiments at Imperial College. *Nuclear Fusion*, 44(12):S215–S220, dec 2004.

[51] R. D. McBride, T. A. Shelkovenko, S. A. Pikuz, D. A. Hammer, J. B. Greenly, B. R. Kusse, J. D. Douglass, P. F. Knapp, K. S. Bell, I. C. Blesener, and D. A. Chalenski. Implosion dynamics and radiation characteristics of wire-array Z pinches on the Cornell Beam Research Accelerator. *Physics of Plasmas*, 16(1):012706, jan 2009.

[52] G. C. Burdiak, S. V. Lebedev, R. P. Drake, A. J. Harvey-Thompson, G. F. Swadling, F. Suzuki-Vidal, J. Skidmore, L. Suttle, E. Khoory, L. Pickworth, P. de Grouchy, G. N. Hall, S. N. Bland, M. Weinwurm, and J. P. Chittenden. The production and evolution of multiple converging radiative shock waves in gas-filled cylindrical liner z-pinch experiments. *High Energy Density Physics*, 9(1):52–62, 2013.

[53] Matthew R Weis. Magneto-Rayleigh-Taylor Instability : theory and simulation in planar and cylindrical pulsed power targets by. *University of Michigan*, PhD Thesis, 2015.

[54] C E Seyler. Axial magnetic flux amplification in Hall-magnetohydrodynamic simulations of externally magnetized z-pinches. *Physics of Plasmas*, 27(9):092102, sep 2020.

[55] P. Batten, N. Clarke, C. Lambert, and D. M. Causon. ON THE CHOICE OF WAVESPEEDS FOR THE HLLC RIEMANNSOLVER. *Siam J. Sci. Comput.*, 18(6):1553–1570, 1997.

[56] N. Bennett, D. R. Welch, C. A. Jennings, E. Yu, M. H. Hess, B. T. Hutsel, G. Laity, J. K. Moore, D. V. Rose, K. Peterson, and M. E. Cuneo. Current transport and loss mechanisms in the Z accelerator. *Physical Review Accelerators and Beams*, 22(12):120401, dec 2019.